DISSERTATION

LOW TEMPERATURE SOLUTION SYNTHESIS OF ZnSb, MnSb, AND Sr-Ru-O COMPOUNDS

Submitted by

Jennifer Lenkner Noblitt

Department of Chemistry

In partial fulfillment of the requirements

For the Degree of Doctor of Philosophy

Colorado State University

Fort Collins, Colorado

Fall 2011

Doctoral Committee:

Advisor: Amy L. Prieto

David S. Dandy
C. Michael Elliot
Ellen R. Fisher
Alan K. Van Orden

ABSTRACT

LOW TEMPERATURE SOLUTION SYNTHESIS OF ZNSB, MNSB, AND SR-RU-O COMPOUNDS

Increasing energy demands are fueling research in the area of renewable energy and energy storage. In particular, Li-ion batteries and superconducting wires are attractive choices for energy storage. Improving safety, simplifying manufacturing processes, and advancing technology to increase energy storage capacity is necessary to compete with current marketed energy storage devices. These advancements are accomplished through the study of new materials and new morphologies.

Increasing dependence on and rising demand for portable electronic devices has continued to drive research in the area of Li-ion batteries. In order to compete with existing batteries and be applicable to future energy needs such as powering hybrid vehicles, the drawbacks of Li-ion batteries must be addressed including (i) low power density, (ii) safety, and (iii) high manufacturing costs. These drawbacks can be addressed through new materials and morphologies for the anode, cathode, and electrolyte. New intermetallic anode materials such as ZnSb, MnSb, and Mn_2Sb are attractive candidates to replace graphite, the current industry standard anode material, because they are safer while maintaining comparable theoretical capacity. Electrodeposition is an inexpensive method that could be used for the synthesis of these electrode materials. Direct

electrodeposition allows for excellent electrical contact to the current collector without the use of a binder.

To successfully electrodeposit zinc and manganese antimonides, metal precursors with excellent solubility in water were needed. To promote solubility, particularly for the antimony precursor, coordinating ligands were added to the deposition bath solutions. This work shows that the choice of coordinating ligand and metal-ligand speciation can alter both the electrochemistry and the film composition. This work focuses on the search for appropriate coordinating ligands, solution pH, and bath temperatures so that high quality films of ZnSb, MnSb, and Mn_2Sb may be electrochemically deposited on a conducting substrate.

Increasing use of natural resources for energy generation has driven research in the area of energy storage using superconducting materials. To meet energy storage needs the materials must have the following features: (i) safety, (ii) superconductivity at or above liquid nitrogen temperature (77 K), (iii) low cost manufacturing processes, and (iv) robustness. The search for materials that meet all of these criteria is on-going, specifically in the area of high temperature superconductivity. The precise mechanism of superconductivity is not known. A few theories explain some of the phenomenological aspects, but not all. In order to logically select and synthesize high temperature superconductors for industrial applications, the precise mechanism must first be elucidated. Additionally, a synthetic method that yields pure, high quality crystals is required because transition temperatures have been shown to vary depending on the preparation method due to impurities. Before measuring properties of superconductors, the development of a synthesis method that yields pure, high quality crystals is required.

Most superconductors are synthesized using traditional solid state methods. This synthesis route precludes formation of kinetically stable phases. Low temperature synthesis is useful for probing thermodynamic verses kinetic stability of compounds as well as producing high quality single crystals. A novel low temperature hydrothermal synthesis of Sr-Ru-O compounds has been developed. These materials are important because of their interesting properties including superconductivity and ferromagnetism. Sr_2RuO_4 is particularly interesting as it is superconducting and isostructural to La_2CuO_4, which is only superconducting when doped. Therefore, Sr_2RuO_4 is a good choice for study of the mechanism of superconductivity. Additionally, new kinetically stable phases of the Sr-Ru-O family may be formed which may also be superconducting.

Sr-Ru-O compounds were previously synthesized via the float zone method. There is one report of using hydrothermal synthesis, but the temperatures used were 480-630 °C. In general, hydrothermal methods are advantageous because of the potential for moderate temperatures and pressures to be used. Additionally, the reaction temperature, precursor choice, and reaction time can all be used to tune the composition and morphology of the product. Hydrothermal methods are inexpensive and a one-step synthesis which is very convenient to scale up for industrial application. This work shows how a hydrothermal method at temperatures between 140 °C and 210 °C was developed for the synthesis of the Sr-Ru-O family of compounds.

ACKNOWLEDGMENTS

This work comprises only part of my research experience at Colorado State University. There is much that cannot be expressed well in words. First, I would like to thank The Boss, my advisor, Amy Prieto. Thank you so much for giving me the opportunity to work in your research group. I never thought I was smart enough to work for such a genius! Instead of thinking I was stupid, you did your best to teach me how to approach difficult problems using science. Thank you for letting me cry in your office when graduate school was too much and I wanted to quit. Thank you for encouraging me when I was questioning why I was doing this. Thank you for supporting me not only as a scientist, but also through becoming a wife and a mom. I hope the work communicated expresses the best fraction of what I learned from Amy.

Second, I would like to thank the guys working in the CIF. Sandeep Kohli taught me everything I know about operating an X-ray diffractometer and ellipsometer. Pat McCurdy taught me everything I know about SEM-EDS. Thank you so much for the hours you spent with me teaching me how to get the best data possible. The willingness to talk about all kinds of science and the always open door that encouraged questions is deeply appreciated.

Thirdly, thank you to the group. Thanks for sitting through all my group meeting talks and asking intelligent questions. Mostly, thanks for being good friends who would commiserate about the pains (and successes!) of graduate school. Particularly, thank you

to Derek Johnson, who I seriously think knows everything…and I mean everything. A special thank you goes to Mary. I don't know what I would have done without you. Someday when we are old we will get a soda and talk about grad school, hopefully with fond memories. Every time I look at a wiffle ball bat I will think of you.

Last, but certainly not least I need to thank my family. My parents always thought I could do anything and always encouraged me to do my best even when I didn't want to (especially then). To my best friend and husband, you are my rock and kept me grounded. Thank you for always believing in me and showing me what hard work means. Thank you to my sweet baby Joshua, who reminds me every day to pause in my pursuit of happiness and just be happy.

I hope you enjoy.

TABLE OF CONTENTS

1. Introduction
    1.1 World energy market 1
    1.2 Lithium-ion battery fundamental technology 3
    1.3 Fundamentals of superconductor technology 7
    1.4 References 12
2. Anode materials for lithium-ion batteries
    2.1 Introduction 14
    2.2 Alternatives to graphite as anode materials for Li-ion batteries 15
    2.3 Antimonide specific alloy materials 18
    2.4 Synthetic routes to antimonide intermetallics 25
    2.5 References 28
3. Electrodeposition of materials
    3.1 Electrodeposition introduction 29
    3.2 Metal deposition 32
    3.3 Alloy deposition 33
    3.4 Challenges of codeposition 36
    3.5 References 40
4. Solution chemistry relevant to the Zn-Sb system and single potential deposition of alloy films
    4.1 Avoiding antimony oxide formation in aqueous solutions 42
    4.2 Experimental details 45
    4.3 Variation in electrochemistry in Sb-Zn-gluconate solutions 46
    4.4 Variations in the electrochemistry of gluconic acid depending on pH.....51
    4.5 Variations in the electrochemistry of antimony-gluconate depending on pH 55
    4.6 Variations in the electrochemistry of zinc-gluconate depending on pH..... 57
    4.7 Variations in the electrochemistry of antimony-zinc-gluconate depending on pH.....62
    4.8 Deposition of ZnSb alloy films 64
        4.8.1 Experimental details 65
        4.8.2 Deposition potential, pH, and film composition 67
        4.8.3 Gluconic acid concentration, pH, and film composition 68
        4.8.4 Bath temperature and film composition.....71
    4.9 Post deposition annealing of Zn-Sb thin films.....74
    4.10 Conclusions.....75
    4.11 References 77
5. Solution chemistry relevant to the Mn-Sb system and single potential deposition of alloy films
    5.1 Manganese chemistry in aqueous solution 79

5.2 Avoiding antimony oxide formation in aqueous solution 80
5.3 Experimental details 83
5.4 pH dependence of electrochemistry 84
5.4.1 Variation in electrochemistry in Sb-Mn-citrate solutions..... 84
5.4.2 Variation in electrochemistry in Sb-Mn-EDTA solutions.....90
5.4.3 Variation in electrochemistry in Sb-Mn-gluconate solutions 97
5.5 Constant potential depositions and film composition 101
5.5.1 Experimental details 102
5.5.2 Deposition bath temperature, pH, and film composition 103
5.5.3 High temperature depositions, pH, and film composition 108
5.6 Electrodeposition of Mn-Sb wires in an anodic alumina template 117
5.6.1 Experimental details 117
5.6.2 Deposition of Mn-Sb alloy wires in a template 118
5.7 Post deposition annealing of Mn-Sb thin films 122
5.8 Conclusions 124
5.9 References 126
6. Conclusions and future work for the ZnSb and MnSb systems
6.1 The ZnSb system 127
6.1.1 Single potential deposition of ZnSb thin films 127
6.1.2 Optimizing the film composition.....128
6.2 The MnSb system 128
6.1.1 Single potential deposition of MnSb thin films.....129
6.1.2 Optimizing the film composition.....129
6.3 Future work: ZnSb and MnSb systems.....130
7. Synthesis of Sr-Ru-O compounds, of which Sr_2RuO_4 is superconducting
7.1 Introduction 132
7.2 La_2CuO_4 and the evolution of copper based superconductors 132
7.3 Non-copper oxide based superconductors 134
7.4 Theories of superconductivity..... 136
7.5 Current synthetic methods 138
7.6 References.....142
8. Facile synthesis of members of the Sr-Ru-O family
8.1 Overview 144
8.2 Introduction 144
8.3 Experimental details 147
8.3.1 Preparation of Sr-Ru-O compounds 147
8.3.2 Characterization 148
8.4 Results and discussion 148
8.4.1 Synthesis of Sr-Ru-O compounds 148
8.4.2 Effect of reaction time 155
8.4.3 Effect of pH 158
8.4.4 Effect of temperature 159
8.4.5 Controlling the CO_2 concentration..... 160
8.5 Conclusions.....160
8.6 References 164

LIST OF FIGURES

Figure 1.1 Distribution of the total world energy consumption in 2007 1
Figure 1.2 Energy densities of common batteries 3
Figure 1.3 Schematic of a conventional Li-ion battery 4
Figure 1.4 Schematic of the Meissner effect 7
Figure 3.1 Length scales of electrochemical deposition 31
Figure 4.1 Cyclic voltammograms of Sb-Zn-gluconate, Sb- gluconate, and Zn-gluconate at different pH values 47
Figure 4.2 Current-time transient of Zn deposition from gluconic acid bath 50
Figure 4.3 Cyclic voltammograms of gluconic acid at different pH values 51
Figure 4.4 Speciation diagram of gluconic acid 54
Figure 4.5 Cyclic voltammograms of Sb-gluconate at different pH values 56
Figure 4.6 Speciation diagram of zinc in the zinc-gluconate system 59
Figure 4.7 Cyclic voltammograms of zinc-gluconate at different pH values 60
Figure 4.8 Cyclic voltammograms of antimony-zinc-gluconate at different pH values ...63
Figure 4.9 Cyclic voltammograms of antimony, zinc gluconate with varying concentrations of gluconate at different pH values 70
Figure 4.10 XRD pattern of Zn-Sb alloy films deposited at room temperature 72
Figure 4.11 XRD pattern of Zn-Sb alloy films deposited at 60 °C 73
Figure 5.1 Chemical structures of gluconic acid, EDTA, and citric acid 81
Figure 5.2 Cyclic voltammograms of Sb-citrate, Mn-citrate, and citrate solutions at different pH values 85
Figure 5.3 Speciation diagram of citric acid 89
Figure 5.4 Cyclic voltammograms of Sb-EDTA, Mn-EDTA, and EDTA solutions at different pH values 92
Figure 5.5 Speciation diagram of EDTA 95
Figure 5.6 Cyclic voltammograms of Sb-gluconate, Mn-gluconate, gluconate solutions 98
Figure 5.7 XRD pattern of Sb-Mn films deposited from citric acid solutions 104
Figure 5.8 XRD pattern of Sb-Mn films deposited from EDTA solutions 105
Figure 5.9 XRD pattern of Sb-Mn films deposited from gluconate solutions 107
Figure 5.10 XRD pattern of Sb-Mn films deposited from citrate solutions at 60 °C 109
Figure 5.11 XRD pattern of Sb-Mn films deposited from EDTA solutions at 60 °C 110
Figure 5.12 XRD pattern of Sb-Mn films deposited from gluconate solutions at 60 °C 112
Figure 5.13 EDS elemental mapping of Mn-Sb thin films 113
Figure 5.14 SEM images of Mn-Sb wires 119
Figure 5.15 EDS elemental mapping of Mn-Sb wires 121
Figure 5.16 XRD pattern of Sb-Mn annealed films.....123
Figure 7.1 Illustration of solid state diffusion.....140

Figure 8.1 XRD pattern of $SrRuO_4 \cdot H_2O$ 149
Figure 8.2 XRD pattern of $Sr_2Ru_3O_{10}$ and $SrRuO_4 \cdot H_2O$ 151
Figure 8.3 TEM-SAED images of $Sr_4Ru_2O_9$ 152
Figure 8.4 XRD pattern of $SrRuO_4 \cdot H_2O$, $Sr_2Ru_3O_{10}$, $Sr_4Ru_2O_9$, and $SrCO_3$ 153
Figure 8.5 XRD pattern of $SrRuO_3$ 155
Figure 8.6 SEM images of $SrRuO_4 \cdot H_2O$ formed at different reaction times.....156
Figure 8.5 XRD pattern of phase boundary material 157

LIST OF TABLES

Table 1.1 Critical transition temperatures for practical superconductors 8
Table 2.1 Cycling rate and energy densities for ZnSb electrodes 24
Table 3.1 Lattice parameters for ZnSb, MnSb, Mn2Sb, Cu, Zn, Mn, and Sb 37
Table 4.1 Energy dispersive X-ray spectroscopy data for Zn-Sb alloy films.....67
Table 4.2 Energy dispersive X-ray spectroscopy data for Zn-Sb alloy films deposited from different concentrations of gluconic acid.....69
Table 5.1 Characteristic redox potentials of Mn-gluconate complexes.....115
Table 7.1 Copper oxide based superconductors and their critical temperature 133
Table 8.1 Strontium ruthenate reaction summary.....147
Table 8.2 Summary of Sr-Ru-O reaction products and the Ru oxidation state 161

CHAPTER 1

FUNDAMENTAL ENERGY STORAGE TECHNOLOGY

1.1 World energy market

World energy consumption is projected to grow by 49% from 2007 to 2035, while the population of the world is expected to grow less than one percent [1, 2]. The large increase can be attributed to a substantial increase in the average amount of energy consumption per capita and an increase in the number of people living a high-energy lifestyle. Rising standards of living increase the demand for personal recreational vehicles, cellular phones, laptop computers, and home appliances. Additionally, the expansion of commercial services including hospitals, office buildings, and large shopping centers contribute to the growth of electricity generation, particularly in countries where infrastructures are quickly growing. Figure 1.1 shows the allocation of the total world delivered energy consumption in 2007 [1].

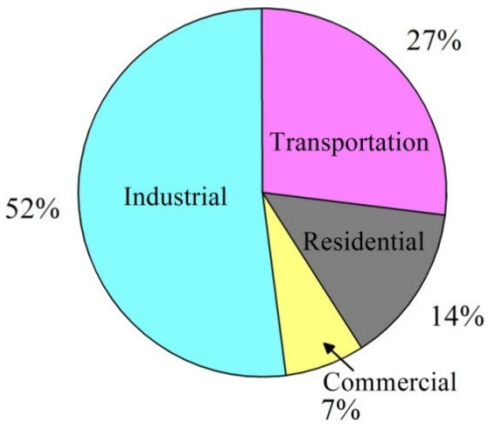

Figure 1.1. Distribution of the total world delivered energy consumption in 2007.

Industrial activity including manufacturing, agriculture, mining, and construction accounts for 52% of the world's energy consumption. Energy use in transportation of goods and people is responsible for 27% of the world's total delivered energy, mostly in the form of liquid fuels [1]. Lastly, residential and commercial sources use a combined 21% of the world's energy output. Renewable energy sources delivered 18% of the energy consumed in 2007. To obtain and sustain the projected worldwide demand for energy consumption of the future, renewable sources must provide a larger percentage of the energy demanded [1, 2]. One area where renewable sources are of particular importance is electricity generation. The fastest growing form of energy consumption in the world is electricity. Electricity generation is primarily coal, followed by renewable sources, natural gas, nuclear sources, and finally liquids. In order to move toward the use of renewable resources for electricity generation once energy has been harvested from renewable sources, *a viable storage scheme for the harvested energy is a necessity.*

Research into energy storage systems is focused on the production of inexpensive and safe storage devices with high storage capacity. Two such storage schemes include batteries and superconducting magnetic energy storage systems. Current battery research is focused on new morphologies and materials for the cathode, the anode, and the electrolyte [3-11]. On the other hand, research on superconducting magnetic storage systems focuses on the development of high-temperature superconductor materials to avoid cryogenic cooling [12-14]. Understanding how batteries and superconducting magnets work is crucial to rationally choosing new materials to improve energy storage capacities.

1.2 Lithium-ion battery fundamental technology

The ideal battery would have the following characteristics: long cycle lifetime, small size, light weight, high energy density, safety, low environmental impact, and low cost [15]. Lithium-ion batteries make up 63% of portable battery sales worldwide, in part because of their popular use in personal portable electronic devices [3]. Besides batteries based on metallic lithium, Li-ion batteries have the highest volumetric and gravimetric energy density as shown in Figure 1.2.

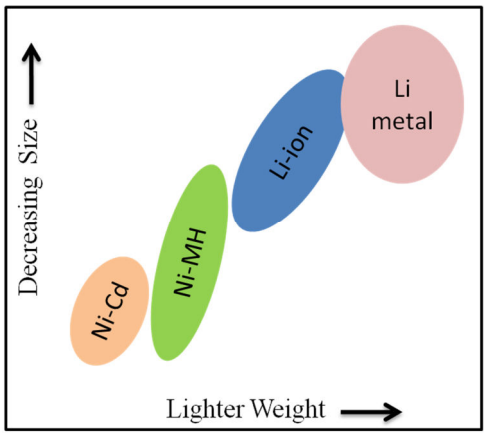

Figure 1.2. Volumetric and gravimetric energy density of common batteries. Adapted from Tarascon et al.[3].

None of the current rechargeable batteries meet all the criteria for an ideal battery mainly because a balance between size, weight, and energy density has not been achieved. Improvements in new electrode materials focus on energy density, capacity, reactivity, reversibility, and structural stability. This work focuses on the development of anode materials for Li-ion batteries because of their excellent energy density.

A battery is composed of electrochemical cells which have one positive and one negative electrode separated by an electrolyte solution that allows ion transfer between

the electrodes. In order to achieve the desired voltage and capacity, these electrochemical cells are connected in series or parallel. Currently, the most commonly used cathode and anode materials are $LiCoO_2$ and LiC_6, respectively. A schematic of a typical Li-ion cell is shown in Figure 1.3 using $LiCoO_2$ and LiC_6 in this example.

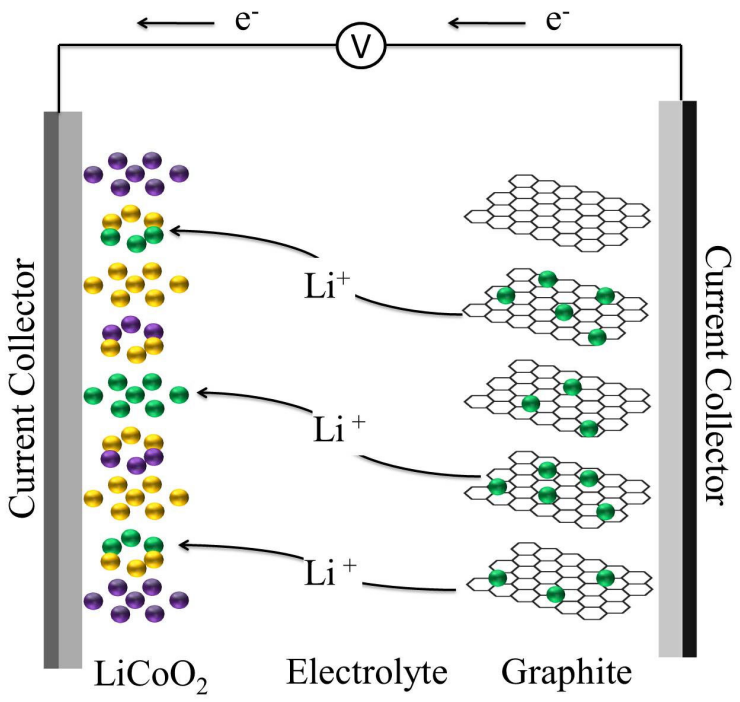

Figure 1.3. Schematic showing the discharge of a Li-ion cell. The $LiCoO_2$ cathode is on the left and the graphite anode is on the right. An electrolyte occupies the space between the electrodes, which allows the diffusion of Li-ions but prevents the passing of electrons.

When the battery is charged, the graphite anode is lithiated and the $LiCoO_2$ cathode is delithiated. When the electrodes are connected externally via the current collectors, electrons pass through the load while the Li-ions pass through the electrolyte from the anode to the cathode. Equations 1.1-1.3 relate the relevant electrochemistry occurring at each electrode.

Anode: $Li_xC \rightarrow C + xLi^+ + xe^-$ [1.1]

Cathode: $Li_{1-x}CoO_2 + xLi+ + xe^- \rightarrow LiCoO_2$ [1.2]

Overall: $Li_xC + Li_{1-x}CoO_2 \rightarrow C + LiCoO_2$ [1.3]

These reactions occur simultaneously at both electrodes which frees electrons for use. To charge the cell, the polarity is reversed, and electrons flow into the anode and the Li-ions move toward cathode. The amount of electrical energy available for delivery is expressed by weight or volume with the units Wh/kg and Wh/L, respectively. Accessible energy is dependent on the cell potential measured in V and capacity with the units Ah/kg. The capacity (Q) and voltage (E) of a cell are theoretically determined using Faraday's equation (Eq. 1.4) and Gibbs free energy (Eq. 1.5)

$$Q = \frac{nF}{M} \quad [1.4]$$

$$\Delta G = nFE \quad [1.5]$$

Here, n is the number of electrons involved, F is Faraday's constant, and M is the equivalent molecular weight. [16]

Current research is focused on improving electrode materials and focuses on five main areas including:

1. *Higher energy density*
2. *Larger storage capacity*
3. *Higher reactivity, reversibility, and structural stability during cycling process*
4. *Faster ionic diffusion and electron diffusion at high charge/discharge rates*
5. *Lower cost.*

Except for the cost, these properties are related to the intrinsic properties of the electrode material. Cycling lifetimes are dependent on the nature of the electrode/electrolyte interface. Safety is dependent on the stability of the electrode materials as well as the interface. Two main approaches are being explored by researchers to improve the electrode materials and achieve the previously stated goals. First is choosing materials that can store large amounts of lithium while having fast kinetics for lithium inclusion. Secondly, exploring nanoscale material morphologies yields materials with decreased lithium-ion diffusion lengths. Nanoscale materials exhibit improved electrode performance solely based on decreasing size [15-27]. The smaller the distance lithium is required to move within an electrode greatly improves both ionic and electronic transport [15].

As for improving the electrolyte, researchers are considering new materials that increase lithium-ion conductivity, while at the same time improving interface stability. Lithiated graphite interacts with polar solvents and lithium salts are produced at the anode/electrolyte interface. These salts along with degradation products from the reduction of the organic electrolyte precipitate on the anode and passivate the surface forming a solid electrolyte interface (SEI) layer so that it is Li-ion conducting but electronically insulating [28-30]. Researchers are also investigating electrolyte additives to facilitate the formation of the SEI layer and improve long-term cycling [29, 31].

Improvement of anode materials is of particular interest. Currently, graphite is the anode of choice for Li-ion batteries. Lithium batteries with graphite anodes operate near the potential where metallic lithium plates out and the growth of lithium dendrites upon cycling reduces battery lifetime and introduces a fire hazard. New anode materials to

replace graphite are being scrutinized including ZnSb, MnSb, and Mn_2Sb. The goal for the research herein is to directly electrodeposit ZnSb, MnSb, and Mn_2Sb anode materials on a conducting substrate. This was achieved by electrodepositing Zn-Sb films from aqueous solution at a single potential at room temperature. The properties of ZnSb that make it an attractive alternative to graphite as an anode material in Li-ion batteries will be discussed later. In Chapter 2, the use of graphite and other alternative anode materials for Li-ion batteries will be discussed in detail.

1.3 Fundamental superconductor technology

Superconductivity is a phenomenon that occurs in certain materials below a characteristic temperature where zero electrical resistance is observed when a low current is applied with no magnetic field present, or if the field does not exceed a certain value. Superconductivity is characterized by the Meissner effect, where the magnetic field is ejected from the interior of the superconducting material as it transitions to the superconducting state. Figure 1.4 is a schematic description of the Meissner effect.

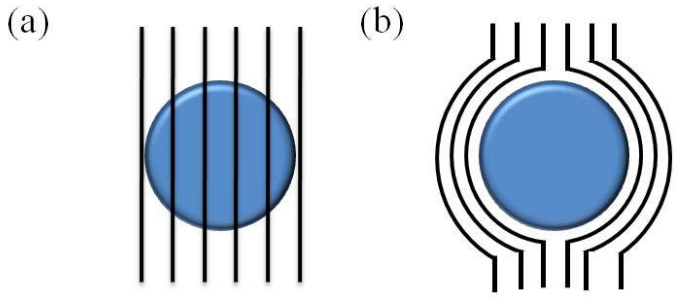

Figure 1.4 Schematic showing the Meissner effect. Magnetic field lines (black) are excluded from a superconductor when it is below the critical temperature.

Figure 1.4a shows how a superconducting material is penetrated by magnetic field lines above the critical temperature, T_c. Below T_c, the superconductor expulses the magnetic field (Figure 1.4b). The Meissner effect is famously demonstrated by a superconductor cooled below the characteristic T_c levitating a magnet. These materials are classified as Type I or Type II if the superconductivity is suddenly destroyed upon reaching a critical field value or has a continuous transition from superconducting to normal state, respectively.

In a normal conductor, the flow of electrons can be visualized as electrons moving across an ionic lattice where the electrons collide with the ions in the lattice. During each collision, energy is transferred from the electron to the lattice and converted to heat. Electrical resistance is the result of this energy dissipation. On the other hand, below T_c of a superconductor, the resistance is zero. This characteristic temperature is material dependent and can vary from < 1 K to 130 K. Table 1.1 is a summary of synthesized superconductors and their critical temperature.

Table 1.1. Summary of critical transition temperatures for practical superconductors.

Material	T_c (K)
Sr_2RuO_4	1
$La_{2-x}Ba_xCuO_4$	30
MgB_2	39
$YBa_2Cu_3O_x$	92
$Bi_2Sr_2Ca_2Cu_3O_x$	108
$Hg_2Ba_2Ca_2Cu_3O_x$	130

High temperature superconductors transition to the superconducting state at or above liquid nitrogen temperatures (77 K). Below this temperature, liquid helium is required.

Cooling superconducting materials using liquid helium is not a viable option if these materials are to be used for energy storage. Instead, liquid nitrogen is a less expensive option for refrigeration and several materials with T_c at above liquid nitrogen temperature have been discovered (Table 1.1). As an added benefit, liquid nitrogen can be produced on site-from air.

How superconductors work is a hotly debated topic in the solid-state physics community [13, 14, 32-37]. The main competing theories on the mechanism of superconductivity are dependent on pairing or independent of pairing. Perhaps the most famous is the Bardeen, Schrieffer, Cooper (BSC) theory which states that electron-lattice interactions mediated by an exchange of phonons between electron pairs leads to an electron-electron interaction resulting in electron pairing in the superconducting state [38]. Another explanation of superconductivity is the resonating-valence-bond theory which is based upon the idea that electron pairs between adjacent atoms can coordinate or partially coordinate resonance throughout the crystal [39]. Although both of these theories explain phenomenological aspects of some superconductors, they fail to explain microscopic events that lead to superconductivity. In addition, neither theory allows for the prediction of new superconductors [40].

Superconductors are mainly characterized by the critical current density (J_c) as well as the field and operating temperature. Target current densities are 10^4-10^5 A/cm^2 in fields of 0.1-10 T at temperatures 20-77 K. Current applications for superconductors that utilize these properties are: electromagnets used for nuclear magnetic resonance (NMR), magnetic resonance imaging (MRI), mass spectrometers, particle accelerators, magnetic separation, and Josephson junctions which are used for superconducting quantum

interference devices (SQUIDs) [41]. The potential uses for superconducting materials range from electric power transmission to high-performance electric motors for vehicle propulsion [38, 41].

In order for superconductors to be used for power technology, research is focused on material requirements that must be met including:

1. *operation at liquid nitrogen temperatures (65-80 K)*
2. *the material must withstand the fabrication processes (winding, cooling, electromagnetic stress)*
3. *the ability to be made a sufficient size or cabled*
4. *carry hundreds to thousands of Amps*
5. *cost comparable to copper.*

So far, these restrictions have limited the present choice to $YBa_2Cu_3O_x$ (YBCO) and $Bi_2Sr_2Ca_2Cu_3O_x$ (Bi-2223) [41]. New materials are needed to make superconductors realistic and useful for power applications. Understanding the first principles of superconductivity is necessary to logically build a practical superconducting material from the ground up. Knowing the mechanism of superconductivity would make it possible to accurately predict which materials are superconducting and allow for material design to tune the critical temperature and achieve the material requirements stated above.

The goal of this work is to develop a low-temperature synthesis method to form members of the Sr-Ru-O family, of which Sr_2RuO_4 is superconducting. This family of materials is important because of their interesting properties including superconductivity and colossal magnetoresistance, among others [35, 42, 43]. The T_c for Sr_2RuO_4 is ~1 K,

Table 1.1, which is not useful for practical applications. However, this material is superconducting without doping, unlike isostructural La_2CuO_4, hence it is a prime candidate for first-principles studies to investigate the mechanism of superconductivity [35]. Previously, strontium ruthenates have been synthesized using floating zone methods, although there is one report of the synthesis of $Sr_2Ru_3O_{10}$ using high pressure and temperature hydrothermal methods (480-630 °C) [44]. Hydrothermal methods are advantageous because of the combinations of moderate temperatures and pressures that can be achieved. Additionally, low-temperature synthesis methods are useful for probing thermodynamic versus kinetic stability of compounds as well as for producing high-quality crystals. Hydrothermal methods have been utilized at lower temperatures (140 to 210°C) and pressures to synthesize this family of compounds.

1.4 References

[1] I.E. Agency, in: W.E.O. 2010, (Ed.), Paris, France, 2010.
[2] BP Statistical Review of World Energy June 2011, bp.com/statistical review (accessed May-June 2011).
[3] J.M. Tarascon, M. Armand, *Nature* 414 (2001) 359-367.
[4] J.-M. Tarascon, *Philos. T. Roy. Soc. A* 368 (2010) 3227-3241.
[5] J.M. Tarascon, N. Recham, M. Armand, J.N. Chotard, P. Barpanda, W. Walker, L. Dupont, *Chem. Mater.* 22 (2010) 724-739.
[6] M.M. Thackeray, J.T. Vaughey, L.M.L. Fransson, *JOM-J. Min. Met. Mat. S.* 54 (2002) 20-23.
[7] M.M. Thackeray, J.T. Vaughey, C.S. Johnson, A.J. Kropf, R. Benedek, L.M.L. Fransson, K. Edstrom, *J. Power Sources* 113 (2003) 124-130.
[8] J.T. Vaughey, C.S. Johnson, A.J. Kropf, R. Benedek, M.M. Thackeray, H. Tostmann, T. Sarakonsri, S. Hackney, L. Fransson, K. Edström, J.O. Thomas, *J. Power Sources* 97-98 (2001) 194-197.
[9] J.-S.H.L.-J.W. Yu-Guo Guo, *Adv. Mater.* 20 (2008) 2878-2887.
[10] K. Zaghib, M. Armand, M. Gauthier, *J. Electrochem. Soc.* 145 (1998) 3135-3140.
[11] S.S. Zhang, *J. Power Sources* 162 (2006) 1379-1394.
[12] T.H. Geballe, *J. Supercond. Nov. Magn.* 19 (2006) 261-276.
[13] M.R. Norman, *Science* 332 (2011) 196-200.
[14] J. Orenstein, A.J. Millis, *Science* 288 (2000) 468-474.
[15] F.Y. Cheng, J. Liang, Z.L. Tao, J. Chen, *Adv. Mater.* 23 (2011) 1695-1715.
[16] J. Chen, F. Cheng, *Accounts Chem. Res.* 42 (2009) 713-723.
[17] S.P.P.S.P.L.T.B.S. J. Hassoun, *Adv. Mater.* 19 (2007) 1632-1635.
[18] S.K. Cheah, E. Perre, M.r. Rooth, M. Fondell, A. HÃ¥rsta, L. Nyholm, M. Boman, T.r. Gustafsson, J. Lu, P. Simon, K. EdstroÌˆm, *Nano. Lett.* 9 (2009) 3230-3233.
[19] C.K. Chan, H. Peng, R.D. Twesten, K. Jarausch, X.F. Zhang, Y. Cui, *Nano Lett.* (2007) 490-495.
[20] U. Kasavajjula, C. Wang, A.J. Appleby, *J. Power Sources* 163 (2007) 1003-1039.
[21] N.C. Li, C.R. Martin, B. Scrosati, *J. Power Sources* 97-8 (2001) 240-243.
[22] N.C. Li, D.T. Mitchell, K.P. Lee, C.R. Martin, *J. Electrochem. Soc.* 150 (2003) A979-A984.
[23] J. Liu, Y. Li, R. Ding, J. Jiang, Y. Hu, X. Ji, Q. Chi, Z. Zhu, X. Huang, *J. Phys. Chem. C.* 113 (2009) 5336-5339.
[24] J. Ning, T. Jiang, K. Men, Q. Dai, D. Li, Y. Wei, B. Liu, G. Chen, B. Zou, G. Zou, *J. Phys. Chem. C.* 113 (2009) 14140-14144.
[25] A.K. Nitin, M. Joachim, *Adv. Mater.* 21 (2009) 2664-2680.
[26] S. Panero, B. Scrosati, M. Wachtler, F. Croce, *J. Power Sources* 129 (2004) 90-95.
[27] C.R. Sides, N.C. Li, C.J. Patrissi, B. Scrosati, C.R. Martin, *MRS Bull.* 27 (2002) 604-607.
[28] K. Xu, *Chem. Rev.* 104 (2004) 4303-4418.

[29] D. Aurbach, *J. Power Sources* 89 (2000) 206-218.
[30] V. Thangadurai, W. Weppner, *Ionics* 12 (2006) 81-92.
[31] K. Abe, Y. Ushigoe, H. Yoshitake, M. Yoshio, *J. Power Sources* 153 (2006) 328-335.
[32] J. Friedel, *J. Phys.-Condens. Mat.* 1 (1989) 7757-7794.
[33] T.H. Geballe, *J. Supercond. Nov. Magn.* 19 (2006) 261-276.
[34] D.A. Huse, M.P.A. Fisher, D.S. Fisher, *Nature* 358 (1992) 553-559.
[35] Y. Maeno, H. Hashimoto, K. Yoshida, S. Nishizaki, T. Fujita, J.G. Bednorz, F. Lichtenberg, *Nature* 372 (1994) 532-534.
[36] P. Monthoux, D. Pines, G.G. Lonzarich, *Nature* 450 (2007) 1177-1183.
[37] M. Sigrist, K. Ueda, *Rev. Mod. Phys.* 63 (1991) 239-311.
[38] A.K. Saxena, High-Temperature Superconductors, Springer Berlin Heidelberg, 2010, pp. 199-214.
[39] L. Pauling, *P. Natl. Acad. Sci. USA* 60 (1968) 59-65.
[40] J.E. Hirsch, *Phys. Scripta* 80 (2009).
[41] D. Larbalestier, A. Gurevich, D.M. Feldmann, A. Polyanskii, *Nature* 414 (2001) 368-377.
[42] G. Cao, C.S. Alexander, S. McCall, J.E. Crow, R.P. Guertin, *Materi. Sci. Eng. B-Adv.* 63 (1999) 76-82.
[43] I. Eremin, D. Manske, S.G. Ovchinnikov, J.F. Annett, *Ann. Phys.* 13 (2004) 149-174.
[44] C. Renard, S. Daviero-Minaud, F. Abraham, *J. Solid State Chem.* 143 (1999) 266-272.

CHAPTER 2

ANODE MATERIALS FOR LITHIUM-ION BATTERIES

2.1. Introduction

Graphite electrodes are widely used as anode materials for Li-ion batteries. The basic function of the electrode is to reversibly intercalate-deintercalate lithium without significant structural damage [1]. The fully lithiated form of graphite is LiC_6 and the material provides a specific capacity of 372 mAh/g [2]. When used in a battery, the material is suspended in a conducting slurry containing 80% graphite and 20% poly-vinylidene fluoride. The slurry has two functions (i) providing electrical contact between the current collector and graphite and (ii) providing mechanical stability for the graphite. Even though graphite has been adopted as the industry standard anode material in Li-ion batteries, there are still many shortcomings to be improved.

Major challenges with the use of these electrodes include (i) lithiated graphite operates near the potential of metallic lithium, (ii) undesirable interactions occur between the active material and solution species, (iii) the necessity of the inactive material in the slurry adds weight to the battery while not contributing to the capacity, and (iv) delamination or loss of active material due to volume expansion upon lithium insertion [1, 3]. Research currently focuses on approaches to improve safety, reduce the effects of volume expansion, and minimize side reactions with the electrolyte. Working toward these objectives has resulted in the development of three classes of materials including: (i) thin film and amorphous alloys, (ii) multiphase composites and (iii) intermetallics.

Advantages and disadvantages of each class of material will be discussed in the next section.

2.2 Alternatives to graphite as anode materials for Li-ion batteries

Thin film anodes are an attractive candidate to replace graphite anode materials because they have exhibited good capacity retention and excellent cycling performance [4-8]. Thin films have the added benefit of making good electrical contact with the electrode support and good capacity retention is attributed to this. However, the performance of these anodes is strongly dependent on deposition rate, temperature, substrate roughness, film thickness, and post-processing treatments [9]. Moreover, the thin films expand with the insertion of lithium causing pulverization of the electrode and eventually loss of active material and loss of electrical contact. An amorphous Si thin film deposited on Ni foil exhibited a specific capacity of over 2000 mAh/g and good cycle stability of over 1000 cycles [10, 11]. However, the cycle lifetime was reduced when the film thickness was increased due to increased diffusion lengths and higher electrical resistance. Although these materials may seem ideal, the high processing cost prohibits the widespread commercial use. The high costs associated with depositing high-quality thin films, the effects of volume changes, and film expansion due to cycling can be alleviated by the use of a multiphase composite.

An electrode material dispersed in an inactive composite matrix results in the formation of a multiphase composite. The purpose of dispersing active electrode material in an inactive filler matrix is to use the host matrix to buffer the volume change of the active material upon lithium insertion so electronic contact between particles and

between particles and the current collector can be maintained [9]. The host matrix must allow passage of electrons and Li ions and maintain structural stability of the entire anode. The type of host phase determines the type of composite anode which can be described as: (a) an inactive matrix, (b) an active matrix, (c) a carbon-matrix composite, and (d) a porous structure. Each type of multiphase composite anode is briefly described below.

A multiphase composite formed using an inactive-matrix consists of active particles in an electrochemically inert matrix. The matrix can be a metal like Fe or Cu, an alloy like $FeSi_2$, or a ceramic like TiN [9]. Good cycling stability for over 100 cycles with a reversible capacity of 600 mAh/g has been reported. Drawbacks to these anodes include slow lithium and electron diffusion resulting in a lowered capacity.

Active-matrix anodes include the active material and host matrix, both of which are reactive towards lithiation at different onset potentials. For example, in a SnSb alloy lithiation of Sb begins at 0.9 V vs. Li/Li^+ while lithiation of Sn begins at 0.6 V. These materials suffer from poor cycle lifetimes.

Carbon-matrix anodes are prepared by ball milling active materials with graphite. Carbon additives have the advantages of good ionic conductivity, low volume expansion, ability to handle mechanical stress, and are lithiated. Silicon has been investigated as an active material in a carbon-matrix anode composite due to its high theoretical capacity of 4200 mAh/g. Including Si in a carbon matrix minimizes the effects of volume expansion by buffering the mechanical stress induced by lithium insertion [12]. A balance between capacity retention and specific capacity must be met with carbon-matrix composites to maximize the Li storage performance. That goal is achieved by combining the

advantageous properties of carbon (long cycle lifetime) with a material with a high storage capacity [12-14].

Porous structures can help overcome the volume expansion problem. These structures are formed by electrodepositing the active material on a porous current collector. While these materials exhibited improved cycle performance (400 cycles at 500 mAh/g for Si deposited on Ni foam) the large volume of pores decreases the volumetric energy density of the cell [9]. Though porous multiphase composite anodes look promising, the addition of the porous material adds cost and lowers the gravimetric and volumetric density of the battery. The volumetric density is of particular concern since many consumer applications have strict size requirements.

Instead of using a matrix to absorb the volume changes associated with lithium intercalation, intermetallic materials, where the lithiated compound maintains a strong structural relationship to the parent compound, have been utilized [2, 15-18]. In an intermetallic compound, a stable sublattice is present which is similar to graphite layers in carbon, but instead of lithium intercalation between layers, lithium is inserted into the host lattice as another lattice component is extruded. For example, in a MnSb anode Li inserts into the MnSb structure to form LiMnSb, then with Mn extrusion Li_3Sb is formed without disruption to the fcc (face-centered cubic) Sb sublattice [15].

Besides minimizing volume expansion due to resemblance of parent and lithiated compounds, intermetallic electrodes are attractive alternatives to graphite because they do not operate near the potential of lithium metal and preclude dendritic growth of lithium. Additionally, the theoretical specific capacities of alloy anode materials are 2-10 times greater than that of graphite [9]. For example, a SnSb nanocomposite demonstrated a

long cycle life of 300 cycles at a capacity of 560 mAh/g [19]. Lastly, after the first irreversible capacity loss, a good cycle lifetime is achieved. Despite the attractiveness of intermetallic electrodes as an alternative to graphite, there are many challenges. One of the major limitations of intermetallic electrodes is the tendency to suffer from irreversible capacity loss on the first cycle. Capacity losses are attributed to (i) loss of active material due to electrode pulverization, (ii) formation of a solid-electrolyte interface (SEI) that passivates the electrode surface, (iii) Li trapping in the host lattice, (iv) reaction with surface oxide layers, and (v) aggregation of alloy particles which increases lithium diffusion length. These issues compromise the cycling efficiency and cycle lifetime of lithium cells such that they are generally not useful for commercial applications [2]. Despite these challenges, materials with large volume changes have been successful commercially, like the Ni/Cd battery or the traditional lead acid battery. The Ni/Cd battery has a volume expansion of 130% and the lead acid battery a 120% volume change [9]. Research is now focused on selectively choosing intermetallic materials to minimize the initial capacity loss and electrode pulverization caused by volume expansion.

2.3 Antimonide specific alloy materials

Research on intermetallic anode materials is now focused on developing compounds where the lithiated compound strongly resembles the parent compounds, with minimal volumetric changes or structural distortions [2, 9, 15-18]. Minimizing effects of volume changes would improve the initial capacity loss, loss of active material due to pulverization or delamination, and Li trapping which lowers the capacity. A few of these materials with strong structural relationships between the parent and lithiated compound

have been identified including: InSb, Cu_2Sb, MnSb, and Mn_2Sb [2]. Antimonide-specific alloy materials show much promise because in many systems, the antimony exists in a fcc array which, while expanding slightly upon lithiation, also provides excellent structural stability minimizing electrode pulverization. InSb, Cu_2Sb, MnSb, and Mn_2Sb have different reaction mechanisms with lithium. Additionally, each compound has supporting experimental data that shows each has good cycling ability and capacity when compared to graphite.

Indium antimonide is a zinc-blende structure that provides a cubic 3D framework for lithium to occupy. The reaction of lithium with InSb is given in Eqs. 2.1 and 2.2 [2, 16].

$$2Li + InSb \rightarrow Li_2InSb \quad [2.1]$$

$$Li_2InSb + Li \rightarrow Li_3Sb + In \quad [2.2]$$

The lithium is inserted into and the indium extruded from a fcc antimony array. It is proposed that this transition occurs through a $Li_xIn_{1-y}Sb$ intermediate where the lithium substitutes for the indium [17, 18]. Experimentally, InSb electrodes can provide a capacity of 250-300 mAh/g while the theoretical gravimetric density is 350 mAh/g. The volumetric expansion of the antimony array in InSb during lithiation is 4.4%. When taking into account the extruded indium, the volume expansion becomes 46.5%. This change in volume is small compared to the 120% and 130% expansion experienced by commercially available lead acid or Ni/Cd batteries. The small volume change improves battery cycle life and reduces active material loss due to electrode pulverization. The

lithiation described in Eq. 2.2 is reversible so that lithium is extruded and indium inserted, but sintering and agglomeration of extruded indium only allows approximately 60% of the extruded indium to be reversibly intercalated [2]. Although the InSb electrode has good experimental gravimetric density and undergoes minimal volume expansion on lithiation, indium is expensive and scarce which drives up the cost of manufacturing.

Copper antimonide (Cu_2Sb) anodes have a capacity similar to graphite (332 mAh/g) and operate similarly to InSb except Cu_2Sb exhibits superior cycling behavior. Additionally, compared to indium, copper is abundant, cheap, and inert with respect to lithium. Unlike InSb, when copper is extruded the sintering and grain growth of the particles is slow, which allows for reintercalation of the extruded copper upon discharge. Experimentally, Cu_2Sb electrodes provide a capacity of 290 mAh/g with excellent cycling efficiency [2]. Cu_2Sb lithiates to Li_3Sb through an intermediate Li_2CuSb as shown in Eq. 2.3 and 2.4 [15].

$$3Li + Cu_2Sb \rightarrow Li_2CuSb + 2Cu \quad [2.3]$$

$$Li_2CuSb + Li \rightarrow Li_3Sb + Cu \quad [2.4]$$

During lithium intercalation, part of the copper is extruded from the parent compound followed by complete displacement by lithium in the second step. During lithiation, the antimony fcc array acts as a matrix material and expands 25% and another 13% upon each step shown in Eqs. 2.3 and 2.4, respectively. The total volume expansion from parent to lithiated form is 41%. When lithium is removed, the exceptional diffusion of copper into antimony aids in the reintercalation of copper into the fcc antimony array.

Fransson *et al.* reported that after 25 cycles, 90% of the theoretical capacity of Cu_2Sb was maintained [20]. The excellent cycling properties of Cu_2Sb can be partially attributed to the strong structural relationship between the parent Cu_2Sb and lithiated Li_3Sb compounds and to the excellent diffusion of copper in antimony. Although Cu_2Sb exhibits good cycling stability and reasonable capacity values, other materials with similar qualities exist with higher theoretical gravimetric and volumetric energy densities.

Manganese antimonides (Mn_2Sb and MnSb) are of the Cu_2Sb-type and NiAs-type structures, respectively. The theoretical capacities for these materials are 348 mAh/g and 454 mAh/g, respectively. The reactions with lithium and MnSb are given in Eqs. 2.5 and 2.6 [15, 21, 22].

$$MnSb + Li \rightarrow LiMnSb \quad [2.5]$$

$$LiMnSb + 2Li \rightarrow Li_3Sb + Mn \quad [2.6]$$

The volume expansion for the lithiation of MnSb given in Eq. 2.5 is 50% and during the step shown in Eq. 2.6 the fcc array of antimony is maintained and expands 12%. The total volume expansion for both steps that occurs with the full lithiation of MnSb to Li_3Sb is 68%. The volume expansion is larger than that of InSb and Cu_2Sb, but the theoretical capacity of MnSb is higher. Understanding the mechanism of lithiation and delithiation allows for the discovery of sources of capacity loss so those areas may be improved. The transition of a MnSb zinc-blende framework to a layered LiMnSb arrangement requires the displacement of half of the Mn atoms in the unit cell into adjacent interstitial sites. The intercalated lithium atoms occupy tetrahedral sites to yield the layered antifluorite-

type LiMnSb [15, 21, 22]. The extrusion of Mn and intercalation of Li occur simultaneously. During the transition from LiMnSb to Li_3Sb, lithium replaces tetrahedrally coordinated Mn atoms and also occupies octahedral interstitial sites of the Sb array. The kinetics of the electrochemical reaction is limited by the diffusion of both Mn and Sb in the transition of MnSb to LiMnSb and Li_3Sb. This reaction is reversible and highlights the strong structural relationship between MnSb and Li_3Sb. A similar lithiation and delithiation pathway occurs for Mn_2Sb electrodes. Mn_2Sb reacts with lithium as described in Eq. 2.7.

$$Mn_2Sb + 3Li \rightarrow Li_3Sb + 2Mn \qquad [2.7]$$

Upon delithiation, this reaction is not fully reversible. Instead, the reverse of Eqs. 2.5 and 2.6 occurs where Li is extruded from Li_3Sb to form LiMnSb then MnSb as manganese diffuses into the antimony array. MnSb is formed upon the recharge of Li/Mn_2Sb cells, demonstrating the difficulty intermetallic electrodes have in reincorporating extruded metal back into the parent compound [2]. The manganese extruded from the Mn_2Sb structure that is not reintercalated upon discharge adds weight to the battery while not contributing to the capacity. This is a large source of initial capacity loss in Mn_2Sb electrodes.

On long-term cycling both MnSb and Mn_2Sb electrodes contain LiMnSb and MnSb when fully charged [15]. This reinforces the idea that Mn_2Sb is not reformed upon discharge. Over time Mn_2Sb electrodes will convert to MnSb. Both MnSb and Mn_2Sb electrodes show stable cycling behavior with capacities of 335 and 260 mAh/g,

respectively. The capacity for Mn_2Sb is lower than MnSb because the second Mn in Mn_2Sb does not contribute to the electrode capacity which is also reflected in the theoretical capacities for these materials [15]. Manganese antimonide electrodes suffer from initial capacity losses due to the difficulty of reintercalation of extruded manganese. This is partially due to the poor diffusion of manganese in antimony. Instead of lithium insertion into an expanding antimony array, as occurs in MnSb and Mn_2Sb lithiation, a different intercalation mechanism called quasi-intercalation, demonstrated by the lithiation of ZnSb, also preserves similarities between a parent and lithiated compound.

Zinc antimonide (ZnSb) has an orthorhombic puckered layer structure. Based on XRD, the *first* charge/discharge of ZnSb occurs as shown in Eqs. 2.8 and 2.9, respectively, where $0 \leq x \geq 2$ [23].

$$ZnSb + 4Li \rightarrow LiZnSb + 3Li \rightarrow Li_3Sb + Zn + Li \rightarrow Li_3Sb + LiZn \quad [2.8]$$

$$Li_3Sb + LiZn \rightarrow Li_3Sb + Zn + Li \rightarrow Li_2ZnSb + 2Li \rightarrow Li_{2-x}ZnSb + xLi \quad [2.9]$$

ZnSb is lithiated to Li_3Sb through a LiZnSb intermediate followed by the lithiation of the extruded Zn. Upon discharge, the original ZnSb structure is not maintained. Instead, on the second and subsequent charges/discharges lithiation and delithiation occurs as shown in Eqs. 2.10 and 2.11, respectively, where $0 \leq x \geq 2$. [23]

$$Li_{2-x}ZnSb + xLi \rightarrow Li_2ZnSb + 2Li \rightarrow Li_3Sb + Zn + Li \rightarrow Li_3Sb + LiZn \quad [2.10]$$

$$Li_3Sb + LiZn \rightarrow Li_3Sb + Zn + Li \rightarrow Li_2ZnSb + 2Li \rightarrow Li_{2-x}ZnSb + xLi \quad [2.11]$$

Unlike the other metal antimonides discussed earlier, the intercalation of lithium into ZnSb is described as "quasi-intercalation" [23]. This is defined as the manner in which a layered structure converts into another layered structure, consisting of host atoms and periodic Li arrays, through electrochemical recrystallization upon lithiation. During lithiation, Li is inserted into the puckered channels of ZnSb. Then, the puckered channels convert into hexagonal channels, inducing rearrangement to the layered ZnSb planes with regular Li arrays. It has been shown that ZnSb electrodes exhibit fast rate capability and long cycle retention [23]. Table 2.1 summarizes the rate, volumetric, and gravimetric capacity of ZnSb electrodes where C is the theoretical capacity of the material.

Table 2.1. Summary of cycling rate and corresponding gravimetric and volumetric density for ZnSb electrodes.

Rate	Capacity (mAh/g)	Capacity (mAh/cm^3)
0.2C	140	895
5C	100	639
10C	82	524

Table 2.1 shows that at a rate of 0.2C the capacity is 140 mAh/g. Increasing the rate by 25 decreases the gravimetric capacity by 29%. Further increasing the cycling rate to 10C results in a capacity of 82 mAh/g. The corresponding volumetric energy densities range between 895 mAh/cm^3 and 524 mAh/cm^3. After 1000 cycles, 80% of the capacity of the first discharge was maintained [23]. These data show the quasi-intercalation of lithium into a parent host is another way to preserve the structural similarities of the parent and lithiated compounds.

It has been shown that antimonide specific materials are reasonable choices for the replacement of graphite as anode material in Li-ion batteries. They exhibit

comparable capacity values and the initial capacity losses caused by volume expansion are minimized. Additionally, because of the relatively small volume changes that occur due to the intercalation of lithium and metal extrusion, pulverization of the electrode is minimized, allowing excellent cycle lifetimes to be achieved. Despite these improvements, the antimonide specific materials may be further improved by making them nanoscale. Nanosize electrode materials offer the following advantages: (i) high capacity due to large surface area to volume ratio, (ii) high rate capability due to smaller lithium diffusion distances, and (iii) stable cycling behavior since the nanosize material can better accommodate strain generated during the cycling process [19]. Nanomaterials, too, have their drawbacks including difficult synthesis methods, increased surface area potentially leading to increased side reactions with the electrolyte, and decreased density from the bulk [24]. Before an electrode is incorporated into a device, a synthetic method that yields pure, high-quality material is essential.

2.4 Synthetic routes to antimonide intermetallics

Most currently used electrode materials are synthesized using a high temperature solid-state method. Often referred to as a ceramic process or the "heat and beat" method, two solids A and B react to form another solid AB solely by diffusion. Because diffusion rates of solids can be low, this process often requires lengthy reaction times, which is accompanied by high-energy demands. For antimonide compounds this process also requires high pressure, as antimony has a high vapor pressure and would otherwise be sublimated. Also using this method, control over particle morphology is lost and the formation of phases stable at lower temperatures is excluded.

Instead of this ceramic process, researchers are utilizing low-temperature methods including solvothermal and hydrothermal syntheses to produce homogenous nanopowders, including metastable phases. A typical solvothermal synthesis involves reacting the desired metal/non-metal precursor salts in a basic liquid medium to promote the precipitation and growth *via* Ostwald ripening [25]. Hydrothermal methods are similar except they are performed under pressure, which allows for the precipitation of metastable phases. Solution syntheses have also been used to make multiphase alloy powders for use in multiphase composites, including Sn-Sb alloys, Ag-Sn alloys, Ag-Sb alloys, and Ag-Sn-Sb alloys which have been synthesized using $NaBH_4$ in aqueous solution with a resulting particle size of 15-70 nm [26]. A major challenge associated with this synthesis method is the presence of oxide impurities. These impurities are irreversibly reduced to the respective metal and Li_2O during the first charge. This reduces the gravimetric and volumetric density of the electrode material. Later data show some oxide impurities can be removed by washing, but an additional step to the synthesis is required. An alternative to ceramic processes and direct solution synthesis is mechanical alloying.

Mechanical milling or mechanical alloying is also a popular synthetic technique. This process requires repetitive grinding, sifting, and size reduction of the particles. Mechanical milling describes a powder of a single composition that is milled whereas mechanical alloying describes dissimilar powders wherein transfer of material occurs during milling to form a new compound [27]. Equipment needed to achieve the milling is a significant cost but the cost is low relative to other fabrication techniques like DC sputtering or physical vapor deposition [27]. Material production occurs at room

temperature and this technique is being investigated for producing materials with unique microstructures to enhance desired properties. However, contamination of the material with Fe from alloy steels used as milling media and contamination from the milling atmosphere are significant issues. Iron contamination from the milling equipment can be controlled, but not usually eliminated, by carefully choosing mill constituents [27]. Impurities introduced from the atmosphere can be controlled using high purity inert atmospheres or vacuum. The particles formed during the milling process are mixed as a multiphase composite or compressed into a film and sintered for use as an electrode material. Impurities introduced during synthesis make milling an unattractive synthetic method. The impurities decrease the overall capacity of the battery, decrease cycle stability, and contribute to irreversible capacity losses.

The previously mentioned anode synthesis methods have major challenges that make them inappropriate of bulk synthesis: difficulty of scaling up the technique for commercial applications, use of high temperature or high vacuum, cost prohibitive, and the necessity of a binder to form a composite. The addition of a binding matrix adds complexity to the anode processing and makes characterization of the material during cycling procedures difficult. The objective of this research is to synthesize ZnSb, MnSb, and Mn_2Sb via electrodeposition of thin film directly onto a copper current collector. This allows battery testing to proceed without a binder and allows for easy characterization of the electrodeposited material. The technique of electrodeposition will be discussed in the next chapter.

2.5 References

[1] B. Markovsky, M.D. Levi, D. Aurbach, *Electrochim. Acta* 43 (1998) 2287-2304.
[2] M.M. Thackeray, J.T. Vaughey, L.M.L. Fransson, *JOM-J. Min. Met. Mat. S.* 54 (2002) 20-23.
[3] Y. Qi, S.J. Harris, *J. Electrochem. Soc.* 157 (2010) A741-A747.
[4] H. Bryngelsson, J. Eskhult, L. Nyholm, K. Edstroem, *Electrochim. Acta* 53 (2008) 7226-7234.
[5] H. Mukaibo, T. Sumi, T. Yokoshima, T. Momma, T. Osaka, *Electrochem. Solid-State Lett.* 6 (2003) A218-A220.
[6] W.-H. Pu, J.-G. Ren, C.-R. Wan, Z.-M. Du, *Electrochim. Acta* 19 (2004) 86-92.
[7] W. Yu, P. Wang, D. Yu, N. Zhang, S. Zhang, *ECS Trans.* 11 (2008) 149-155.
[8] H. Morimoto, S.-i. Tobishima, H. Negishi, *J. Power Sources* 146 (2005) 469-472.
[9] W.-J. Zhang, *J. Power Sources* 196 (2011) 13-24.
[10] S. Ohara, J. Suzuki, K. Sekine, T. Takamura, *J. Power Sources* 136 (2004) 303-306.
[11] T. Takamura, S. Ohara, M. Uehara, J. Suzuki, K. Sekine, *J. Power Sources* 129 (2004) 96-100.
[12] Y.S. Hu, P. Adelhelm, B.M. Smarsly, J. Maier, *Chemsuschem* 3 (2010) 231-235.
[13] E. Yoo, J. Kim, E. Hosono, H.-s. Zhou, T. Kudo, I. Honma, *Nano Lett.* (2008) 2277-2282.
[14] M. Noel, R. Santhanam, *J. Power Sources* 72 (1998) 53-65.
[15] L.M.L. Fransson, J.T. Vaughey, K. Edstrom, M.M. Thackeray, *J. Electrochem. Soc.* 150 (2003) A86-A91.
[16] K.C. Hewitt, L.Y. Beaulieu, J.R. Dahn, *J. Electrochem. Soc.* 148 (2001) A402-A410.
[17] C.S. Johnson, J.T. Vaughey, M.M. Thackeray, T. Sarakonsri, S.A. Hackney, L. Fransson, K. Edstrom, J.O. Thomas, *Electrochem. Commun.* 2 (2000) 595-600.
[18] J.T. Vaughey, J. O'Hara, M.M. Thackeray, *Electrochem. Solid St.* 3 (2000) 13-16.
[19] C.-M. Park, H.-J. Sohn, *Electrochim. Acta* 54 (2009) 6367-6373.
[20] L.M.L. Fransson, J.T. Vaughey, R. Benedek, K. Edstrom, J.O. Thomas, M.M. Thackeray, *Electrochem. Commun.* 3 (2001) 317-323.
[21] C.M. Ionica, P.E. Lippens, J.O. Fourcade, J.-C. Jumas, *J. Power Sources* 146 (2005) 478-481.
[22] C.M. Ionica-Bousquet, M. Womes, P.E. Lippens, J. Olivier-Fourcade, B. Ducourant, A.V. Chadwick, *Hyperfine Interact.* 167 (2006) 773-778.
[23] C.M. Park, H.J. Sohn, *Adv. Mater.* 22 (2010) 47-52.
[24] P.G. Bruce, B. Scrosati, J.-M. Tarascon, *Angew. Chem. Int. Edit* 47 (2008) 2930-2946.
[25] J.M. Tarascon, N. Recham, M. Armand, J.N. Chotard, P. Barpanda, W. Walker, L. Dupont, *Chem. Mater.* 22 (2010) 724-739.
[26] M. Wachtler, M. Winter, J.O. Besenhard, *J. Power Sources* 105 (2002) 151-160.
[27] C.C. Koch, J.D. Whittenberger, *Intermetallics* 4 (1996) 339-355.

CHAPTER 3

ELECTRODEPOSITION OF MATERIALS

3.1 Electrodeposition introduction

The previous chapter discussed commonly used synthesis techniques for battery electrode materials. The choice of synthesis routes is very important in determining the purity and quality of the resulting material. The energy density of electrode materials is directly related to the lithium diffusion distance and the presence of impurities. The common synthesis techniques described in the previous chapter shared the following two main challenges: (i) high energy input which would make commercial production cost prohibitive and (ii) the final product must be dispersed in a binding material in order to make contact with the current collector and promote particle-particle contact. The use of a binder adds weight to the battery, and because the binder is often an inactive material it does not contribute to the capacity. Also, when a binder is used the mechanism of lithium intercalation/deintercalation is difficult to characterize using common analysis techniques including: x-ray diffraction (XRD), transmission electron microscopy (TEM), x-ray photoelectron spectroscopy (XPS), and energy dispersive x-ray spectroscopy (EDS). The issue of the required binder makes the exploration of new electrode materials difficult since the charge/discharge processes cannot be adequately characterized. Electrodeposition is an attractive alternative to traditional solid-state methods for synthesizing new electrode materials with new morphologies. It allows for the direct

deposition of electrode materials on a conducting substrate and the films are readily characterized using common analysis techniques.

Electrodeposition is the process by which electroplating occurs. Electroplating is widely used for the fabrication of decorative and/or protective coatings [1]. These coatings include metals and alloys which impart scratch resistance or corrosion protection. Substrates with complex shapes can be conformally coated in a dense film, unlike a physical vapor deposition method, which yields porous films. Deposition occurs when metal ions in solution are moved to the electrode surface by means of an electric field, where they are reduced and coat the electrode with a thin layer. Codeposition occurs when two or more ions are reduced and coat the electrode surface. The simplest relation between electrode potential and deposition is described by the Nernst equation which defines the equilibrium condition of a reversible codeposition. In practice, there are few known examples of equilibrium codeposition [2]. However, the idea of the diffusion layer introduced by Nernst is an easy way to visualize time-dependent effects of current flow through an electrode.

The region near the surface of the electrodepositing metal can be described by the metal surface, electrical double layer, diffusion layer, and bulk electrolyte. During electrodeposition, metal is continually removed from solution adjacent the cathode. Diffusion, electrical migration, and convection replace the metal at the cathode-solution interface. A cartoon depiction of these layers is shown in Figure 3.1.

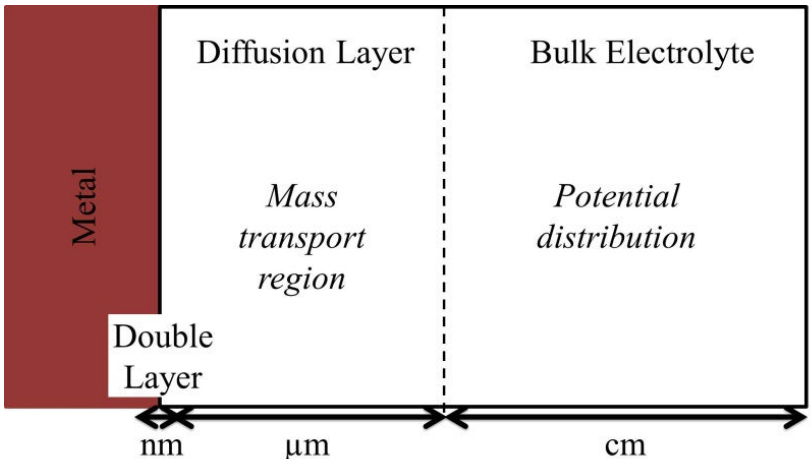

Figure 3.1. Length scales of electrochemical deposition. Adapted from Landolt *et al*. [3]

The electrical double layer consists of two parallel layers of charge on the electrode surface formed to maintain charge balance. The depletion region corresponds to a concentration gradient and extends a few microns away from the electrode surface. Convection determines the thickness of this layer. In the bulk electrolyte region, the concentration of the electrolyte is constant. Characterization of the diffusion and electrolyte layers is important in electrodeposition. A non-uniform potential distribution in the electrolyte layer leads to non-uniform current distribution on the electrode resulting in an uneven deposit of varying thickness and composition [4]. Additionally, the size of the diffusion layer controls the amount of metal available at the electrode surface. To obtain conformal coatings during the electrodeposition process, metals must be available at the electrode surface and a uniform current density must be achieved.

Although single metallic elements are most commonly electroplated, binary and ternary compounds can also be deposited using electrodeposition [5-7]. The main goal of this work is to electrodeposit high-quality thin films of ZnSb, MnSb, and Mn_2Sb from

aqueous solution at a single potential. First, the electrodeposition of pure Sb, Zn, and Mn metals will be described followed by the deposition of binary compounds.

3.2 Metal deposition

Antimony metal has been deposited from aqueous solutions of tartaric acid in crystalline form, as a powder, and as a bright mirror [8-11]. Also, Sb has been deposited from citrate baths [12]. It has been shown that Sb can be deposited on copper substrates [13]. At room temperature, Sb is rhombohedral, whereas copper is cubic. It has been shown that Sb grows in a heteroepitaxial manner and the Sb film has good adhesion to copper substrates [13]. The good adhesion of the Sb to the Cu substrate allows for excellent electrical contact.

Manganese has also been deposited from aqueous solution on stainless steel substrates at room temperature from baths containing ammonium sulfate. [14, 15] At low current density, deposits of crystalline manganese were formed, while at high current density amorphous manganese was deposited. Manganese has also been deposited from chloride baths, but chlorine gas was produced as a secondary product [16]. Manganese is difficult to electrodeposit due the highly negative potential of the Mn(II)/Mn(0) redox couple at –1.18 V vs. SHE (standard hydrogen electrode). The reduction is always accompanied by hydrogen evolution. Lastly, Mn is easily oxidized, so typically Mn alloy coatings such as Cu-Mn, Zn-Mn, or Co-Mn are used as protective coatings. The morphology of the Mn deposits can be controlled via the current density.

Zinc, like manganese, has been electrodeposited mainly from acid chloride baths and sulfate baths [17, 18]. Varying the applied voltage and electrolyte concentration

changes the morphology of the Zn deposits from dendritic growth to homogenous growth or mixed homogenous and dendritic growth. Homogenous growth occurs at low electrolyte concentration over a wide range of applied potentials. Dendritic growth occurs at higher electrolyte concentrations [19]. Not only can zinc be easily electrodeposited from aqueous solution, but controlling the applied potential allows the morphology of the deposit to be tuned.

For metal deposition on a given substrate, it is possible to tune the morphology of the film through deposition parameters like pH, coordinating ligands, temperature, and applied potential. This also holds true for alloy depositions. Tuning the morphology of alloy anode materials will allow for an electrode to be designed to best provide structural stability while minimizing the volume expansion. Since volume expansion of elemental electrodes results in poor cycling performance and low capacity, the focus of this discussion is on the electrodeposition of intermetallic materials that maintain structural similarities between the parent and lithiated compounds.

3.3 Alloy deposition

The deposition of intermetallic or alloy materials can proceed via normal, anomalous, and induced codeposition. In normal deposition, the more noble element deposits more readily and the composition of the film reflects the solution composition [20]. Anomalous codeposition proceeds by the preferential deposition of the less noble metal first. This behavior is seen in the deposition of the iron group metals [3, 21]. Induced codeposition is described by a metal that cannot be deposited as a pure metal, but only as an alloy. Examples include molybdenum or tungsten with iron group metals [3,

22, 23]. It is difficult to predict the composition of an electrodeposited film unless the codeposition mechanism is known. Therefore, experimentation is often necessary to deduce the codeposition mechanism or determine film composition. There are several difficulties that must be considered for the electrodeposition of intermetallic or alloy films including: solubility of metal precursors, reduction potentials of the individual metals, and the onset of hydrogen evolution.

Cu_2Sb is an attractive choice for an intermetallic anode material for Li-ion batteries that does not exhibit large volume changes during lithiation and delithiation. Cu_2Sb has been directly deposited on a conducting copper substrate from citrate baths and the material exhibits excellent electrical contact [24]. No post annealing step is required. The film was homogenous, stoichiometric, and crystalline. This system was challenging since the reduction potentials of Cu and Sb varied, and the deposition of Cu was preferred. However, the use of citrate in the deposition bath solubilized the antimony precursor, widened the electrochemical window, and brought the deposition potentials of Cu and Sb closer together so a thin film could be deposited at a single potential. The deposition proceeded via induced codeposition since Cu metal cannot be deposited directly from solution without the presence of the Sb-citrate complex [25]. Cu_2Sb has also been formed by the electrodeposition of Sb on a copper substrate then annealing to form Cu_2Sb. Copper antimonide formed in this way exhibited stable cycling capacities of approximately 290 mAh/g for more than 60 cycles [26]. Composite films composed of ball milled Cu_2Sb and graphite exhibited a rechargeable capacity of 290 mAh/g [27]. Similar performance of the electrodeposited and ball-milled Cu_2Sb shows that

electrodeposition is a viable method for synthesizing intermetallic anode electrode materials.

Another intermetallic material where the battery performance has been tested for electrodeposited and ball-milled samples is ZnSb. Zinc antimonide has been electrodeposited as nanoflakes and nanoparticle films from baths containing metal chloride precursors and ethylene glycol. The nanoflake films maintained a capacity of 500 mAh/g, and the nanowire films kept a capacity of 190 mAh/g after 70 cycles [28]. A composite mixture of ZnSb and carbon exhibited a capacity of 600 mAh/g after 100 cycles [29]. The high capacity of the electrodeposited ZnSb nanoflakes shows that electrodeposited ZnSb is useful for the deposition of pure, high-quality electrode materials.

The last two examples of the direct electrodeposition of Cu_2Sb or ZnSb directly on a conducting substrate show that the electrodes formed *via* electrodeposition perform similarly to composite electrodes. The use of electrodeposition for the synthesis of intermetallic anode materials results in a film that is used for battery testing or other applications without the need of additional binding material, while still having excellent electrical contact. Not only is the characterization of the electrode material easier, but it also lowers the weight of the non-active material in a battery, improving the gravimetric and volumetric density. This allows for the deposition of material on electrodes of different size, shape, and area.

The goals of this research are to (i) develop an electrochemical deposition method for the single potential codeposition of MnSb, Mn_2Sb, and ZnSb thin films directly on a conducting substrate from aqueous solution and (ii) improve the cycling stability of an

anode material for a Li-ion battery. Electrochemical deposition is a useful technique for the deposition of thin films due to the precise control of the reactions involved in the deposition itself, film structure, composition, and thickness. After optimizing the deposition parameters, the electrode material can be deposited and characterized. Then battery testing can be performed without a binder with the expectation that the capacity would be improved.

3.4 Challenges of codeposition

One of the biggest difficulties in codeposition is the issue of reduction potentials. Codeposition of binary and ternary materials is challenging as the reduction potential of the metals must be close to the same potential. Complexing agents or coordinating ligands are sometimes required to increase solubility of metal precursors, shift the reduction potentials of the metals, and widen the electrochemical window. Speciation of the coordinating ligand and metals is determined by solution pH. The role of complexing agents in electrodeposition is discussed in greater detail in Chapters 4 and 5. Another challenge of codeposition includes difficulty in predicting the composition of electrodeposited films based on a given set of deposition parameters. Due to the many mechanisms of codeposition and the inability to accurately predict film composition, experimentation to determine film composition is necessary instead of rationally choosing deposition bath constituents to form the desired film.

Researchers are currently working toward developing a mathematical model that predicts the composition of alloy deposits at a given set of deposition parameters. Basic rules governing the prediction of electrolytic reduction of binary compounds, including

intermetallics, have been devised through literature study and analysis of electronic structures [2]. It can be predicted if two or more metals will form a deposit on an electrode surface by considering the following factors:

1. *The similarities of atomic sizes and small lattice mismatch between the deposit and substrate favor epitaxial growth on the electrode*
2. *The reduction potential of each metal in a given electrolyte is similar*
3. *The relative concentrations of each metal in the electrolyte solution*
4. *The cathodic polarization of each metal*
5. *Onset of hydrogen evolution*

If the lattice mismatch between the desired compound and the substrate is too large, then new grains must be nucleated [2]. To determine if the depositions of ZnSb, MnSb, and Mn_2Sb on copper were favorable, the lattice parameters for each compound and constituent metal were tabulated. Table 3.1 summarizes the lattice parameters for ZnSb, MnSb, Mn_2Sb, Zn, Mn, Sb, and Cu [29-31].

Table 3.1. Summary of the lattice parameters for ZnSb, MnSb, Mn_2Sb, Cu, Zn, Mn, and Sb.

Compound	**a**	**b**	**c**
	(Å)		
Cu	3.610		
MnSb	4.12		5.74
Mn_2Sb	4.098		6.653
ZnSb	6.2016	7.7416	8.0995
Sb	4.510		
Mn	8.890		
Zn	2.660		

For epitaxial growth to occur, the lattice mismatch between the substrate and growth material typically is <10%. In some cases, if the lattice parameter of the deposit is double

the lattice parameter of the substrate, deposition will also occur. In this research, copper foil was used as the deposition substrate with a lattice parameter of 3.610 Å. Comparing the relevant lattice parameters for each antimonide compound that most closely matches the lattice parameter from the copper substrate will predict which compounds will grow epitaxially. The copper lattice parameter 3.610 Å ± 10% is 3.971 and 3.249 Å, respectively. No lattice parameter for any antimonide material or metal falls within that range. The manganese antimonides have a difference in lattice parameter match of 12% and 14% when considering the "a" lattice parameter. If the lattice parameter for copper is doubled to 7.220 Å, then ZnSb has a mismatch of 7% when considering the "b" lattice parameter and has a high probability for epitaxial growth on a copper substrate. Based on lattice mismatch alone, it is unlikely these materials will grow epitaxially on a copper substrate. However, epitaxial growth is not required for these films. Comparison of the lattice parameters is a convenient way to predict if a compound will form an electrodeposit on a given substrate.

Models that propose to explain electrodeposition processes or predict the composition of electrodeposits are highly dependent on experimental conditions including the following: the concentration of the electroactive species, electrode material, electrode preparation, pH, bath composition, additives, coordinating ligands, and temperature [19]. The multiple parameters make it difficult for a model to be accurate and widely applicable for the prediction of the composition of electrodeposited films. However, it has been shown that electrodeposition is an excellent way to produce pure, high-quality thin films with good electrical contact to a conducting substrate. Additionally, electrodeposited films exhibit similar battery performance when compared

to electrodes of the same material synthesized in a different manner. Electrodeposition is thus an appropriate synthetic method because the film thickness, composition, and morphology can easily be controlled through deposition time, bath composition, and current density.

3.5 References

[1] D. Landolt, *Fundamental Aspects of Alloy Plating*. American Electroplaters and Surface Finishers Society, Orlando, FL, 2001.
[2] R.D. Srivastava, S.K. Nigam, *Surf. Technol.* 8 (1979) 371-384.
[3] D. Landolt, *Electrochim. Acta* 39 (1994) 1075-1090.
[4] M. Datta, D. Landolt, *Electrochim. Acta* 45 (2000) 2535-2558.
[5] F.A. Kroger, *J. Electrochem. Soc.* 125 (1978) 2028-2034.
[6] T. Tetsuya, A. Satoshi, K. Susumu, L.H. Charles, *J. Electrochem. Soc.* 155 (2008) D256-D262.
[7] H. Nara, Y. Fukuhara, A. Takai, M. Komatsu, H. Mukaibo, Y. Yamauchi, T. Momma, K. Kuroda, T. Osaka, *Chem. Lett.* 37 (2008) 142-143.
[8] J.C. Ghosh, A.N. Kappana, *J. Phys. Chem.* 28 (1924) 149-160.
[9] H. Bryngelsson, J. Eskhult, K. Edstrom, L. Nyholm, *Electrochim. Acta* 53 (2007) 1062-1073.
[10] L. Chazova, *Izv. Vuz. Fiz+* 21 (1978) 1163-1166.
[11] I.O. Mazali, W.C. Las, M. Cilense, *J. Mater. Synth. Proces.* 7 (1999) 387-391.
[12] L. Li, Y.H. Xiao, Y.W. Yang, X.H. Huang, G.H. Li, L.D. Zhang, *Chem. Lett.* 34 (2005) 930-931.
[13] J.-W.Y. Ji-Hong Wu, Zhao-Xiong Xie, Qi-Kun Xue, and Bing-Wei Mao, *J. Phys. Chem. B* 108 (2004) 2773-2776.
[14] J. Gong, I. Zana, G. Zangari, *J. Mater. Sci. Lett.* 20 (2001) 1921-1923.
[15] J. Gong, G. Zangari, *J. Electrochem. Soc.* 149 (2002) C209-C217.
[16] J.E. Lewis, P.H. Scaife, D.A.J. Swinkels, *J. Appl. Electrochem.* 6 (1976) 199-209.
[17] J. Torrent-Burgues, E. Guaus, *J. Appl. Electrochem.* 37 (2007) 643-651.
[18] T. Yamashita, *J. Electroanal. Chem.* 106 (1980) 95-102.
[19] P.P. Trigueros, J. Claret, F. Mas, F. Sagués, *J. Electroanal. Chem.* 312 (1991) 219-235.
[20] R. Sudipta, M. Matlosz, D. Landolt, *J. Electrochem. Soc.* 141 (1994) 1509-1517.
[21] Z. Zhang, W.H. Leng, H.B. Shao, J.Q. Zhang, J.M. Wang, C.N. Cao, *J. Electroanal. Chem.* 516 (2001) 127-130.
[22] N.G. Eliaz, E., Modern Aspects of Electrochemistry, 2008, pp. 191-301.
[23] E.J. Podlaha, D. Landolt, *J. Electrochem. Soc.* 143 (1996) 893-899.
[24] J.M. Mosby, A.L. Prieto, *J. Am. Chem. Soc.* 130 (2008) 10656-10661.
[25] J.M. Mosby, D.C. Johnson, A.L. Prieto, *J. Electrochem. Soc.* Submitted (2010).
[26] H. Bryngelsson, J. Eskhult, L. Nyholm, K. Edstroem, *Electrochim. Acta* 53 (2008) 7226-7234.
[27] J.T. Vaughey, C.S. Johnson, A.J. Kropf, R. Benedek, M.M. Thackeray, H. Tostmann, T. Sarakonsri, S. Hackney, L. Fransson, K. Edström, J.O. Thomas, *J. Power Sources* 97-98 (2001) 194-197.
[28] S. Saadat, Y.Y. Tay, J. Zhu, P.F. Teh, S. Maleksaeedi, M.M. Shahjamali, M. Shakerzadeh, M. Srinivasan, B.Y. Tay, H.H. Hng, J. Ma, Q. Yan, *Chem. Mater.* (2011) 1032-1038.
[29] C.M. Park, H.J. Sohn, *Adv. Mater.* 22 (2010) 47-52.

[30] L.M.L. Fransson, J.T. Vaughey, K. Edstrom, M.M. Thackeray, *J. Electrochem. Soc.* 150 (2003) A86-A91.
[31] F.L. Carter, R. Mazelsky, *J. Phys. Chem. Solids* 25 (1964) 571-581.

CHAPTER 4

SOLUTION CHEMISTRY RELEVANT TO THE ZN-SB SYSTEM AND THE SINGLE POTENTIAL DEPOSITION OF ALLOY FILMS

4.1 Avoiding antimony oxide formation in aqueous solutions

In order to directly electrodeposit ZnSb from an aqueous deposition bath at a single potential, the first step was to determine the electrochemistry of both antimony and zinc precursors. First, the problem of the limited solubility of Sb_2O_3 in aqueous solution was addressed. At pH values as low as 3 the reduction of small amounts of Sb^{3+} to Sb^0 from acidic solution competes with hydrogen evolution which occurs at a less negative potential than what is required to reduce Sb^{3+} [1]. To preclude the competing hydrogen evolution, Sb^{3+} must be soluble in aqueous solutions at higher pH values or the reduction potential of Sb^{3+} must be moved to a less negative potential. According to the literature, using coordinating ligands to complex with Sb^{3+} not only increases aqueous solubility but also shifts the reduction potential so that antimony metal and metal alloys can be electrodeposited from aqueous solutions [2-8]. The reduction potential of a metal-ligand complex can be determined by cyclic voltammetry or the reversible potential for a metal-ligand complex can be estimated using Eq. 4.1.

$$E_{rev} = E^0 + \frac{2.3RT}{nF}\log K + \frac{2.3RT}{nF} log(c_{Me^{z+}}) \qquad [4.1]$$

R is the ideal gas constant (8.314 J mol^{-1} K^{-1}), T is the temperature, F is Faraday's constant (96485.3 C/mol), $c_{Me^{z+}}$ is the bulk concentration of the metal ion being deposited, and K is the stability constant of the complex [9, 10]. It can be seen that the reduction potential of the metal-ligand complex can be controlled by choice of ligand (metal-ligand equilibrium constants), temperature, and metal concentration. The Nernst equation can be expressed using concentration because in dilute solutions, the activity coefficients are close to unity. Besides improving the solubility of antimony oxide, the coordinating ligand allows for electrochemistry to be performed at higher pH because the electrochemical window can be widened to more negative potentials. Both of these consequences of ligand complexation are required for the direct electrodeposition of Zn-Sb alloy films reported in this work. Therefore, ligand selection is a critical consideration.

A ligand is an ion or molecule that binds to a metal atom to form a coordination complex. Ligands are classified in many ways including by charge, size or bulkiness, denticity, and pK_a values. Denticity refers to the number of times an individual ligand molecule can bond to a metal. Many ligands are able to bind metal ions at multiple sites due to electron pairs on more than one atom available for donation. The pK_a value indicates the level of deprotonation of the ligand at a specific site at a specific pH. For assisting in solubilizing metal precursors and electrodeposition the ideal ligand would have the following characteristics:

1. sufficiently soluble in aqueous solution
2. adequately deprotonated in the pH range 4-7
3. bind and solubilize the metal precursors

4. the reversible reduction of the metal-ligand complex must be at less negative potentials than the onset of hydrogen evolution.

It was determined that the organic ligand gluconic acid meets these criteria for use in electrodeposition.

Gluconic acid is a six carbon chain with 5 hydroxyl groups and a terminal carboxylic acid group. It is a monoprotic acid with a pK_a of 3.7. In aqueous solution, gluconic acid exists in equilibrium with glucono-δ-lactone and glucono-γ-lactone [11, 12]. The reported equilibria and equilibrium constants for gluconic acid are given in Eqs. 4.2-4.4 [12-14].

$$\frac{[H^+][GH_4^-]}{[HGH_4]+[L]} = 1.76 \times 10^{-4} \quad [4.2]$$

$$\frac{[H^+][GH_4^-]}{[HGH_4]} = 1.99 \times 10^{-4} \quad [4.3]$$

$$\frac{[HGH_4]}{[L]} = 7.7 \quad [4.4]$$

where the abbreviation HGH_4 is used for the protonated form of gluconic acid and the first H is the carboxylic acid hydrogen while the H_4 represents the hydrogen atoms on the alcohol groups. The abbreviation GH_4^- represents the deprotonated gluconic acid and L represents both the glucono-δ-lactone and glucono-γ-lactone.

Besides binding Sb^{3+}, gluconic acid also coordinates to Zn^{2+} with stability constants of log K = 6.0 and 1.7, respectively [13]. This leads to aqueous solutions containing both Sb-gluconate and Zn-gluconate complexes. Solution pH is an important parameter to consider in coordination chemistry. The coordination complexes present in solution can be tuned with pH and so can the reduction behavior. Also, the measure of deprotonation of the gluconic acid in solution with Sb^{3+} and Zn^{2+}, determined by solution

pH, also affects the reduction potential. Additionally, the electrochemical window can be expanded in the negative direction by lowering the H_3O^+ concentration. This work focuses on (i) characterizing the pH dependence of electrochemical behavior of solutions containing Sb^{3+}, Zn^{2+}, and gluconic acid and (ii) optimizing the electrodeposition of Zn-Sb thin films.

4.2 Experimental details

The aqueous solutions used to perform cyclic voltammetry experiments discussed in this chapter and for the deposition of ZnSb films discussed in other parts of this thesis were prepared with 18 MΩ-cm Millipore water. The solutions contained 100-300 mM sodium gluconate (denoted gluconic acid, Aldrich 99% minimum), 25 mM zinc acetate ($Zn(CH_3COO)_2$, Fisher) and 25 mM antimony (III) acetate ($Sb(CH_3COO)_3$, Aldrich, 99.99% metals basis). The deposition solutions were prepared by adding the gluconic acid to Millipore water followed by the addition of $Sb(CH_3COO)_3$. The dissolution was aided by mechanical stirring. Upon complete dissolution, the $Zn(CH_3COO)_2$ was added. The pH was subsequently adjusted to the desired value by the addition of ammonium hydroxide (NH_4OH, Aldrich, ACS reagent grade). The resulting solution was clear and colorless.

All cyclic voltammograms (CVs) and depositions were conducted using a three-electrode cell and a Gamry Instruments Reference 3000 potentiostat. Platinum gauze (1x1 cm^2) was used as the counter electrode, and a saturated sodium calomel electrode (SSCE, 0.236 V versus the standard hydrogen electrode) was used as the reference electrode. A platinum disc electrode (2.01 mm^2) was used as the working electrode for the CVs, and

copper flag electrodes were used for the depositions. The solutions were used as prepared with no degassing prior to electrochemical measurements or depositions.

4.3 Variation in electrochemistry in Sb-Zn-gluconate solutions

In this work, gluconic acid has been used as a coordinating ligand in deposition solutions containing both zinc and antimony. At this time, electrochemistry of these two elements studied together in gluconate solutions has not been reported. Solutions of varying pH were examined using cyclic voltammetry to study the effect of pH on the zinc and antimony reduction potentials. The first deposition solutions studied contained 200 mM gluconic acid, 25 mM $Zn(CH_3COO)_2$ and 25 mM $Sb(CH_3COO)_3$. The CV of this solution (Figure 4.1a) shows that scanning in the negative direction from a starting potential of 0.0 V vs. SSCE results in two or three reduction peaks depending on the pH followed by the evolution of hydrogen gas. The CV of the pH 5 solution shows two cathodic peaks corresponding to the reduction of antimony and zinc are seen at –1.00 V and –1.25 V, respectively, in Figure 4.1a. As the potential becomes more negative, the current increases rapidly due to the evolution of hydrogen gas starting at approximately –1.2 V. The assignment of the reduction peaks at –1.00 V and –1.25 V was made by depositing films at various deposition potentials before, between, and after the reduction peaks then examining the film composition using energy-dispersive X-ray spectroscopy (EDS).

Increasing the pH of the deposition solution from 5 to 6 significantly increases the electrochemical window. The decreased hydrogen ion concentration delays the onset of hydrogen evolution to more negative potentials. Raising the pH also changes metal-ion

binding due to changes in speciation, which may shift reduction potentials. The CV of the pH 6 solution containing antimony-zinc-gluconate in Figure 4.1a shows the presence of two cathodic peaks shifted to more negative potential values of –1.10 V, which can be attributed to the reduction of antimony, followed by the reduction of zinc at –1.40 V.

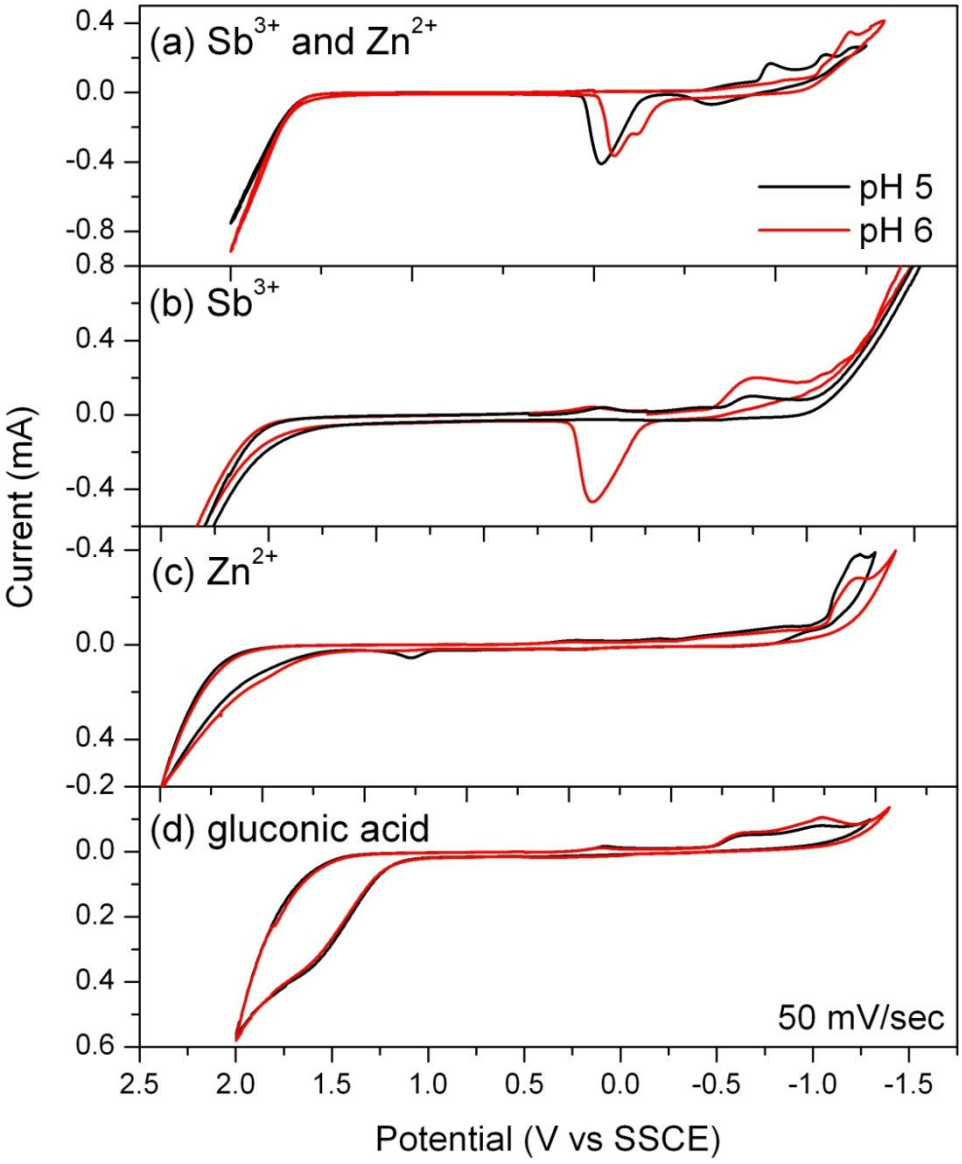

Figure 4.1. Cyclic voltammograms of solutions containing (a) 200 mM gluconic acid, 25 mM $Sb(CH_3COO)_3$ and 25 mM $Zn(CH_3COO)_2$, (b) 200 mM gluconic acid with 25 mM $Sb(CH_3COO)_3$, (c) 200 mM gluconic acid with 25 mM $Zn(CH_3COO)_2$, and (d) 200 mM gluconic acid, where pH 5 is the solid line and pH 6 is the dashed line. The reference electrode was SSCE, the working electrode was Pt, and the scan rate was 50 mV/sec.

Direct comparison of the CV of the deposition solution with the CVs from solutions containing gluconic acid only (Figure 4.1d) and gluconic acid with only antimony or zinc (Figures 4.1b, c) shows that the deposition cannot be attributed to only Sb or only Zn due to the shifting of the number and position of the oxidation and reduction peaks. These peaks are assigned on the basis of examination of the film composition of materials deposited between –1.0 and –1.5 V. Deposition at a single potential (–1.50 V) results in a film containing zinc and antimony according to EDS. Upon switching the scan direction, at pH 5 one oxidation peak is observed (Figure 4.1a) indicating there is a single oxidation process occurring at that specific potential. At pH 6 two oxidation peaks are observed at 0.1 and –0.45 V, corresponding to the stripping of antimony and zinc, respectively. The presence of the two stripping peaks indicates that zinc and antimony are deposited onto the working electrode within this electrochemical window, which is attractive because slightly acidic pH conditions preclude oxide precipitation during film deposition. The appearance of a second oxidation peak could indicate that a second species is being oxidized at the electrode surface or could be the resolution of two overlapping peaks due to the pH change. Differences in electrochemistry that results from both metal-ligand complexes in solution can be observed by looking at the redox behavior of Sb-gluconate and Zn-gluconate individually (Figures 4.1b, c).

In solutions containing Sb-gluconate, increasing the pH from 5 to 6 shows that the Sb^{3+} reduction peak shifts slightly in the positive direction (Figure 4.1b). The reduction of Sb^{3+} in the gluconate solutions occurs at approximately –0.75 V. At solution pH < 5, a large oxidation peak is present at –0.50 V, whereas at pH > 5, no oxidation peak is present. The lack of an oxidation peak in the CV indicates that Sb-gluconate is reduced at

more negative potentials than the onset of hydrogen evolution. In the presence of zinc gluconate, one or two oxidation peaks are observed for deposition solutions from pH 5-6 (Figure 4.1a).

CVs of Zn-gluconate only at pH 5 show the presence of three reduction peaks located at 0.0 V, -0.5 V, and a broad reduction peak with the center at about –0.85 V. As the pH is increased from 5 to 6, the broad Zn^{2+} reduction peak decreases in intensity and is no longer distinguishable from the hydrogen evolution, Figure 4.1c. The other two peaks do not change position and have similar intensities. Upon reversing the polarity, two anodic peaks are observed at pH 5 at 0.12 V and 0.75 V (Figure 4.1c). The peak at 0.12 V is likely due to the oxidation of Zn at the working electrode and the peak at 0.75 V is likely due to gluconate species adsorbed to the electrode surface. The lack of a stripping peak at pH 6 indicates that the deposition of zinc in inhibited when zinc is bound to gluconic acid at this pH. This was confirmed by performing constant potential experiments where the deposition potential was –1.35 V. The current-time (*i-t*) curve is shown in Figure 4.2 in addition to an image from a scanning electron microscope (SEM) showing the surface morphology of the as-deposited film.

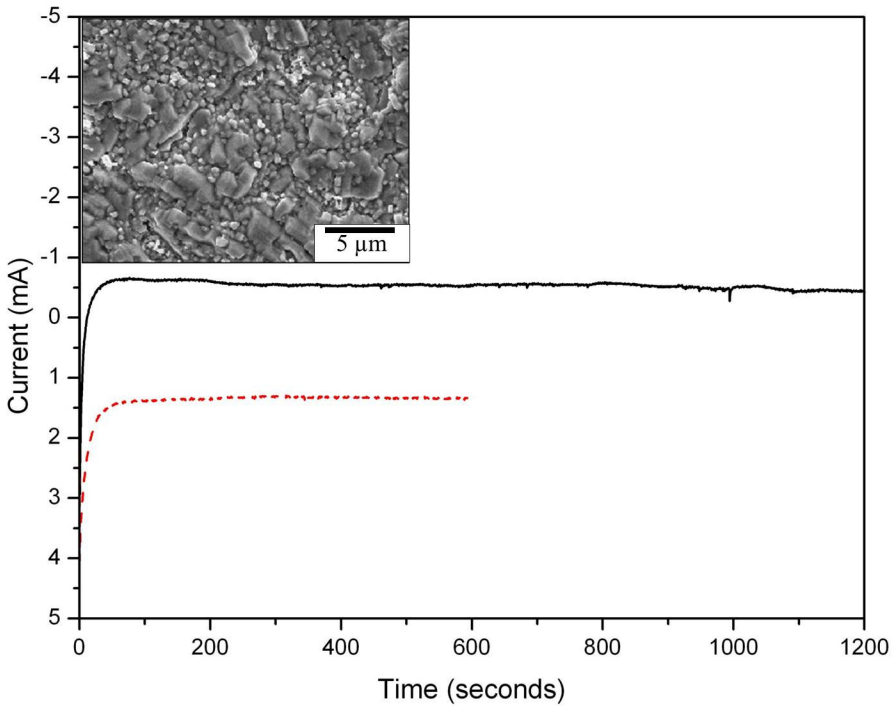

Figure 4.2. *i-t* curves of Zn deposition from aqueous solution containing 200 mM gluconic acid, 25 mM $Sb(CH_3COO)_3$ and 25 mM $Zn(CH_3COO)_2$ where the black line is the 1200-s deposition and the dashed line is the 600-s deposition. Inset: SEM image of film surface.

At a deposition time of 600 s, no visible film formed. However, after 1200 s a thin film of Zn metal was deposited on the working electrode. The absence of an oxidation peak at 0.75 V in Figure 4.1a indicates that the adsorbed surface species does not occur in solutions that also contain Sb-gluconate. Under these conditions, zinc metal is deposited when complexed by gluconate at pH 6. In the presence of Sb-gluconate, a second reduction peak is observed due to the reduction of zinc and antimony metals.

The CVs of gluconic acid only exhibits two reduction peaks shown in Figure 4.1d one attributed to a surface phenomenon on Pt (at 0.0 V) and one at –0.65 V from to the reduction of a gluconate species. Three oxidation peaks are observed from the oxidation of species adsorbed to the electrode surface and gluconate.

4.4 Variations in the electrochemistry of gluconic acid depending on pH

The function of a coordinating ligand is to solubilize metal precursors and extend the electrochemical window. In addition to the ideal ligand qualities listed earlier, it is important that the ligand is not electrochemically active. An electrochemically active ligand can reduce at the surface of the electrode which can passi2vate the surface, or add greater complexity to the characterization of reduction/oxidation chemistry of metal-ligand complexes. Therefore, consideration of the electrochemistry of the ligand is important. The pH of the solution controls the extent of deprotonation of the ligand which controls the electrochemical response as shown in Figure 4.3. Cyclic voltammograms of gluconate solutions at pH 4-7 were examined. A clear transition was observed as the pH is adjusted from 4 to 5 (Figure 4.3c, d).

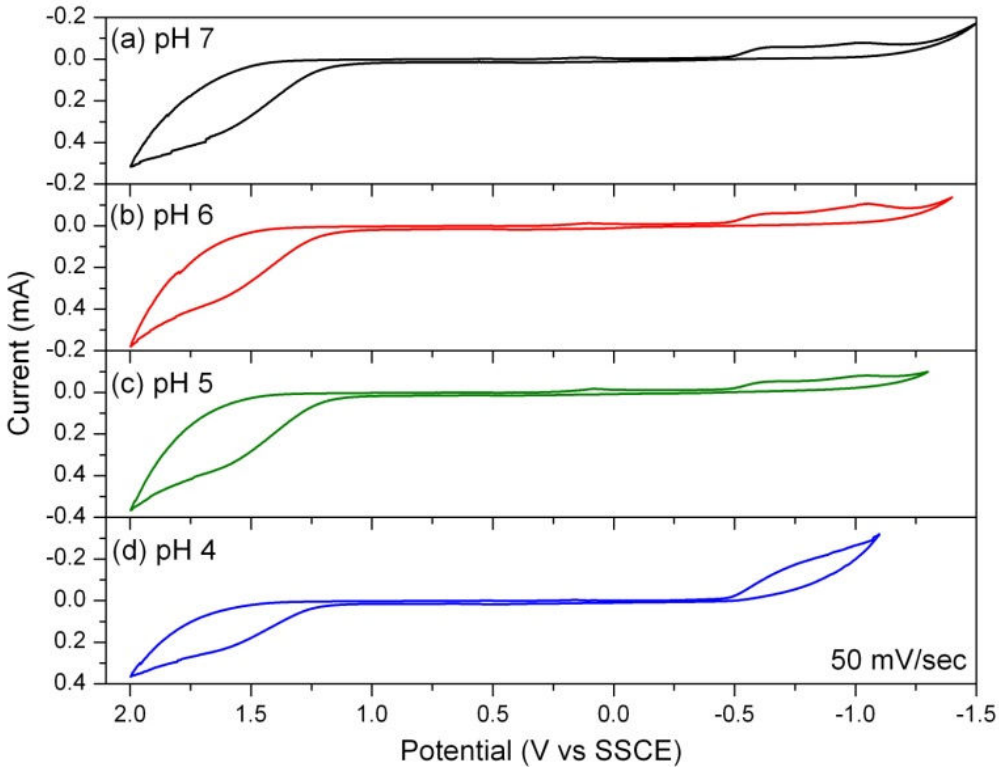

Figure 4.3. CVs of 200 mM gluconic acid at (a) pH 7, (b) pH 6, (c) pH 5, and (d) pH 4. The scan rate was 50 mV/sec and the reference electrode was SSCE.

The CVs were first scanned in the negative direction starting at 0.0 V. A small reduction peak was observed at approximately 0.0 V due to surface effects of the Pt working electrode followed by a steep increase in current due to the reduction of H_3O^+ and hydrogen gas evolution. As the pH is increased from 4 to 5, two small reduction peaks appear at –0.65 V and –1.0 V (Figure 4.3c). The onset of hydrogen evolution was not observed at –1.30 V when the polarity was switched. As the pH is further increased, the two small reduction peaks shift to slightly more negative potential values, without the steep current increase due to hydrogen evolution. Hydrogen evolution in solutions at pH 5 occurs at a potential 1.0 V more negative than solutions at pH 4 (Figure 4.3d). Increasing the electrochemical window by adjusting the pH to decrease the H_3O^+ concentration allowed for the observation of two new reduction peaks at –0.65V and –1.0 V and the suppression of hydrogen evolution (Figure 4.3a-c). There is no evidence of these peaks in CVs obtained from solutions at pH 4 due to the limited electrochemical window or overlap of hydrogen and gluconate reduction. Both peaks are present in solutions at pH 5-7 (Figure 4.3a-c) with the onset starting at the same potential at approximately –0.5 V.

The literature does not speculate on what is reduced in solutions containing gluconate. Gluconic acid is formed by the oxidation of glucose, a reaction that is irreversible, so gluconic acid is not being reduced to glucose [12]. It is commonly known that carboxylic acid functional groups can be reduced to primary alcohols according to Eq. 4.5. For the ease of discussion, the abbreviation HGH_4 is used for the protonated form of gluconic acid, where the first H is the carboxylic acid hydrogen and H_4 represents

the hydrogen atoms on the alcohol groups. The abbreviation GH_4^- represents the deprotonated gluconic acid.

$$HOOGH_4^- + 2e^- + 2H^+ \rightarrow HOGH_4^- + H_2O \qquad [4.5]$$

Additionally, the glucono-lactones can be reduced to form alcohols by first breaking the ester bond of the lactone followed by the reduction of the carboxylic acid group to the alcohol group. Both the reduction of the carboxylic acid and lactones are usually achieved using a strong reducing agent such as $LiAlH_4$ or $NaBH_4$ [15-17]. The applied potential where $[AlH_4]^-$ and $[BH_4]^-$ reduce organic species has been estimated at –0.7 V or –0.5 V vs. SSCE, respectively [17]. The identity of the species being reduced is not yet known. In order to determine which gluconic acid species are present in solution and available for reduction at specific pH values, the speciation diagram was calculated, Figure 4.4. This calculation used previously stated stability constants (298 K), as well as the equation describing the total gluconic acid concentration. Vertical lines represent the pH values of the CVs shown in Figure 4.3. In solutions where the pH is less than 3, the dominant gluconic acid species is the free acid with about 10% of the total concentration being the lactone. Beginning at about pH 3, the gluconic acid begins to deprotonate and the amount of lactone present decreases. At pH 3.7 (the pK_a of gluconic acid), half of the free acid is deprotonated. At pH 4, about 30% of the total concentration is the free acid, while most of the remaining 70% is the anion GH_4^-. As the pH is further increased to pH 5, the solution is dominated by the anion GH_4^- and the amount of lactone present

approaches zero. The speciation diagram can be used to understand the reduction behavior seen in the CVs (Figure 4.3).

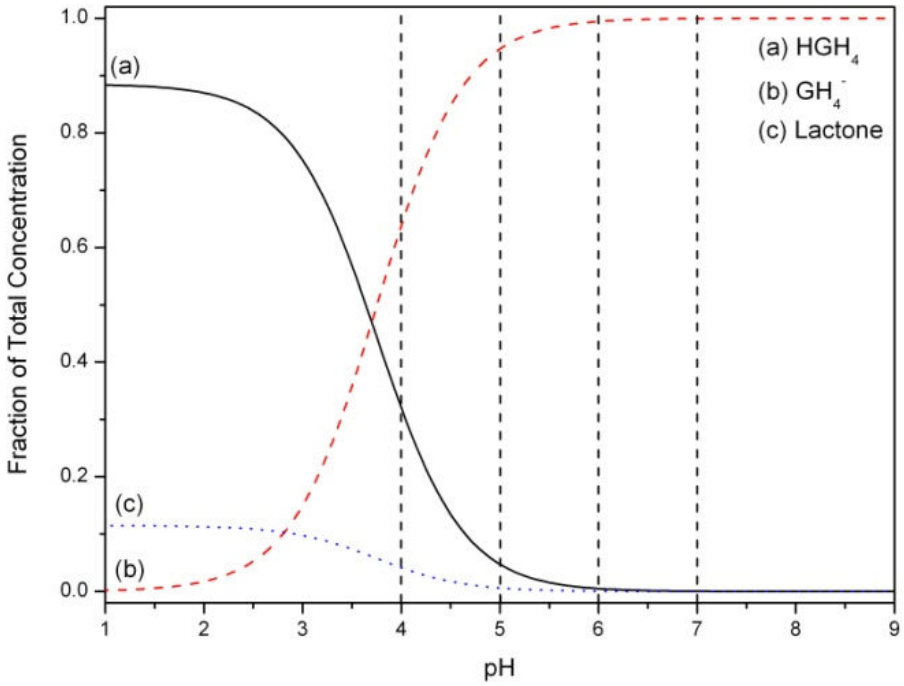

Figure 4.4. Calculated speciation diagram of 200 mM gluconic acid at 25 °C. The contribution of the (a) free acid HGH_4, (b) anion GH_4^-, and (c) lactone are shown by the solid, dashed, and dotted lines, respectively. The vertical dashed lines represent the pH values of the CVs in Figure 4.3.

The increase in cathodic current from pH 5 to 6 in Figures 4.3b and c may be attributed to a greater concentration of the anion GH_4^- and less free acid HGH_4 present in solution. No change in cathodic intensity or position is observed as the pH changes from 6 to 7 (Figure 4.3c, d) just as there is no change in the speciation diagram. At pH values greater than 6 the speciation diagram does not change, with the solution being dominated by the anion GH_4^- with the amount of free acid HGH_4 approaching zero. Therefore, variations in the composition of electrodeposited films will be controlled by the metal speciation at pH 6 or greater.

Studying the oxidation and reduction behavior has shown that gluconic acid is not significantly electrochemically active between 2.0 and -1.5 V. The reduction of carboxylic acid groups results in two small cathodic peaks. The speciation diagram for gluconic acid has also been calculated showing that in the range of pH 4-7 the dominant species is the anion, GH_4^-. It is useful to know which species are present in solution available for metal binding.

4.5 Variations in the electrochemistry of antimony-gluconate depending on pH

The improved solubility of Sb_2O_3 in solutions where a coordinating ligand was introduced was exploited to study the formation of antimony-gluconate complexes. The proposed structure of the Sb-gluconate complex includes an antimony ion coordinated to the carboxylic acid group in addition to the α- and β-OH groups [12]. Cyclic voltammograms of solutions containing 200 mM gluconic acid with 25 mM $Sb(CH_3COO)_3$ were examined from pH 4-7 (Figure 4.5). The CVs were obtained by scanning first in the negative direction between –1.6 V and –1.9 V depending on pH, and then switching the polarity and scanning in the positive direction to 2.0 V. At pH 4, a cathodic peak is observed at –0.7 V and –1.0 V, which corresponds to the reduction of antimony-gluconate depositing Sb metal on the working electrode according to Eq. 4.6, and the reduction of hydrogen begins shortly after that.

$$SbGH_4^- + 2e^- + 2H_3O^+ \rightleftharpoons Sb^0 + GH_4^- + 3H_2O \qquad [4.6]$$

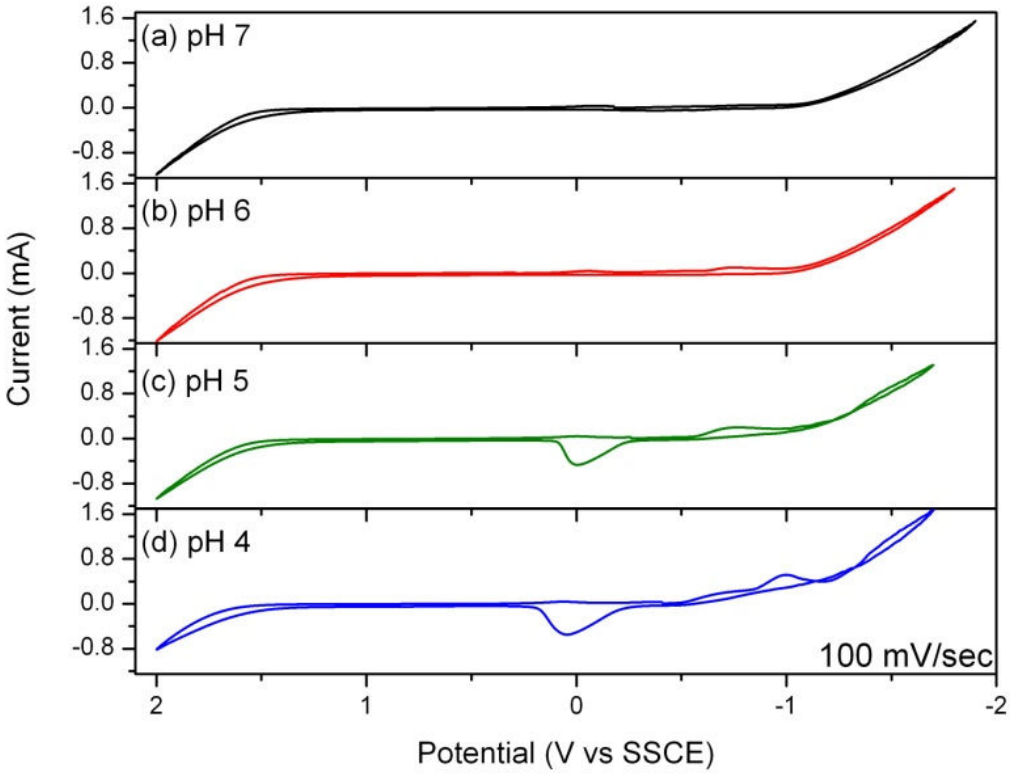

Figure 4.5. CVs of 200 mM gluconic acid with 25 mM Sb(CH3COO)3 at (a) pH 7, (b) pH 6, (c) pH 5, and (d) pH 4. The scan rate was 100 mV/sec and the reference electrode was SSCE.

An anodic peak observed at 0.05 V corresponds to the stripping of antimony off of the working electrode according to the reverse of Eq. 4.6. On the cathodic scan at pH 5, one reduction peak is observed at –0.7 V followed by the onset of hydrogen evolution at –1.0 V. As the pH is increased from pH 4 to pH 5 (Figure 4.5d, c) a single reduction peak is observed at –0.7 V. The second reduction peak seen at pH 4 is not observed at pH 5. Additionally, the anodic peak shifts to more negative potentials, from +0.05 V to 0.0 V. The anodic peak also decreases in size as the pH is increased from pH 4 to 5, indicating that more Sb metal is deposited from solutions at pH 4 than at pH 5.

As the pH is further increased to pH 6 and pH 7 (Figure 4.5a, b), the electrochemistry drastically changes. At pH 6 a small cathodic peak is present at –0.6 V

followed by the onset of hydrogen evolution at –1.0 V. At pH 7, no cathodic peaks were observed apart from the onset of hydrogen evolution, also at –1.0 V. The lack of anodic peaks shows that no antimony was deposited on the working electrode and that the reduction of antimony-gluconate to antimony metal occurs at potentials more negative than –1.8 V. The speciation diagram for gluconic acid (Figure 4.4) shows that at pH 4 (50%) and pH 5 (85%) of the gluconic acid has been deprotonated. The reduction of antimony occurs after the deprotonation of the gluconic acid. No literature was found that described the binding constants for Sb(III)-gluconate systems so no speciation diagram for Sb(III)-gluconate could be constructed at this time. A speciation diagram would be useful in determining which Sb-gluconate species are in solution and available for reduction. According to the CVs, it would be expected that SbOH-gluconate complexes would begin to form in significant amounts at pH 6. The reduction potential of SbOH-gluconate complexes would be more negative than the onset of hydrogen evolution, which is why no reduction peaks are observed in the CVs at pH 6 and 7.

4.6 Variations in the electrochemistry of zinc-gluconate depending on pH

Changes in electrochemistry of zinc-gluconate solutions depending on pH will be discussed next. There is ample literature discussing zinc-gluconate, as it has been shown that consuming zinc-gluconate lozenges reduces the length of the common cold [18-23]. However, the focus of that research has not been on zinc-gluconate electrochemistry. Instead the research focuses on the inhibition of viral replication by Zn^{2+} ions [19]. Some literature discusses the electrochemical characteristics of Zn-gluconate and more that discusses the use of gluconate in deposition baths containing zinc [13, 14, 24-29]. A

titration study of gluconate salts with zinc ions indicates that three types of zinc-gluconate complexes may exist with 1:1, 1:2, and 1:4 Zn:gluconate ratios, where the dominant ratio is concentration dependent [13]. Stability constants for metal-gluconate complexes are available in an excellent review by Sawyer [12]. Cyclic voltammetry of zinc-gluconate solutions at different pH values (Figure 4.7) will be compared to a speciation diagram (Figure 4.6) calculated using reported stability constants.

To construct a speciation diagram for metal-ligand complexes, the equilibrium constants for the metal and ligand must be known. Equilibrium constants for gluconic acid were reported earlier. The relevant equilibria and equilibrium constants at 25 °C for zinc are shown below in Eqs. 4.7-4.10 [30].

$$\frac{[ZnOH]^+}{[Zn^{2+}][OH^-]} = 1.0 \times 10^5 \quad [4.7]$$

$$\frac{[Zn(OH)_2]}{[ZnOH]^+[OH^-]} = 1.2 \times 10^6 \quad [4.8]$$

$$\frac{[ZnGH_4]^+}{[Zn^{2+}][GH_4]^-} = 50 \quad [4.9]$$

$$\frac{[ZnGH_4OH]}{[ZnGH_4]^+[OH^-]} = 1.4 \times 10^8 \quad [4.10]$$

The total zinc concentration is described by Eq. 4.11.

$$[Zinc_{Total}] = [Zn^{2+}] + [ZnOH]^+ + [Zn(OH)_2] + [ZnGH_4]^+ + [ZnGH_4OH] \quad [4.11]$$

The fraction for each species at a specific pH is calculated by simultaneously solving the equilibria expressions for gluconic acid (Eqs. 4.2-4.4), the equilibria expressions for zinc

(Eqs. 4.7-4.10), and using the expressions for the total concentration of gluconic acid and zinc. The calculated speciation diagram for zinc in the Zn-gluconate system is shown in Figure 4.6.

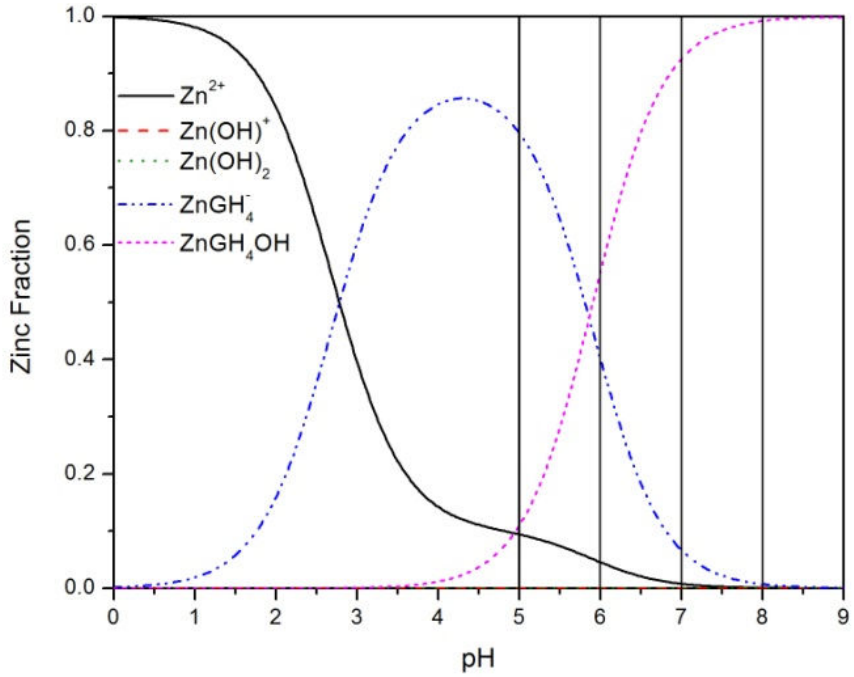

Figure 4.6. Calculated speciation diagram of zinc species in the zinc-gluconate system at 25 °C. The contribution of the Zn^{2+} (solid line), $Zn(OH)^{+}$ (dashed line), $Zn(OH)_2$ (dotted line), $ZnGH_4^{-}$ (dash-dot line), and $ZnGH_4OH$ (short dashed line) are shown. The vertical lines represent the pH values of the CVs in Figure 4.6. Fractions of $Zn(OH)^{+}$ and $Zn(OH)_2$ are two low to be distinguishable on the displayed scale.

The speciation diagram shows that at pH 1 and 2 the dominant species is free zinc. At pH 2, $ZnGH_4^{-}$ begins to form. $ZnGH_4^{-}$ is the dominant species between pH 3.5 and 6. At pH values greater than 6, $ZnGH_4OH$ is the dominant species. $ZnGH_4OH$ begins to form at pH 4 and is present with equal amounts of $ZnGH_4^{-}$ at pH 6. The zinc hydroxide species, $Zn(OH)^{+}$ and $Zn(OH)_2$ are not present in significant amounts until the pH is greater than 9. The speciation diagram will be used to help explain the reduction and oxidation behavior observed in the CVs of Zn-gluconate solutions.

The CVs of the zinc-gluconate solutions contained 200 mM gluconic acid and 25 mM $Zn(CH_3COO)_2$. The solutions were first scanned in the negative direction to a potential between –1.6 V and –1.9 V vs. SSCE depending on pH, then the polarity was reversed and scanned until 2.0 V. The CV of the pH 4 solution reveals the presence of a reduction peak at –1.25 V and two corresponding oxidation peaks at –0.6 V and 0.1 V (Figure 4.7d). Similar behavior is seen in the solution at pH 5 (Figure 4.7c) where a cathodic peak is shifted slightly to a more negative potential (–1.05 V), and a single anodic peak is observed at 0.2 V.

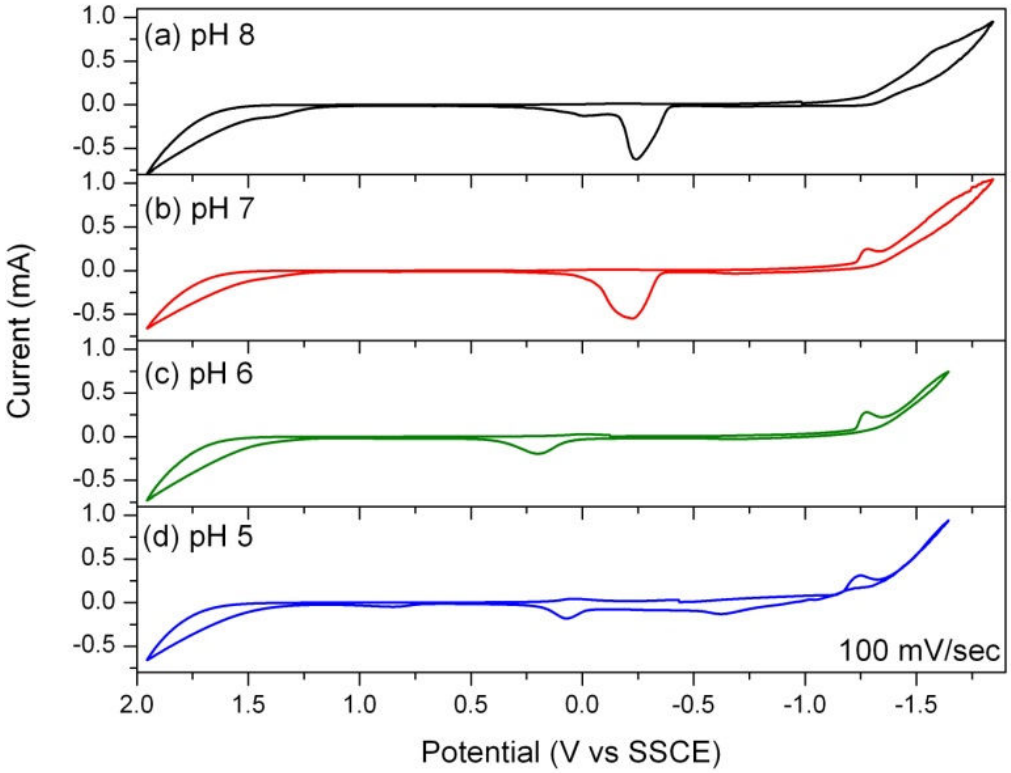

Figure 4.7. CVs of 200 mM gluconic acid with 25 mM $Zn(CH_3COO)_2$ at (a) pH 8, (b) pH 7, (c) pH 6, and (d) pH 5. The scan rate was 100 mV/sec and the reference electrode was SSCE.

According to the zinc-gluconate speciation diagram shown in Figure 4.6, the main species present in solution are Zn^{2+}, $ZnGH_4^-$, and $ZnGH_4OH$. At pH 5 those species are

present at 10%, 80%, and 10%, respectively. At pH 6 those species are present at 5%, 55%, and 40%, respectively. In addition to the zinc species, excess gluconic acid is present. As shown in Figure 4.4, at pH 5 and 6 the GH_4^- is the dominant gluconic acid species. Despite these differences in zinc speciation at pH 5 and 6, the CVs are similar. The specie being oxidized and reduced is likely not a zinc species due to the cathodic peak current being similar for both pH 5 and 6 when the speciation diagram indicates large differences in the speciation of zinc-gluconate solutions.

Between pH 6 and 7 (Figures 4.7b, c) a clear transition is observed. At pH 7 on the cathodic scan a peak is observed at –1.1 V followed by the onset of hydrogen evolution and an anodic peak at –0.25 V. The cathodic peak is similar in intensity and position to the peak observed at pH 5 and 6 (Figure 4.7c, d). However, the shifting of the anodic peak to –0.25 V indicates that something else was reduced and the peak is not visible in the CV due to hydrogen evolution. According to the speciation diagram (Figure 4.6) the difference is probably due to the increase of $ZnGH_4OH$. At pH 6 the dominant species is $ZnGH_4OH$ (55%) followed by $ZnGH_4^-$ (40%). Raising the pH to 7 results in $ZnGH_4OH$ composing 90% of the zinc speciation and at pH 8 the fraction increases to 98%. Upon scanning in the negative direction of a pH 8 solution, a reduction peak was observed at –1.6 V and was partially masked by hydrogen evolution. This probably corresponds to the reduction of the $ZnGH_4OH$ complex. It is not possible to determine if the same reduction peak occurs in solution at pH 7 due to the convolution of the hydrogen generation at negative potentials. However, the large concentration of the neutral $ZnGH_4OH$ complex and the wider electrochemical window at pH 8 allowed for the deconvolution of the cathodic peak from the hydrogen evolution. Upon reversing the

polarity, a large anodic peak is observed at –0.25 V with a shoulder located at –0.05 V. The first anodic peak is probably the dissolution of zinc metal from the Pt surface, while the second peak is likely the oxidation of an adsorbed zinc hydroxide species at the Pt electrode surface.

4.7 Variations in the electrochemistry of antimony-zinc-gluconate depending on pH

The previous sections described how the observed electrochemistry of gluconate solutions with Sb^{3+} and Zn^{2+} changes with solution pH. Now, the pH dependence of solutions containing all three components, 200 mM gluconic acid, 25 mM $Sb(CH_3COO)_3$, and 25 mM $Zn(CH_3COO)_2$, will be explained. The cathodic scan of the solution at pH 4 in Figure 4.8d shows three reduction peaks at –0.7 V, –1.0 V, and –1.3 V. The first two peaks occur at a similar potential as the peak corresponding to the antimony-gluconate reduction (Figure 4.5d). The third peak at –1.3 V may be the reduction of zinc. When the polarity was switched, a broad anodic peak is observed, with the peak maximum at 0.05 V. The position of the anodic peak is at a similar potential to antimony oxidation at pH 4 (Figure 4.5d) or zinc oxidation at pH 5 (Figure 4.7d). At this pH the CV shows that three reduction events are occurring, probably including the reduction of Sb-gluconate and Zn-gluconate.

The cathodic scan of the CV of the solution at pH 5 has three reduction peaks: the first occurring at –0.95 V, the second at –1.25 V, and the third at –1.45 V (Figure 4.8c). The first and third peaks match the potential where antimony-gluconate is reduced (Figure 4.5d). The second peak matches the potential where zinc-gluconate is reduced

(Figures 4.7b-d). The single anodic peak at 0.1 V is similar to the antimony oxidation in antimony-gluconate solution at pH 4 and 5 (Figures 4.5c, d).

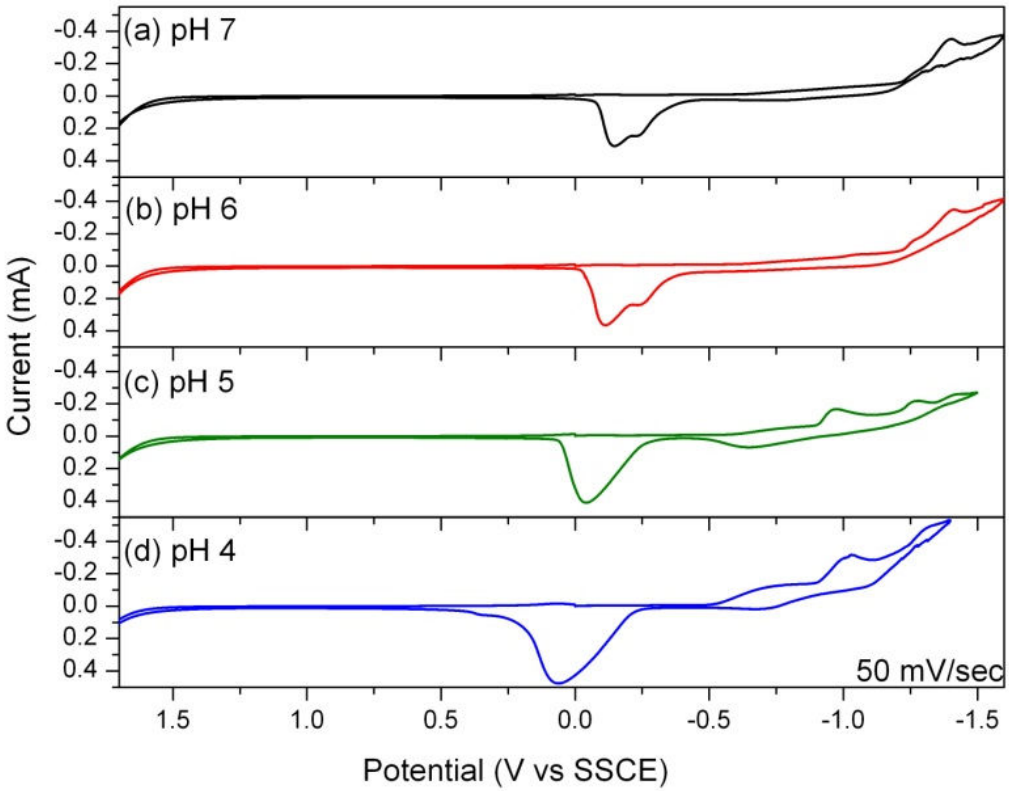

Figure 4.8. Cyclic voltammograms of solutions containing 200 mM gluconic acid, 25 mM $Sb(CH_3COO)_3$ and 25 mM $Zn(CH_3COO)_2$ at pH (a) 7, (b) pH 6, (c) pH 5, and (d) pH 4. The reference electrode was SSCE, the working electrode was Pt, and the scan rate was 50 mV/sec.

As the pH of antimony-zinc-gluconate solutions is increased from pH 5 to 6 the reduction peaks are fewer in number and occur at more negative potentials. Also, the single oxidation peak appears at more negative potentials and increases from one to two peaks (Figures 4.8a, b). Scanning solutions containing antimony-zinc-gluconate at pH 6 and 7 in the negative direction reveals one reduction peak located at –1.45 V with the onset of hydrogen evolution occurring at –1.25 V. This peak matches the potential where zinc-

gluconate is reduced at pH 8 (Figure 4.7a). This peak does not match the reduction potential of gluconate, antimony-gluconate, or zinc-gluconate reduction at any pH value. It only appears when both antimony and zinc are in solution with gluconic acid. At pH 6 and 7, the reduction peak occurring at –0.25 V matches the oxidation potential for zinc at pH 7 (Figure 4.7b). The second peak occurring at –0.12 V or –0.2 V at pH 6 and 7, respectively, appears to be unique and may be due to the oxidation of ZnSb on the Pt electrode surface.

4.8 Deposition of ZnSb alloy films

In this section, the aim is the direct electrodeposition of Zn-Sb anode materials on a conducting substrate to form Zn-Sb anodes for use in a Li-ion battery [31-33]. Electrochemical deposition is a useful technique for the deposition of thin films because it provides precise control of the reactions involved in the deposition itself, film structure, composition, and thickness [34]. This method can also be used to deposit into deep recesses and complex shapes [35, 36]. ZnSb has been successfully electrodeposited from ethylene glycol but we aim to achieve this electrodeposition using non-toxic aqueous deposition baths [37, 38].

Co-deposition of two metals is challenging because the reduction potentials and deposition rates of the two metals must be simultaneously controlled. This is especially difficult for Zn and Sb where the reduction potentials vary by approximately 967 mV in aqueous solutions. Another difficulty is the deposition solution must be slightly acidic because while antimony salts are soluble in acidic solutions, Sb_2O_3 precipitates in neutral aqueous solutions. Also, the electrodeposition of Sb is difficult in acidic solutions

because H_2 gas is evolved at potentials less negative than what is required to reduce Sb^{3+}. Coordinating ligands are therefore required to keep Sb^{3+} in solution and shift the reduction potential to less negative potentials as discussed earlier in this chapter. D-gluconic acid was chosen to keep Sb^{3+} in solution because of its history as a complexing agent [12]. The resulting complexation of the Sb^{3+} by the gluconate species allows the pH of the deposition solution to be raised without the precipitation of Sb_2O_3 and also widens the electrochemical window toward more negative potentials. Additionally, the coordinating ligand brings the reduction potentials of Sb and Zn closer together to allow for the deposition of Zn-Sb films. The electrodeposition of Zn and Sb metals was performed at room temperature at a single potential onto copper foil substrates resulting in an amorphous film of intimately mixed metals.

4.8.1 Experimental details

All the deposition solutions and baths were freshly prepared from aqueous sodium gluconate solutions ranging in concentration from 100-300 mM (denoted gluconic acid, Aldrich, 99% minimum) containing 25 mM zinc acetate ($Zn(CH_3COO)_2$, Fisher) and 25 mM antimony (III) acetate ($Sb(CH_3COO)_3$, Aldrich, 99.99% metals basis). The deposition solutions were prepared by adding the gluconic acid to Millipore water (18 MΩ-cm) followed by the addition of $Sb(CH_3COO)_3$. The dissolution was aided by mechanical stirring. Upon complete dissolution, the $Zn(CH_3COO)_2$ was added. The pH was subsequently adjusted to 4-7 by the addition of ammonium hydroxide (NH_4OH, Aldrich, ACS reagent grade). The resulting solution was clear and colorless. The

optimum solution parameters were found by varying gluconic acid concentrations, deposition temperature, and solution pH.

The films containing Zn and Sb were deposited by performing bulk electrolysis at room temperature and at a range of potential values (–0.97 to –1.50 V) vs. SSCE. The bath temperature and the applied potential were also systematically varied to determine the optimum deposition conditions.

The depositions were conducted using a three-electrode cell and a Gamry Instruments Reference 3000 potentiostat. Platinum gauze (1x1 cm^2) was used as the counter electrode, and a SSCE (0.236 V versus the standard hydrogen electrode) was used as the reference electrode. Copper flag electrodes were used for the depositions. The copper flags were foil (0.25 mm thick, 99.98% Aldrich) with an area of 1-2 cm^2. Electrical contact was made by connecting a stainless steel wire to the flag with an alligator clip. Clear nail polish was used to insulate the edges of the substrate and the back of the copper foil to ensure the deposition occurred within a controlled surface area. The depositions were carried out at a constant potential for 10-min periods. The films were rinsed with Millipore water and allowed to dry in air.

The powder X-ray diffraction patterns were obtained using Cu Kα radiation from a Scintag X-2 Advanced Diffraction X-ray cabinet system that is equipped with a stationary stage and a Peltier detector. Scanning electron microscope images of films were obtained using a JEOL JSM-6500F equipped with an energy dispersive X-ray spectroscopy (EDS) detector from Thermo Electron. An accelerating voltage of 15 kV was used to image films and collect EDS spectra. EDS data are reported as the ratio of Sb to Zn. The standard deviation was calculated from data of multiple samples at a given set

of deposition conditions. The 95% confidence interval was then calculated for each Sb:Zn ratio using the student t-test.

4.8.2 Deposition potential, pH, and film composition

A systematic investigation of the deposition parameters was conducted using baths composed of 200 mM gluconic acid, 25 mM $Sb(CH_3COO)_3$, and 25 mM $Zn(CH_3COO)_2$. Films were deposited at different potentials surrounding the cathodic peaks seen in the CV shown in Figure 4.8. The three potentials chosen varied depending on pH. For example, at pH 5 films were deposited at –0.97 V (the onset of the first cathodic peak), –1.13 V (between the cathodic peaks), and –1.30 V (after the second peak maximum). Compositional results determined by EDS are shown in Table 4.1.

Table 4.1. EDS data and corresponding 95% confidence intervals for films deposited at different potentials from solutions containing 200 mM gluconic acid, 25 mM $Sb(CH_3COO)_3$, and 25 mM $Zn(CH_3COO)_2$ at pH 6.

pH	Potential (V vs. SSCE)	Approximate Sb:Zn ratio
4	–1.00	No Zn detected
	–1.20	22 ±5
	–1.30	3.7 ±0.1
5	–0.97	No Zn detected
	–1.13	8.9 ±0.4
	–1.30	50 ±10
6	–1.25	1.5±0.1
	–1.32	1.6 ±0.3
	–1.50	5 ±2
7	–1.26	1.64 ±0.05
	–1.40	1.7 ±0.05
	–1.50	1.16 ±0.03

Films deposited from solution at pH 4 and 5 contained no zinc when the deposition potential selected was the onset of the first cathodic peak. Zinc was detected in films deposited at potentials chosen between the cathodic peaks and after the onset of the second peak. A qualitative trend is clear at pH 6 and 7, relative to the desired 1:1 Sb:Zn ratio, antimony rich films are deposited at less negative potentials and increasing amounts of zinc are deposited at more negative potentials. A 1.2:1 ratio of Sb and Zn (±10%) was achieved at these deposition conditions at room temperature. The compositional trend is consistent with the reduction peak assignments made earlier (Figure 4.8). At less negative potentials, the reduction of Sb^{3+} will occur first. Also, zinc will not be deposited from solution until the applied potential is more negative than –1.00 V. At more negative applied potentials the reduction of both Sb^{3+} and Zn^{2+} occurs such that both metals are present in similar amounts, but the films are slightly antimony rich.

4.8.3 Gluconic acid concentration, pH, and film composition

The coordinating ligand also contributes to the codeposition of these metals. Both antimony and zinc bind to gluconic acid (log K = 6.0 and 1.7, respectively). It was just shown that zinc deposition occurs at more negative potentials than antimony. The effects of altering the concentration of gluconic acid in the deposition bath were evaluated. It is expected that an increase in gluconic acid will decrease the cathodic current due to the equilibrium of metal-gluconate complexes. For example, more gluconate added the fewer free metal ions are in solution. However, a change in the peak current of Sb-gluconate is not expected because gluconate is required for the solubility of Sb in aqueous solution.

Table 4.2 summarizes the deposition parameters (where GA is gluconic acid) and the film composition as determined by EDS.

Each film was deposited after the second peak maximum for pH 4 and 5, and after the first and only peak maximum for pH 6 and 7. At a particular concentration of gluconic acid, the Sb:Zn ratio generally approaches 1:1 as the pH increases from 4 to 7. Depositions at low pH seem to be more sensitive to gluconic acid concentration.

Table 4.2. EDS data showing Sb:Zn composition ratio of films deposited at different pH values from solutions containing 100-300 mM gluconic acid, 25 mM $Sb(CH_3COO)_3$, and 25 mM $Zn(CH_3COO)_2$ at pH 4-7.

pH	Sb:Zn ratio		
	100 mM GA	200 mM GA	300 mM GA
4	No Zn detected	3.7 ± 0.1	No Zn detected
5	2.49 ± 0.04	1.38 ± 0.07	1.15 ± 0.02
6	1.0 ± 0.1	1.51 ± 0.03	1.23 ± 0.02
7	1.14 ± 0.02	1.16 ± 0.03	1.1 ± 0.2

Examination of CVs of deposition solutions containing different amounts of coordinating ligand show the electrochemical behavior becomes more similar in terms of position and number of oxidation and reduction peaks as the pH is increased from 4 to 7. Figure 4.9 shows typical CVs of pH 4 and 7 solutions containing 100 or 300 mM gluconic acid.

CVs of the pH 4 solution show an increase in intensity of oxidation and reduction peaks with increasing gluconic acid concentration. At a gluconic acid concentration of 300 mM at pH 4, two reduction peaks at approximately –0.08 V and –1.0 V are present. At 100 mM gluconic acid at pH 4, a peak is at –0.08 V and the second reduction peak is shifted to–1.10 V. CVs of the pH 7 solution show the reduction peaks do not shift

position with increasing gluconic acid concentration. The oxidation peak shifts slightly to more negative potentials. Also, as shown in Table 4.2, the Sb:Zn ratio of films deposited at pH 7 were 1.1:1 at both 100 mM and 300 mM gluconic acid. No zinc was detected in films deposited at pH 4. Additionally, a film with similar amounts of antimony and zinc can be deposited at pH 5, 6, or 7 from deposition solutions with 300 mM gluconic acid.

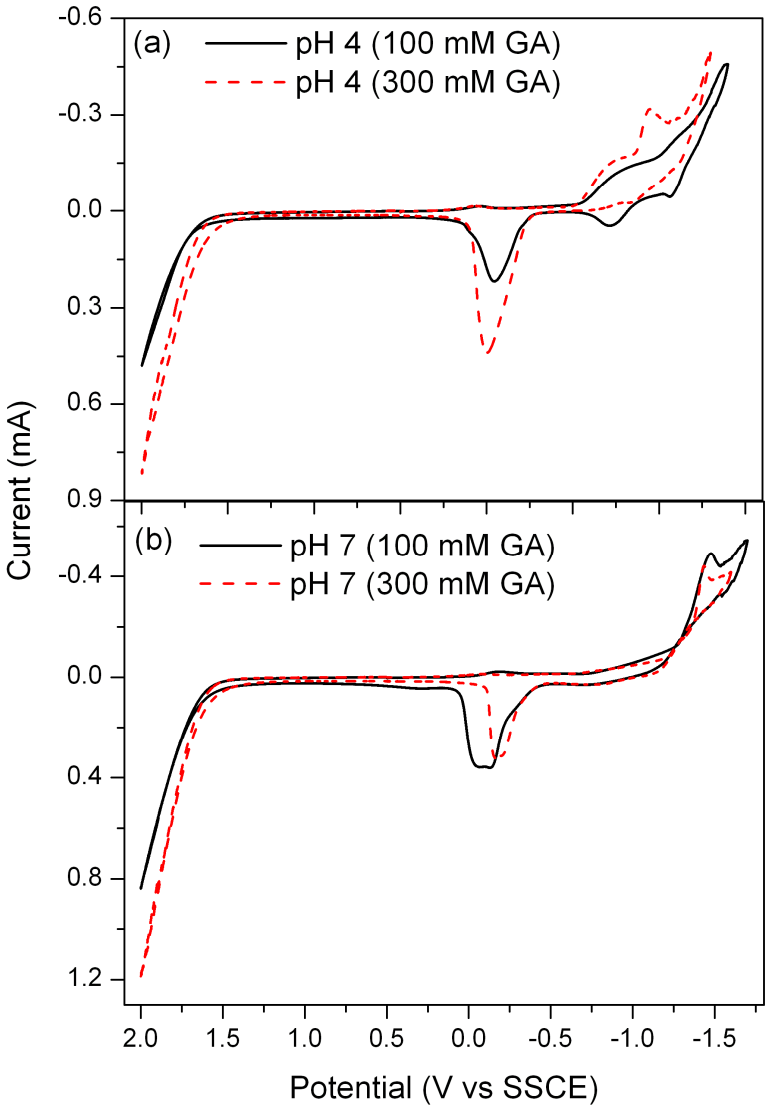

Figure 4.9. Representative CVs of deposition solutions at (a) pH 4 or (b) pH 7 with 100 mM or 300 mM gluconic acid and 25 mM each of $Sb(CH_3COO)_3$ and $Zn(CH_3COO)_2$. The CVs become more similar with increasing pH. The scanrate is 50 mV/sec.

The concentration of gluconic acid in deposition solutions is most important at low pH values. This was seen when evaluating the film composition of films deposited from solution containing 100 mM, 200 mM, or 300 mM gluconic acid. At low pH values, no trend in the film composition was observed. Examination of the CVs shows that the electrochemical behavior varies with gluconic acid concentration. On the other hand, at pH 5 and 6 the composition of the films did not change much with increasing gluconic acid concentration. The number, position, and intensity of the reduction peaks in the CVs were similar despite changes in gluconic acid concentration. The similarities in the electrochemical behavior were reflected in the similarities in film composition.

4.8.4 Bath temperature and film composition

The effect of bath temperature on the film composition formed by the electrodeposition of Zn and Sb was also investigated. Crystallinity and composition of films deposited at room temperature were compared with films deposited at 60 °C. Deposition baths contained 200 mM gluconic acid, 25 mM $Zn(CH_3COO)_2$, and 25 mM $Sb(CH_3COO)_3$. The crystallinity of the films deposited at 25 °C at different pH values was examined using X-ray diffraction (XRD). Figure 4.10 contains a representative XRD powder pattern for films deposited at room temperature from solution at pH 4, 5, and 6. At pH 5 and 6, all peaks index to copper metal, the substrate for these depositions (Figures 4.10b, c). Additional peaks in the pH 4 powder pattern are due to antimony metal. No other peaks were observed, showing the as-deposited film is amorphous. The film deposited from solution at pH 4 contained only antimony, as determined by EDS. Films deposited from solution at pH 5 and 6 contained nearly equal amounts of Sb and

Zn. At room temperature, films with nearly a 1:1 ratio of Sb:Zn were deposited at a single potential. Although it is convenient for characterization, it is not a requirement that the films be crystalline.

On the other hand, films that were deposited at 60 °C were antimony rich. The amount of antimony deposited was 2-7 times greater than the amount of zinc deposited from baths adjusted to pH 4-7. Figure 4.11 shows a representative XRD powder pattern for films deposited from solution at 60 °C and at pH 4-6.

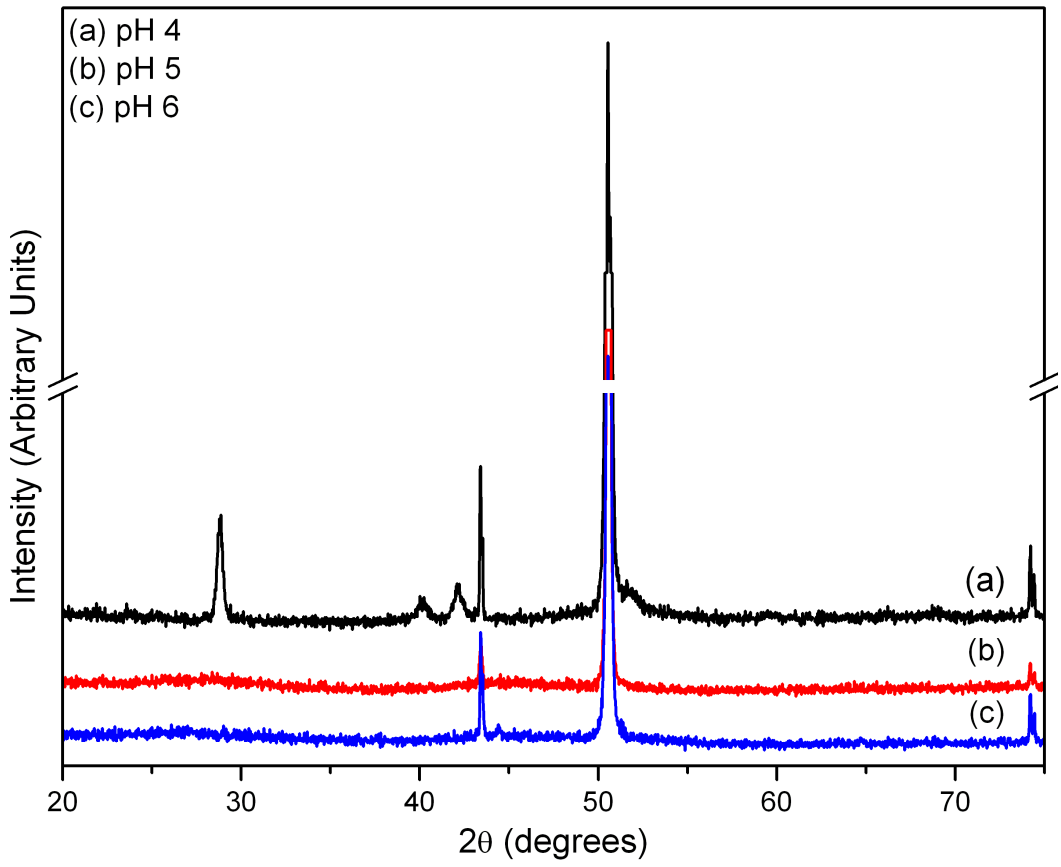

Figure 4.10. XRD pattern of films deposited from room temperature bath solutions composed of 200 mM gluconic acid, 25 mM $Sb(CH_3COO)_3$, and 25 mM $Zn(CH_3COO)_2$ at (a) pH 4, (b) pH 5, and (c) pH 6.

The copper substrate is responsible for the high intensity of the three peaks at 43, 51, and 74 ° 2θ (PDF 04-0836). All additional peaks observed in the XRD pattern correspond to Sb metal (PDF 85-1322). According to the EDS, both Sb and Zn are present in films deposited from baths at 60 °C adjusted to pH 4-7. The lack of Zn in the XRD pattern shows that Zn is amorphous.

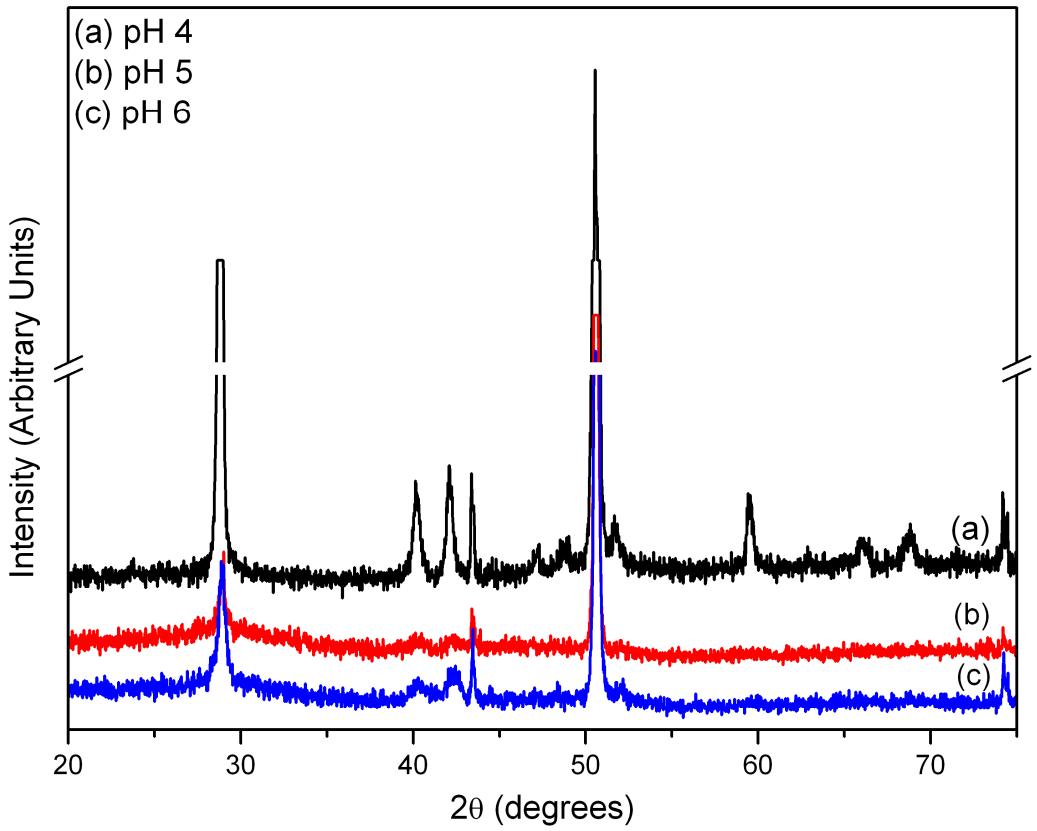

Figure 4.11. XRD pattern of films deposited from bath solutions at 60 °C composed of 200 mM gluconic acid, 25 mM $Sb(CH_3COO)_3$, and 25 mM $Zn(CH_3COO)_2$ at (a) pH 4, (b) pH 5, and (c) pH 6.

Increasing the bath temperature promoted the deposition of crystalline Sb, and in all cases, the films were antimony rich. For room temperature depositions, only films deposited from solution at pH 4 contained crystalline Sb. The observation that ZnSb did not form with gentle heating, indicates that the stability of the individual metals is

probably greater than the stability of ZnSb. Increasing the deposition bath temperature did not afford crystalline ZnSb. Instead, the simultaneous deposition of crystalline antimony and amorphous zinc from baths adjusted to pH 4-7 occurred. In order to form ZnSb from films containing Zn and Sb a post deposition annealing step may be required. Heating the film could (i) promote the diffusion of Zn into Sb an Sb into Zn and (ii) the formation of crystalline ZnSb upon cooling.

4.9 Post deposition annealing of Zn-Sb thin films

Post deposition annealing of the as-deposited Zn-Sb alloy thin films at 300 °C was completed to promote the formation of ZnSb. The high vapor pressure of antimony required the system to be under a slight positive pressure (800 torr) during the annealing process. Additionally, a clean quartz tube was used to avoid any chemical vapor transport and deposition of impurities on the surface of the tube on the films. These depositions were 10 minutes long, performed with the bath temperature raised to 60 °C. XRD patterns of as-deposited films show the film is amorphous. The only crystalline component is copper from the substrate. Annealing the film at 300 °C for 12 hours at 800 torr only succeeded in forming ZnSb. Unfortunately, crystalline Cu_4Zn (brass), Cu_2Sb, and Sb metal was also formed. Annealing a Zn-Sb film on a copper substrate yields the thermodynamically favored Cu_2Sb. To avoid the formation of brass and Cu_2Sb, films containing Zn-Sb could be deposited on gold substrates. Though the formation of ZnSb by post deposition annealing may be successful on gold substrates, the use of gold as a current collector in a battery is not useful, since gold lithiates. The lithiation and

expansion of gold would contribute to the pulverization and delamination of the electrode.

4.10 Conclusions

In this chapter, the electrochemistry of gluconic acid with antimony and zinc was shown to vary with pH due to changes in speciation. The electrochemistry of Zn-gluconate solutions was successfully explained using known stability constants used to calculate a speciation diagram for the individual metal-gluconate complexes. The speciation diagram was then used to help describe the CVs of solutions containing antimony-zinc-gluconate as well as individual Zn-gluconate solutions. The introduction of a coordinating ligand not only aided in precursor solubility, it also allowed the electrochemical window to widen, but changed the reduction potential as the metals formed complexes. This is an important start to developing an electrochemical deposition procedure for ZnSb films at a single potential from aqueous solution.

In addition, based on previous observations, films containing intimately mixed zinc and antimony were deposited at room temperature from bath solutions containing 200 mM gluconic acid, 25 mM $Sb(CH_3COO)_3$, and 25 mM $Zn(CH_3COO)_2$ at pH 6 and an applied potential of –1.47 V versus SSCE. The solution pH and deposition temperature can be used to tune to film composition. Lower solution pH and higher deposition temperatures favor higher antimony content. Changing the composition of gluconic acid in the deposition solution does not significantly affect the film composition. The formation of ZnSb was not achieved with post deposition annealing at 300 °C for 12 hours. Cu_2Sb formed during the annealing step when antimony metal reacted with copper

metal from the substrate. A different substrate is required for post deposition annealing to avoid the formation of Cu_2Sb and brass.

4.10 References

[1] M. Pourbaix, *Atlas of Electrochemical Equilibria in Aqueous Solutions*. NACE International, 1974.

[2] L. Chazova, *Izv. Vuz. Fiz+* 21 (1978) 1163-1166.

[3] J.C. Ghosh, A.N. Kappana, *J. Phys. Chem.* 28 (1924) 149-160.

[4] H.M. Hu, M.S. Mo, B.J. Yang, M.W. Shao, S.Y. Zhang, Q.W. Li, Y.T. Qian, *New J. Chem.* 27 (2003) 1161-1163.

[5] A.S. Fouda, A.K. Mohamed, *B. Electrochem.* 6 (1990) 677-678.

[6] Y. Zhang, G.H. Li, Y.C. Wu, B. Zhang, W.H. Song, L. Zhang, *Adv. Mater.* 14 (2002) 1227-1230.

[7] H. Bryngelsson, J. Eskhult, K. Edstrom, L. Nyholm, *Electrochim. Acta* 53 (2007) 1062-1073.

[8] J.M. Mosby, A.L. Prieto, *J. Am. Chem. Soc.* 130 (2008) 10656-10661.

[9] N.G. Eliaz, E., Modern Aspects of Electrochemistry, 2008, pp. 191-301.

[10] R.D. Srivastava, S.K. Nigam, *Surf. Technol.* 8 (1979) 371-384.

[11] L. Fabre, G. Fleche, P. Fuertes, P. Gallezot, A. Perrard, *Catal. Lett.* 68 (2000) 41-44.

[12] D.T. Sawyer, *Chem. Rev.* 64 (1964) 633-643.

[13] P.W. Roller, W.F. Pickering, *Aust. J. Chem.* 29 (1976) 2395-2403.

[14] V.S. Vasantha, V.S. Muralidharan, *P. Indian A. S.-Chem. Sci.* 106 (1994) 825-836.

[15] G. W. Gribble, *Chem. Soc. Rev.* 27 (1998) 395-404.

[16] R.F. Nystrom, W.G. Brown, *J. Am. Chem. Soc.* 69 (1947) 2548-2549.

[17] N.G. Connelly, W.E. Geiger, *Chem. Rev.* 96 (1996) 877-910.

[18] W. Alnakib, P.G. Higgins, I. Barrow, G. Batstone, D.A.J. Tyrrell, *J. Antimicrob. Chemoth.* 20 (1987) 893-901.

[19] G.A. Eby, D.R. Davis, W.W. Halcomb, *Antimicrob. Agents Ch.* 25 (1984) 20-24.

[20] M.L. Garland, K.O. Hagmeyer, *Ann. Pharmacother.* 32 (1998) 63-69.

[21] J.C. Godfrey, B.C. Sloane, D.S. Smith, J.H. Turco, N. Mercer, N.J. Godfrey, *J. Int. Med. Res.* 20 (1992) 234-246.

[22] S. Marshall, *Can. Fam. Physician* 44 (1998) 1037-1042.

[23] S.B. Mossad, M.L. Macknin, S.V. Medendorp, P. Mason, *Ann. Intern. Med.* 125 (1996) 81-88.

[24] E. Guaus, J. Torrent-Burgués, *J. Electroanal. Chem.* 549 (2003) 25-36.

[25] R. Renuka, S. Ramamurthy, K. Muralidharan, *J. Power Sources* 76 (1998) 197-209.

[26] J.L. Ortiz-Aparicio, Y. Meas, G. Trejo, R. Ortega, T.W. Chapman, E. Chainet, P. Ozil, *J. Electrochem. Soc.* 155 (2008) D167-D175.

[27] R.K. Cannan, A. Kibrick, *J. Am. Chem. Soc.* 60 (1938) 2314-2320.

[28] C. Panda, R.K. Patnaik, *Indian J. Chem. A* 14 (1976) 446-448.

[29] R. Sekar, S. Jayakrishnan, V.S. Muralidharan, *T. I. Met. Finish.* 83 (2005) 300-302.

[30] *CRC handbook of food additives*. 2nd ed. Furia, T.E.; CRC Press: Cleveland, OH, 1972; Chapter 6.

[31] L.P. Bicelli, B. Bozzini, C. Mele, L. D'Urzo, *Int. J. Electrochem. Sc.* 3 (2008) 356-408.

[32] R.M. Penner, *J. Phys. Chem. B* 106 (2002) 3339-3353.
[33] M.E. Hyde, R.G. Compton, *J. Electroanal. Chem.* 549 (2003) 1-12.
[34] H. Bryngelsson, J. Eskhult, L. Nyholm, K. Edstroem, *Electrochim. Acta* 53 (2008) 7226-7234.
[35] J.A. Switzer, H.M. Kothari, P. Poizot, S. Nakanishi, E.W. Bohannan, *Nature* 425 (2003) 490-493.
[36] J.A. Switzer, M.G. Shumsky, E.W. Bohannan, *Science* 284 (1999) 293-296.
[37] H. Yamamoto, K. Fujii, M. Morishita, *Electrochemistry* 74 (2006) 874-876.
[38] S. Saadat, Y.Y. Tay, J. Zhu, P.F. Teh, S. Maleksaeedi, M.M. Shahjamali, M. Shakerzadeh, M. Srinivasan, B.Y. Tay, H.H. Hng, J. Ma, Q. Yan, *Chem. Mater.* (2011) 1032-1038.

CHAPTER 5

SOLUTION CHEMISTRY RELEVANT TO THE MN-SB SYSTEM AND THE SINGLE POTENTIAL DEPOSITION OF ALLOY FILMS

5.1 Manganese chemistry in aqueous solution

The reduction of manganese from 2+ to 0 occurs at –1.42 V vs. SSCE (saturated sodium calomel electrode) in aqueous solution, making Mn the most electronegative metal that can be electrodeposited from aqueous solution [1, 2]. The highly negative potential required to reduce manganese makes the deposition sensitive to impurities and makes the deposition of Mn and its alloys difficult. Usually, manganese depositions are obtained by using deposition baths containing manganese sulfate and chloride with ammonium salts [3-5]. This is easy to achieve since manganese compounds are generally readily soluble in aqueous solution at room temperature. Hydroxide formation during the deposition is avoided by including the ammonium ion in the bath. Ammonium also improves the conductivity of the solution, and a desirable buffering effect is provided [6]. Ammonium has also been used to deposit tin-manganese alloys where the ammonium brings the deposition potential of the metals closer together allowing for the co-deposition of both metals [2].

Manganese salts are readily dissolved in aqueous solution, and the relevant reactions concerning Mn^{2+} in acidic aqueous solution in the presence of oxygen are shown in Eqs. 5.1-5.3.

$Mn^{2+} + 2e^- \rightarrow Mn^0$ E = –1.18 V vs. SHE [5.1]

$Mn^{3+} + e^- \rightarrow Mn^{2+}$ E = +1.50 V vs. SHE [5.2]

$MnO_2 + e^- \rightarrow Mn^{3+}$ E = +0.95 V vs. SHE [5.3]

These equations show that Mn^{2+} is reduced at –1.18 V vs. SHE (standard hydrogen electrode) in acidic aqueous solution. Competing with that reduction is the oxidation of $Mn^{2+} \rightarrow Mn^{3+}$ and $Mn^{3+} \rightarrow Mn^{4+}$ at –1.50 V and –0.95 V vs. SHE, respectively. To adjust the reduction potential of Mn^{2+} to a potential less negative than the onset of hydrogen evolution, a coordinating ligand is required for co-deposition applications, as was used in Chapter 4. With this in mind, a coordinating ligand that strongly binds manganese is required to avoid the competing oxidation reactions during film deposition. Besides strongly coordinating to the manganese, the newly formed manganese complex must be reduced at a potential that precludes hydrogen evolution. In addition to binding manganese, the coordinating ligand must solubilize the antimony precursor just as was done in Chapter 4.

5.2 Avoiding antimony oxide formation in aqueous solutions

The solubility of Sb_2O_3 in aqueous solution was addressed in Chapter 4.1. It was determined that gluconic acid was an excellent choice for a coordinating ligand to solubilize and coordinate metal ions in aqueous solution. However, gluconic acid is not the only appropriate coordinating ligand with the benefits of solubilizing metal precursors and widening the electrochemical window with pH. Other suitable ligands include

ethylenediaminetetraacetic acid (EDTA) and citric acid. The structures of gluconic acid, EDTA, and citric acid are shown in Figure 5.1.

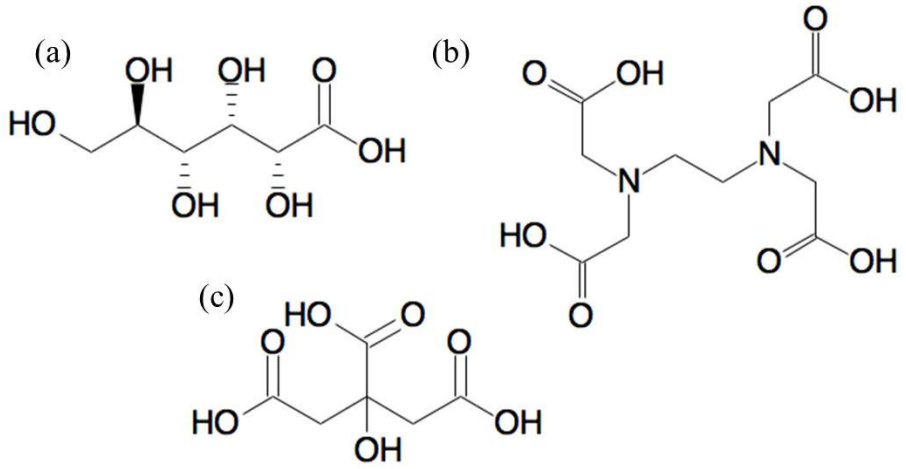

Figure 5.1. Chemical structures of (a) gluconic acid, (b) EDTA, and (c) citric acid.

Gluconic acid, EDTA, and citric acid are all soluble in aqueous solution. Additionally, the ligands have similar features including carboxylic acid groups that can be deprotonated for metal binding. Gluconic acid and citric acid have additional hydroxyl groups whereas EDTA has two amine groups. The pK_a values for each ligand determine at what pH the ligand is deprotonated and the charge. Ligand speciation and how it affects electrochemistry observed in cyclic voltammograms (CVs) will be discussed later. Now, the features of EDTA and citric acid will be discussed in detail. Gluconic acid was discussed in Chapter 4.1.

EDTA is a water-soluble polyamino carboxylic acid. It is a hexadentate ligand and is widely used to sequester metal ions. Due to its large number of coordination sites, EDTA has a high affinity for metal ions. There are six pK_a values for EDTA, the first four being for the carboxylic acid groups and the last two being for the amine groups: pK_{ai} = 0.0, 1.5, 2.00, 2.69, 6.13, 10.37 [7]. When fully deprotonated, EDTA usually binds

to metals through the two amines and four carboxylate groups resulting in an octahedral geometry. In this application, the solution pH is maintained at pH < 7 to preclude metal oxide precipitation. Therefore, the major form of EDTA present in solution is Y^{4-}, where Y^{x-} represents the EDTA anion and the x^- represents the charge. Industry widely uses EDTA as a means to sequester metal ions in solution and also to suppress catalytic activity of metal ions during certain processes. EDTA is well known for use as a water softener and in chelation therapy for arsenic, mercury, and lead poisoning [8].

The other appropriate ligand for solubilizing metal precursors and tuning reduction potentials is citric acid. Citric acid is a water soluble triprotic acid with three carboxylic acid groups and one hydroxyl group. The hydroxyl group is alpha with respect to one of the carboxylic acid groups and in the beta position with respect to the other two carboxylic acid groups. Literature states that antimony coordinates to citrate with a coordination number of four [9]. Antimony coordinates to a water molecule, hydroxyl group, and the carboxylic acid groups both alpha and beta to the hydroxyl group [10]. It has recently been shown that citric acid not only solubilizes antimony precursors and precludes antimony oxide formation, but tunes the reduction potentials of both antimony and copper to allow the direct electrodeposition of Cu_2Sb at a single potential [11].

The solution pH plays an important role in the size of the electrochemical window and controls the degree of protonation of the coordinating ligands. The degree of protonation affects metal-ligand binding as well as the reduction potential of the Sb^{3+} and Mn^{2+} complexes. These effects will be discussed later in this chapter. This work focuses on the search for appropriate coordinating ligands, bath temperature, and solution pH so

that high-quality thin films of MnSb or Mn_2Sb may be directly electrodeposited on a conducting substrate from aqueous solution at a single potential.

5.3 Experimental details

The aqueous solutions used to perform cyclic voltammetry experiments discussed in this chapter and for the electrodeposition of Mn-Sb films discussed in other parts of this thesis were prepared with 18 MΩ-cm Millipore water. The solutions contained 200 mM ligand (citrate, EDTA, or gluconate) with 25 mM manganese acetate ($Mn(CH_3COO)_2$, Aldrich), and 25 mM antimony acetate ($Sb(CH_3COO)_3$, Aldrich, 99.99% metals basis). The solutions were prepared by adding the coordinating ligand to Millipore water and waiting until complete dissolution before adding $Sb(CH_3COO)_3$. The dissolution was aided by mechanical stirring. After the dissolution of the antimony precursor, $Mn(CH_3COO)_2$ was added. The solution pH was subsequently adjusted to pH 2-8 using ammonium hydroxide (NH_4OH, Aldrich, ACS reagent grade). The resulting solutions were clear and colorless.

All cyclic voltammograms (CVs) and depositions were conducted using a three-electrode cell and a CHInstruments potentiostat. Platinum gauze (1x1 cm^2) was used as the counter electrode, and a SSCE (0.236 V versus the standard hydrogen electrode) was used as the reference electrode. For ease of discussion, all reported potential values are versus SSCE unless otherwise specified. A platinum disc electrode (2.01 mm^2) was used as the working electrode for the CVs, and evaporated copper flag electrodes were used for the depositions unless otherwise specified. Copper flag electrodes were insulated with clear nail polish on the sides and back to control the surface area of the deposition. The

solutions were used as prepared with no degassing prior to electrochemical measurements.

5.4 pH dependence of electrochemistry

5.4.1 Variation in electrochemistry in antimony-manganese-citrate solutions

Examination of the electrochemical redox behavior of deposition solutions using cyclic voltammetry allows observation of changes in reduction potential due to the addition of a coordinating ligand. Also, observation of the electrochemical behavior of Sb-ligand solutions and Mn-ligand solutions separately allows for the identification of differences in redox activity between individual Sb-ligand/Mn-ligand complexes and mixtures of both metal complexes in solution. Solutions of varying pH were examined using cyclic voltammetry to study the effects of pH and coordinating ligand on the antimony and manganese deposition potentials. The first solutions studied contained 200 mM citric acid, 25 mM $Sb(CH_3COO)_3$, and 25 mM $Mn(CH_3COO)_2$ at pH 5 and pH 7 as shown in Figure 5.2a.

Examination of the CVs of this solution at pH 5 and 7 scanning in the negative direction from an initial potential of –500 mV results in a small cathodic peak at –1.05 V followed by the onset of hydrogen evolution at –1.50 V. The pH 5 solution was not scanned far enough in the negative direction to observe hydrogen evolution. After the polarity is switched, two anodic peaks are seen at –0.20 V and –0.75 V. In the CVs of the solution containing Sb^{3+} and citric acid at pH 5 and 7, scanning in the negative direction first yields a cathodic peak observed at –1.0 V. Figure 5.2b may have an additional cathodic peak at –1.50 V, but it is overshadowed by hydrogen evolution.

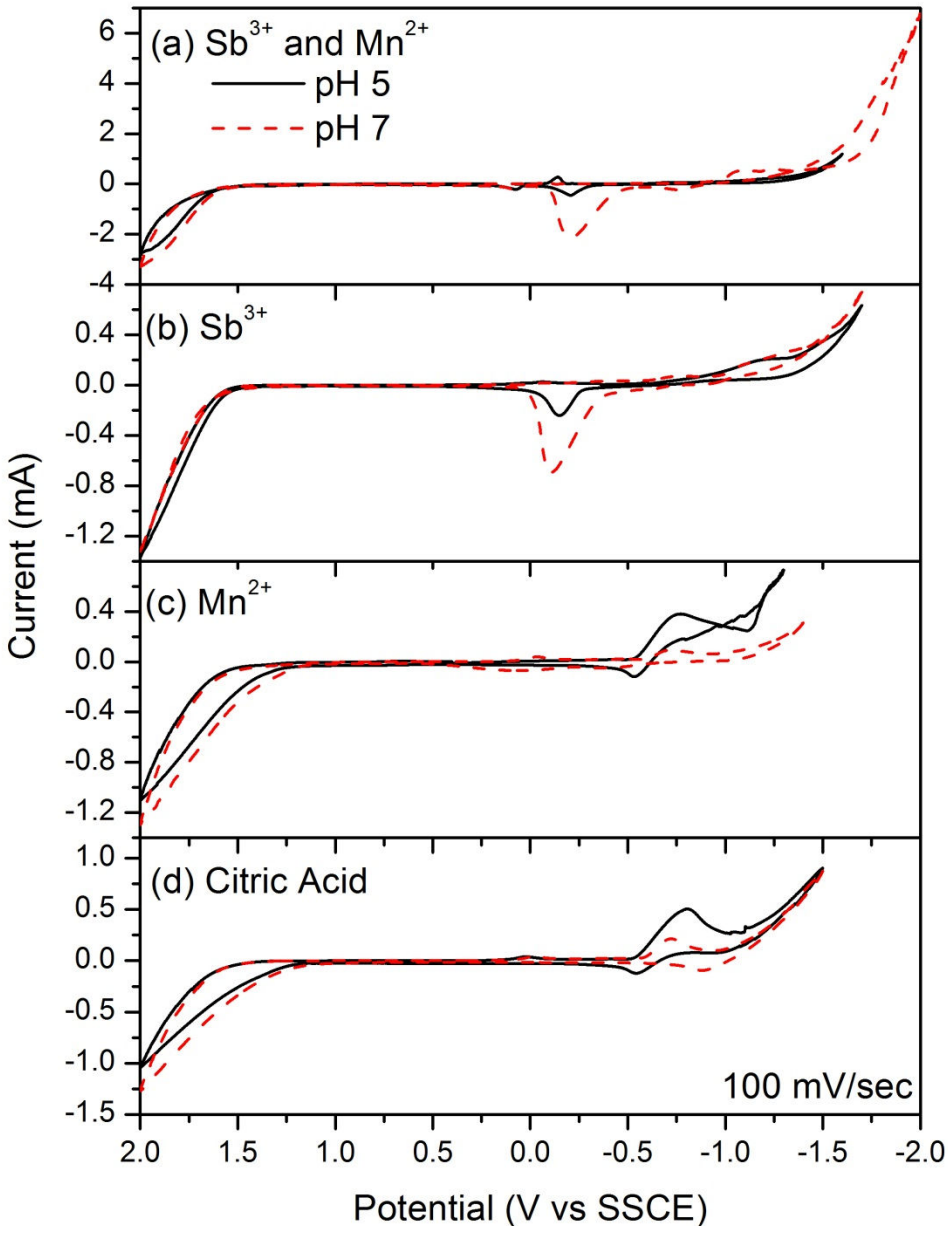

Figure 5.2. Cyclic voltammograms of solutions containing (a) 200 mM citric acid, 25 mM $Sb(CH_3COO)_3$ and 25 mM $Mn(CH_3COO)_2$, (b) 200 mM citric acid with 25 mM $Sb(CH_3COO)_3$, (c) 200 mM citric acid with 25 mM $Mn(CH_3COO)_2$, and (d) 200 mM citric acid where pH 5 is the solid line and pH 6 is the dashed line. The reference electrode was SSCE, the working electrode was Pt, and the scan rate was 100 mV/sec.

When the polarity was reversed, a single anodic peak was observed at –0.10 V. No additional anodic peaks were observed when compared to CVs of the Sb^{3+}, Mn^{2+}, and

citrate mixture. The peaks observed in the Sb^{3+}, Mn^{2+}, and citrate mixture (Figure 5.2a) seem to correspond to the reduction and oxidation of antimony citrate only based on the number and position of both the cathodic and anodic peaks in the CVs of solution containing antimony-citrate (Figure 5.2b). Similarly, comparing the CVs of citric acid and a mixture of citric acid and Mn^{2+} reveals the reduction and oxidation peaks observed in Figure 5.2c are mainly due to citric acid reduction and oxidation

Examination of the CVs of solutions at pH 5 and 7 containing Mn^{2+} and citric acid (Figure 5.2c) scanning in the negative direction from 0.0 V reveals a cathodic peak at –1.25 V in the midst of hydrogen evolution. Upon switching the polarity, an anodic peak is observed at –0.5 V in the CV of the pH 4 solution. At pH 5, no anodic peak is observed. Similarly, CVs of solutions containing citric acid only beginning at 0.0 V and scanning in the negative direction show a cathodic peak observed at –0.75 V and –0.65 V for solutions at pH 5 and 7, respectively. Switching the polarity reveals a small anodic peak at –0.5 V in the CV of the pH 5 solution and at –0.85 V in the CV of the pH 7 solution. From direct comparison of the CVs of Mn^{2+} and citric acid (Figure 5.2c) with CVs of a solution containing only citric acid (Figure 5.2d), it is clear the oxidation and reduction occurring in Figure 5.2c is due to citric acid.

Based on the CVs, antimony is electrochemically active whereas manganese is not when bound to citric acid in aqueous solution. The electrochemical behavior observed in the CVs of the Sb^{3+}, Mn^{2+}, and citrate mixture (Figure 5.2a) is similar to the behavior observed in the CVs of Sb-citrate solutions. The addition of manganese to solutions containing Sb-citrate does not shift the antimony reduction potential, as evidenced by the similar number and position of cathodic peaks seen in the CVs. Likewise, the

electrochemical behavior observed in the CVs of Mn-citrate (Figure 5.2c) is very similar to that of citrate solutions (Figure 5.2d) indicating that manganese reduction occurs at potentials more negative than –1.5 V. In order to determine which species are being oxidized and reduced, a clear understanding of which species are present in solution and in what amount at a specific pH value is important.

The composition of the species present in solution is dependent on solution pH since pH controls the level of deprotonation of the coordinating ligand and the amount of hydroxide available to form metal oxides and hydroxides. These metal oxides and hydroxides may become significant as the pH approaches 7, as is the case with gluconic acid, discussed later. Even though citric acid is a biologically important molecule no literature was found where the binding constants Sb(III)-citrate were reported. In particular, there is no clear settlement on which Sb(III)-citrate complexes actually formed. The equilibrium constants of Mn(II)-citrate were reported, but the speciation diagram is not constructed here [12]. The pH equilibria for citric acid are well known.

Citric acid dissociates when dissolved in aqueous solution and exists in equilibrium with many different citrate species. For ease of discussion the fully, singly, doubly, and triply deprotonated species of citrate are written as H_3Cit, H_2Cit^-, $HCit^{2-}$, and Cit^{3-}, respectively. The relevant chemical equilibria and equilibrium constants for citrate in aqueous solution are shown in Eqs. 5.1-5. 3 [7].

$$\frac{[H_2Cit]^-[H^+]}{[H_3Cit]} = 7.4 \times 10^{-4} \qquad [5.1]$$

$$\frac{[HCit]^{2-}[H^+]}{[H_2Cit]^-} = 1.7 \times 10^{-5} \qquad [5.2]$$

$$\frac{[Cit]^{3-}[H^+]}{[HCit]^{2-}} = 4.0 \times 10^{-7} \qquad [5.3]$$

Small equilibrium constants for the various forms of citrate indicate the reactant is favored in the individual equilibrium equations. In order to deprotonate the citrate species, a change in pH is required to shift the equilibria. The equation for total citrate content in solution at a specific pH value is given by Eq 5.4.

$$[Cit_{Total}] = [H_3Cit] + [H_2Cit]^- + [HCit]^{2-} + [Cit]^{3-} \qquad [5.4]$$

Using the relevant citric acid equilibria (Eqs. 5.1-5.3) along with the equation for total citrate concentration (Eq. 5.4) the equilibrium diagram can be calculated by simultaneously solving the four equations. Then the diagram that shows the fraction of citrate species formed at a specific pH can be formed (Figure 5.3). As noted above, citric acid is a triprotic acid. Thus, the pH of the final solution controls the amount of deprotonation, which ultimately affects the metal binding and electrochemistry. Looking at Figure 5.3, it can be seen how the speciation of citric acid changes drastically as the pH is increased from pH 0 to pH 9. The pH of interest ranges from 4-7 to avoid the early onset of hydrogen evolution and preclude metal oxide precipitation. At pH values 1 and 2, the main species in solution is the fully protonated citrate. At pH 3, one half of the citrate is singly deprotonated. At pH 4 the major species in solution becomes H_2Cit^- with small but equal amounts of H_3Cit and $HCit^{2-}$. Increasing the pH from 4 to 5 makes the prevailing species in solution nearly equal amounts of H_2Cit^- and $HCit^{2-}$, with slightly more of the doubly deprotonated species present. At pH 6 the dominant species is $HCit^{2-}$ with lesser amounts of H_2Cit^- and H_3Cit. By pH 7, the citrate speciation is dominated by the fully deprotonated Cit^{3-}.

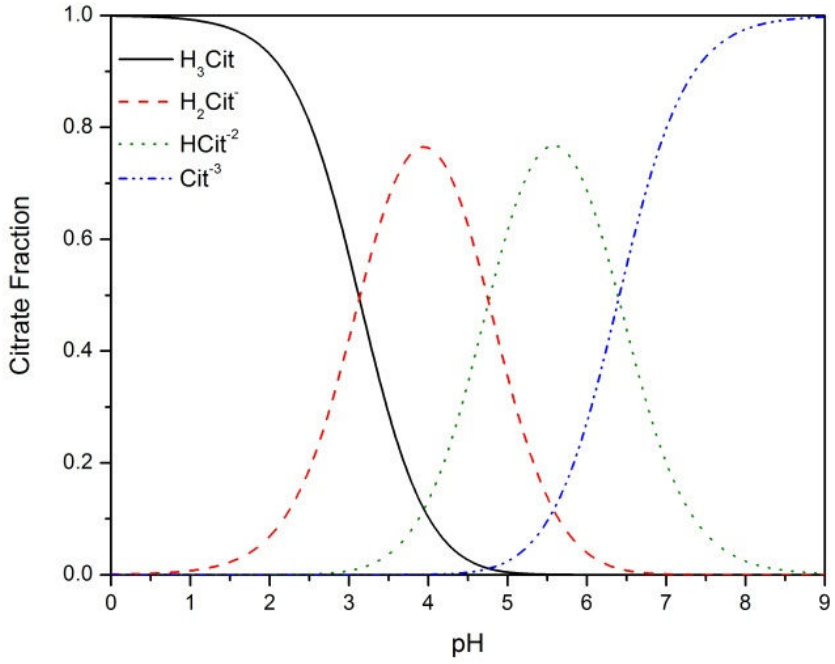

Figure 5.3. Calculated speciation diagram of 200 mM citric acid at 25 °C. The contribution of each citrate species is shown.

The speciation diagrams can be used to help understand which species are being oxidized and reduced in the CVs. The CVs of citric acid solutions at pH 5 and 7 (Figure 5.2d) reflect the speciation diagram. The reduction peak in the CV of the pH 5 solution is due to $HCit^{2-}$ and $HCit^{2-}$. A reduction peak is observed at a similar potential in the CV of the pH 7 solution that could be due to $HCit^{2-}$ or Cit^{3-}, but the intensity of the peak is decreased as expected based on the speciation diagram. The other species in solution, mainly H_2Cit^- with $HCit^{2-}$ and Cit^{3-} at pH 5 and 7, respectively, reduce at a similar potential or at a more negative potential where the peaks would be masked by the increase in current due to hydrogen evolution.

In summary, the electrochemistry of Sb-citrate Mn-citrate, and a mixture of Sb and Mn-citrate was examined using cyclic voltammetry. It was shown that the

electrochemistry of the Mn-citrate solution closely matches the behavior of citrate only in aqueous solution. Also it was shown that Mn-citrate reduces at potentials more negative than –1.50 V, beyond the onset of hydrogen evolution. Examination of CVs show that the electrochemical behavior of the mixture of antimony, manganese, and citrate is dominated by the reduction of antimony citrate, based on the number and position of cathodic and anodic peaks and the fact that manganese is not electrochemically active when present in citrate solutions by itself.

5.4.2 Variation in electrochemistry in antimony-manganese-EDTA solutions

In order to shift the reduction potential of manganese to less negative potentials or bring the reduction potentials of Sb and Mn closer together, a new ligand, EDTA, was evaluated as a coordinating ligand. Unlike citrate which has a -3 charge when fully deprotonated, EDTA has a –6 charge, although in the pH range of interest the maximum charge would be –5. Also, the metal-ligand binding constants will differ between citrate and EDTA, allowing changes in the reduction potential of Sb-EDTA, Mn-EDTA, or both complexes. The sodium salt of EDTA is readily soluble in water and easily solubilizes the metal precursors making it an attractive ligand choice to aid in the electrodeposition of Mn-Sb films.

EDTA is not typically used in deposition solutions with antimony or manganese. However, it has been used to improve the film quality, cyclic capabilities, and specific capacity of Sn-Co-C anode materials. [13] To determine the efficacy of EDTA as a coordinating ligand, solutions of varying pH were examined using cyclic voltammetry to study the effect of pH on the antimony and manganese deposition potentials. The first

deposition solutions studied contained 200 mM EDTA, 25 mM $Sb(CH_3COO)_3$, and 25 mM $Mn(CH_3COO)_2$. Next, solutions containing 200 mM EDTA, and 200 mM EDTA with 25 mM $Sb(CH_3COO)_3$ or $Mn(CH_3COO)_2$ were considered as shown in Figure 5.4.

Examination of the CVs of the solution containing Sb^{3+}, Mn^{2+}, and EDTA at pH 4 and 6 scanning in the negative direction from an initial potential of 0.0 V shows a small cathodic peak at –0.90 V followed by the onset of hydrogen evolution at –1.20 V.
In the CV of the pH 6 solution, an additional reduction peak at –1.40 V is observed. After the polarity is switched, one anodic peak is seen at 0.0 V at pH 4. The anodic peak is shifted in the negative direction to –0.20 V at pH 6.

In solutions containing Sb^{3+} and EDTA, the CVs of solution at pH 4 and 6 are different. The CV of the pH 4 solution shows two cathodic peaks at –0.75 V and –1.0 V followed by an anodic peak at –0.13 V upon switching the polarity. At pH 6, the reduction peak at –0.75 V nearly completely disappears, followed by a second reduction peak at –0.90 V. Due to the increased pH, the electrochemical window was widened such that hydrogen evolution did not interfere with electrochemical measurements. Comparing the CVs of the Sb^{3+}, Mn^{2+}, and EDTA mixture (Figure 5.4a) to the CVs of 200 mM EDTA and 25 mM $Sb(CH_3COO)_3$ (Figure 5.4b), reduction peaks are shifted to less negative potentials with the addition of Mn^{2+} to the solution containing Sb-EDTA. No additional anodic peaks were observed and the position of the peaks is similar to the Sb^{3+}, Mn^{2+}, EDTA mixture (Figure 5.4a). Similarly, comparing the CVs of the mixture of EDTA and Mn^{2+} (Figure 5.4c) to CVs of EDTA (Figure 5.4d) shows the reduction and oxidation peaks observed in Figure 5.4c are similar to those in the CVs of EDTA only.

Examination of the CV of the solution at pH 4 containing Mn^{2+} and EDTA scanning in the negative direction from 0.0 V shows the onset of hydrogen evolution at –0.50 V.

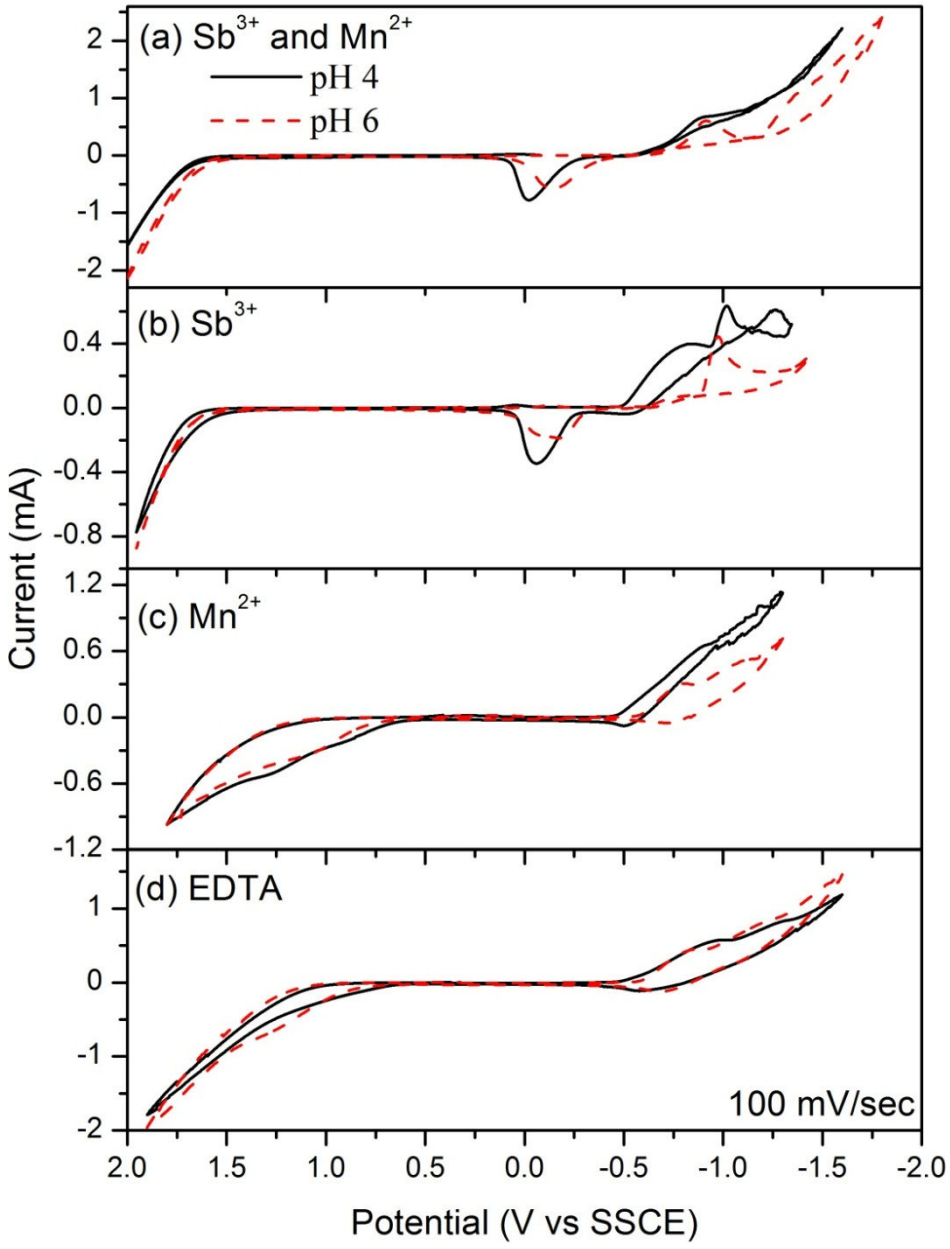

Figure 5.4. Cyclic voltammograms of solutions containing (a) 200 mM EDTA, 25 mM $Sb(CH_3COO)_3$ and 25 mM $Mn(CH_3COO)_2$, (b) 200 mM EDTA with 25 mM $Sb(CH_3COO)_3$, (c) 200 mM EDTA with 25 mM $Mn(CH_3COO)_2$, and (d) 200 mM EDTA. The reference electrode was SSCE, the working electrode was Pt, and the scan rate was 100 mV/sec.

Reduction of Mn(II)-EDTA species must occur at a more negative potential than –0.50 V. At pH 6, two cathodic peaks are observed at –0.80 V and –1.15 V, partially masked by hydrogen evolution. Upon switching the polarity a broad anodic peak is observed at +1.20 V at pH 4 and 6, probably due to an EDTA species adsorbed on the electrode surface. Similar behavior is observed in directly comparing the CVs of Mn^{2+} and EDTA (Figure 5.4c) with CVs of only an EDTA solution (Figure 5.4d). CVs of EDTA at pH 4 and 6 scanning in the negative direction from 0.0 V reveal two cathodic peaks at –0.90 V and –1.25 V. Reversing the polarity shows there are no anodic peaks. The similarities in the number and position of cathodic peaks in CVs of EDTA only and Mn-EDTA solutions support the idea that manganese is not electrochemically active in the potential range of +1.8 V to –1.25 V. The electrochemistry of each solution is determined by the species present in solution. The speciation of the ligand and metal-ligand complexes in solution is determined by the solution pH. The speciation for EDTA is well known and the binding constants of Mn(II)-EDTA and Sb(III)-EDTA were reported in the literature [14, 15]. The speciation for EDTA will be discussed first, followed by antimony and manganese.

The reported equilibria for EDTA are given in Eqs. 5.5-5.10 where H_4Y represents EDTA free acid, and H_3Y^-, H_2Y^{2-}, HY^{3-}, and Y^{4-} represents the third, fourth, fifth, and sixth deprotonated form of EDTA, respectively [7].

$$\frac{[H^+][H_5Y^+]}{[H_6Y^{2+}]} = 1.00 \times 10^0 \qquad [5.5]$$

$$\frac{[H^+][H_4Y]}{[H_5Y^+]} = 3.54 \times 10^{-1} \qquad [5.6]$$

$$\frac{[H^+][H_3Y^-]}{[H_4Y]} = 1.02 \times 10^{-2} \qquad [5.7]$$

$$\frac{[H^+][H_2Y^{2-}]}{[H_3Y^-]} = 2.14 \times 10^{-3} \quad [5.8]$$

$$\frac{[H^+][HY^{3-}]}{[H_2Y^{2-}]} = 6.92 \times 10^{-7} \quad [5.9]$$

$$\frac{[H^+][Y^{4-}]}{[HY^{3-}]} = 5.50 \times 10^{-11} \quad [5.10]$$

The stability constants for the first two carboxylic acid groups are typically ignored since their pK_a values are 0.0 and 1.5, respectively. However, at low pH they contribute significantly to the speciation of EDTA in aqueous solution. Small equilibrium constants indicate that the protonated species is preferred unless an increase in pH occurs. The equation for the total EDTA concentration present in solution is given by Eq. 5.11.

$$[EDTA_{Total}] = [H_4Y] + [H_3Y^-] + [H_2Y^{2-}] + [HY^{3-}] + [Y^{4-}] + [H_5Y^+] + [H_6Y^{2+}] \quad [5.11]$$

Using Eqs. 5.5-5.10 in conjunction with Eq. 5.11, the speciation diagram for EDTA can be calculated. The total EDTA concentration, $[EDTA_{Total}]$, is the sum of the concentrations of each EDTA species present at a specific pH value. These six equations, solved simultaneously, allow for the speciation diagram, which shows the fraction of each EDTA species present at a specific pH, to be constructed as shown in Figure 5.5. From the speciation diagram, solutions containing EDTA at low pH contain H_6Y^{2+}, H_5Y^+, H_4Y, H_3Y^-, and H_2Y^{2-}. At pH 3, the dominant specie becomes H_3Y^- and H_2Y^{2-}. Also at pH 3, the amount of H_4Y approaches zero. H_3Y^- begins forming at pH 1 and reaches its maximum fraction of 0.5 at approximately pH 2.5. H_2Y^{2-} begins forming around pH 1

and increases until pH 4.5 where the maximum fraction of 0.98 is reached before declining in concentration until pH 8, where it approaches zero.

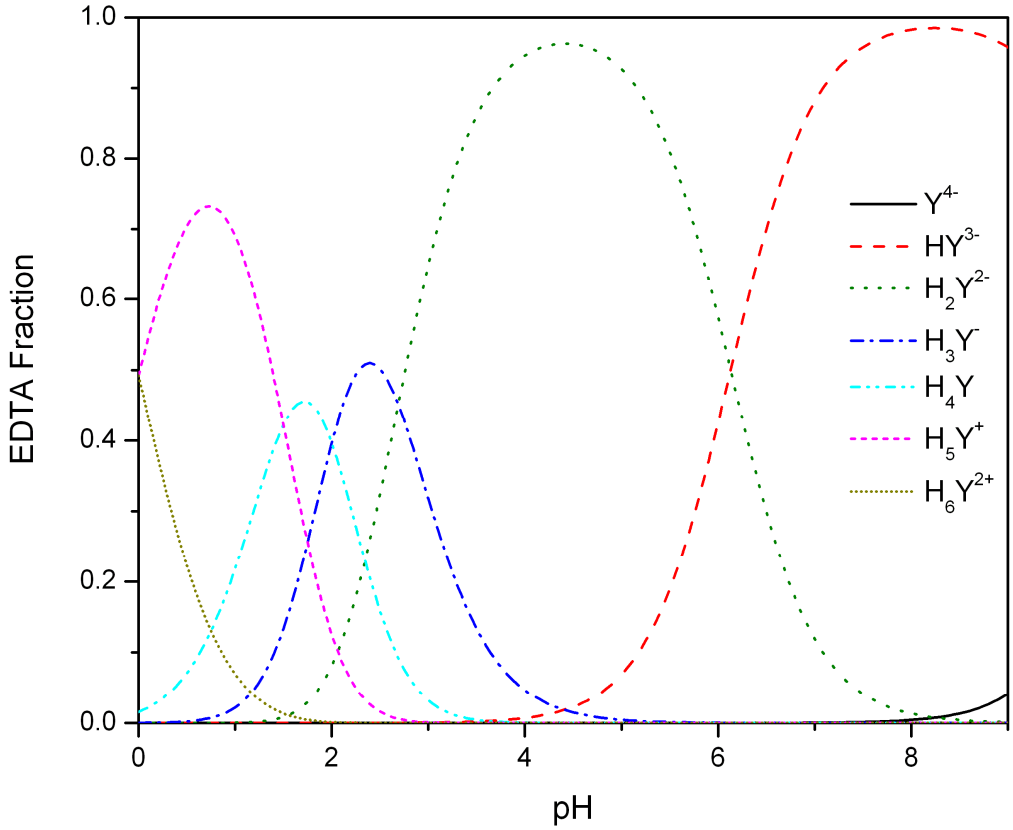

Figure 5.5. Calculated speciation diagram of 200 mM EDTA at 25 °C. The contribution of each form of EDTA in aqueous solution depending on pH.

The H_2Y^{2-} is the dominant EDTA species between pH 2.5 and 6, though there are other EDTA species present. At pH values greater than 6, the HY^{3-} species dominates.

The speciation diagram for EDTA can be used to explain the electrochemical observations seen in the CVs of EDTA solutions. At pH 4, the dominant species by far is H_2Y^-, and at pH 6 the dominant species is an equal mixture of H_2Y^- and HY^{3-}. Despite the differences in speciation, the CVs of EDTA solutions at pH 4 and 6 look remarkably similar. The cathodic peak at –0.70 V is due to the reduction of carboxylic acid functional

groups to a primary alcohol. At all pH values carboxylic acid groups are being reduced so only small changes in the position of the reduction peak is expected based on pH.

Besides speciation of the EDTA, the metal-EDTA complexes are important as well in understanding the electrochemistry. Both antimony and manganese bind with EDTA. The reported equilibira and corresponding K for Sb(III)-EDTA complexes are given in Eqs. 5.12-5.15 [16].

$$\frac{[SbY]^-}{[Sb^{3+}][Y^{4-}]} = 5.9 \times 10^{26} \quad [5.12]$$

$$\frac{[SbYH]}{[SbY]^-[H^+]} = 1.0 \times 10^{28} \quad [5.13]$$

$$\frac{[SbY(OH)_2]^{3-}}{[SbY(OH)^{2-}][OH^-]} = 5.8 \times 10^{20} \quad [5.14]$$

$$\frac{[Sb(OH)_3]^0[HY^{3-}]}{[SbY^-][OH^-]} = 4.7 \times 10^{12} \quad [5.15]$$

The very large Sb-EDTA binding constants indicate that EDTA very strongly binds antimony in aqueous solution. According to the CVs, antimony is still electrochemically reduced and oxidized at potential values less negative than the onset of hydrogen evolution, despite being bound so strongly to the ligand. Besides binding antimony, EDTA binds manganese. The reported equilibria and corresponding K for Mn(II)-EDTA are given in Eqs. 5.16-5.18. [17]

$$\frac{[MnY]^{2-}}{[Mn^{2+}][Y^{4-}]} = 1.1\ x\ 10^{14} \quad [5.16]$$

$$\frac{[MnHY]^-}{[Mn^{2+}][HY^{3-}]} = 7.9\ x\ 10^6 \quad [5.17]$$

$$\frac{[MnHY]^-}{[MnY^{2-}][H^+]} = 1.3 \qquad [5.18]$$

The equilibrium constants for the formation of $[MnY]^{2-}$ and $[MnHY]^-$ are large, indicating manganese is strongly bound to EDTA. Due to lack of reduction and oxidation in the CVs, the reduction of Mn-EDTA complexes is precluded by the onset of hydrogen evolution.

Though the speciation diagrams for Sb-EDTA and Mn-EDTA are not calculated here, the reported equilibrium constants show that the formation of both Sb-EDTA and Mn-EDTA complexes are favorable. Although Sb-EDTA complexes are reduced at potentials less negative than the onset of hydrogen evolution, the reduction of Mn-EDTA does not occur at an accessible potential where hydrogen evolution does not interfere. It has been shown that EDTA binds both Sb and Mn which allows for aqueous solutions containing both Sb and Mn-EDTA complexes.

5.4.3 Variation in electrochemistry in antimony-manganese-gluconate solutions

Since CVs showed that Mn-EDTA complexes do not reduce at a potential less negative than the onset of hydrogen evolution, gluconic acid was considered as a coordinating ligand. Unlike citrate and EDTA, gluconic acid is a monoprotic organic acid with a -1 charge when fully deprotonated. The sodium salt of gluconic acid is easily soluble in water and solubilizes the metal precursors. Gluconic acid is an attractive candidate for a coordinating ligand in the deposition of Mn-Sb films.

Gluconate solutions of varying pH were examined using cyclic voltammetry to study the effect of pH on the antimony and manganese deposition potentials.

The first deposition solutions studied contained gluconic acid, Sb^{3+}, and Mn^{2+}. The CVs are shown in Figure 5.6a.

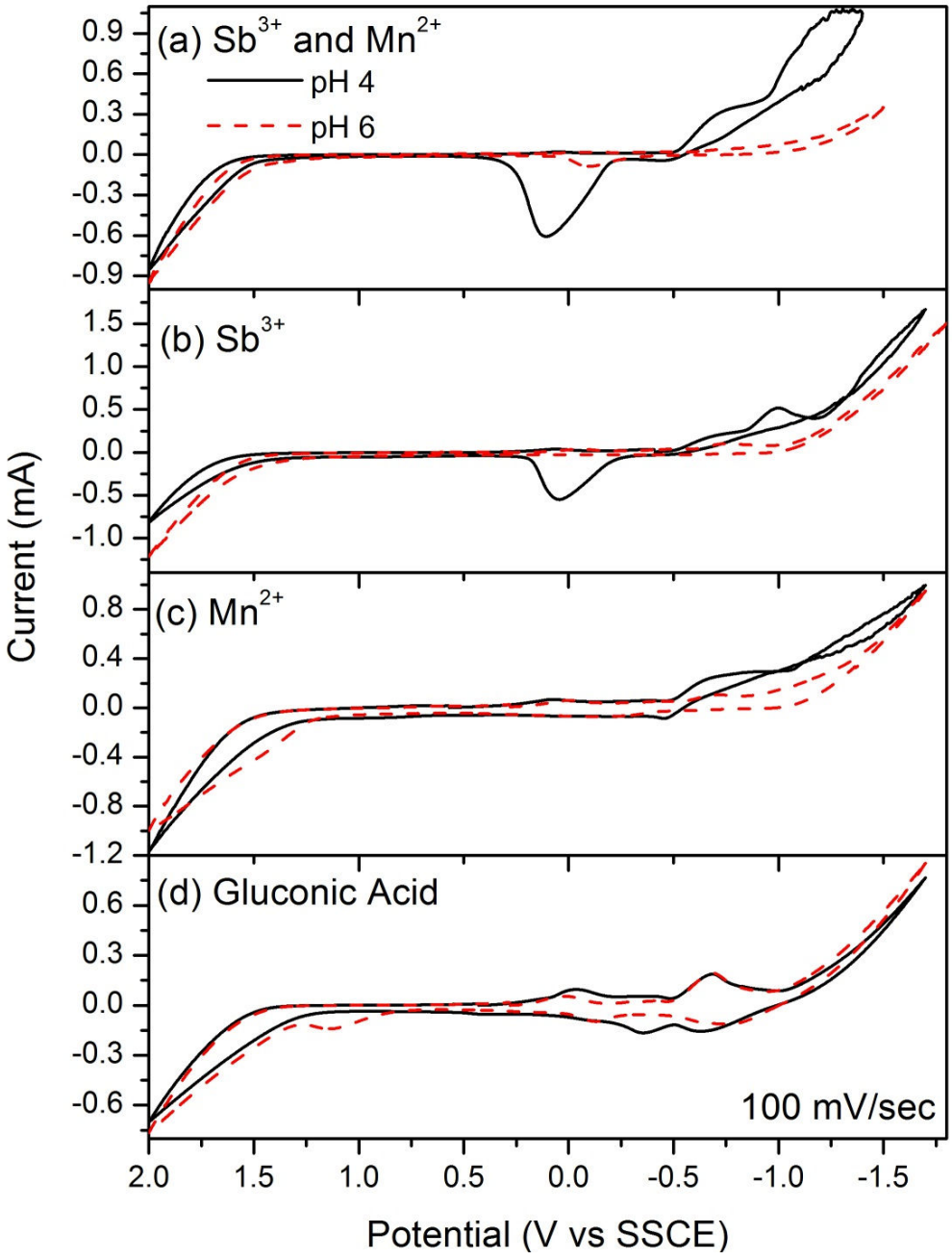

Figure 5.6. Cyclic voltammograms of solutions containing (a) 200 mM gluconic acid, 25 mM $Sb(CH_3COO)_3$ and 25 mM $Mn(CH_3COO)_2$, (b) 200 mM gluconic acid with 25 mM $Sb(CH_3COO)_3$, (c) 200 mM gluconic acid with 25 mM $Mn(CH_3COO)_2$, and (d) 200 mM gluconic acid. The reference electrode was SSCE, the working electrode was Pt, and the scan rate was 100 mV/sec.

Examination of the CVs of the solution containing Sb^{3+}, Mn^{2+}, and gluconic acid at pH 4 and scanning in the negative direction from an initial potential of 0.0 V results in two cathodic peaks at –0.70 V and –1.15 V. The onset of hydrogen evolution begins at –0.5 V. In solution at pH 6, a small reduction peak is observed at –0.70 V. Hydrogen evolution is delayed until –1.40 V. After the polarity is switched a single anodic peak is seen at 0.1 V at pH 4. At pH 6, a small anodic peak is present at –0.1 V. At pH 6, the reduction of Sb-EDTA is precluded by the onset of hydrogen evolution. Now that the electrochemistry of the mixture of Sb^{3+}, Mn^{2+}, and gluconic acid has been considered, the electrochemistry of the constituents will be examined.

In solution containing Sb^{3+} with gluconic acid at pH 4, shown in Figure 5.6b, first scanning in the negative direction from 0.0 V shows the presence of three cathodic peaks located at –0.65 V, –1.00 V, and –1.50 V with hydrogen evolution beginning at –0.5 V. Upon switching polarity, one anodic peak is present at +0.05 V. In the same way that the redox chemistry changed in the Sb^{3+}, Mn^{2+}, and gluconic acid mixture from pH 4 to pH 6, as the pH is increased from 4 to 6 in the Sb-gluconate solution, the redox chemistry changes significantly. Scanning in the negative direction from 0.0 V, there is only a single cathodic peak present at –0.70 V in the solution containing Sb^{3+} with gluconic acid at pH 6 (Figure 5.6b). No anodic peaks are present. This indicates that the reduction of a Sb(III)-gluconate species occurs at a more negative potential than –1.50 V when the pH is adjusted to 6. Additionally, the cathodic peak at approximately –0.70 V may be due to the reduction of gluconic acid since the position resembles the position of the reduction of gluconic acid (Figure 5.6d). Variations in the electrochemistry of Sb-gluconate were discussed in detail in Chapter 4.5.

In solution containing Mn^{2+} with gluconic acid at pH 4 and 6, a single cathodic peak is observed at –0.7 V with hydrogen evolution beginning at –0.50 V (Figure 5.6c). Upon switching the polarity, no anodic peaks are observed. The CVs of Mn^{2+} with gluconic acid (Figure 5.6c) strongly resemble the CVs obtained from solution containing gluconic acid only (Figure 5.6d). The absence of an anodic stripping peak indicates the reduction of Mn-gluconate to Mn metal does not occur in the scanned potential range 2.0 V to –1.7 V. Potentials more negative than the onset of hydrogen evolution are required to reduce Mn-gluconate complexes. At pH 4 and 6, solutions containing gluconic acid have two cathodic peaks at 0.0 V and –0.7 V with the onset of hydrogen evolution starting at –1.0 V (Figure 5.6d). The cathodic peak at –0.7 V is present in both the gluconic acid and the Mn-gluconate CVs, showing the cathodic peak in the Mn-gluconate solution is due to the reduction of gluconate. Upon switching polarity, two anodic peaks are seen at –0.7 and –0.3 V. At pH 6 an additional anodic peak is seen at +1.20 V, probably due to a gluconic acid species adsorbed to the electrode surface. The CVs of gluconic acid at pH 4 and 6 have similar features and are explained by the speciation diagram shown in Figure 4.4. At both pH 4 and 6 the main species in solution is the anion GH_4^-, so the observed electrochemistry at both pH values is similar.

In this section, it was shown that the coordinating ligand chosen to solubilize the metal precursors and bring the reduction potentials of the two metals closer together is a critical component of the system. Citrate, EDTA, and gluconate have different charges when fully deprotonated and each ligand has a different speciation profile depending on the solution pH. The solution pH and corresponding speciation profile of the ligand determines the speciation of the antimony and manganese in solution, thus controlling the

electrochemistry. Additionally, the metal-ligand equilibrium constant describing how tightly the metal is coordinated to the ligand is different for each ligand and each ligand species. CVs of solutions containing Sb^{3+}, Mn^{2+}, and a ligand show redox chemistry is occurring. CVs of solutions containing antimony and a ligand show that antimony is electrochemically active. On the other hand, CVs of solution containing manganese and a ligand show that manganese is not electrochemically active within the aqueous electrochemical window. To determine what redox chemistry is occurring in the Sb^{3+}, Mn^{2+}, and ligand mixtures and if the electrochemical reduction of Sb-ligand and Mn-ligand complexes results in the formation of MnSb or Mn_2Sb, films were deposited from solutions containing citrate, EDTA, or gluconate with antimony and manganese.

5.5 Constant potential depositions and film composition

Earlier in this chapter it was shown that solution chemistry, specifically speciation and pH, play an important role in the observed electrochemistry of aqueous solutions containing antimony, manganese, and ligand. The CVs of solution containing Sb^{3+}, Mn^{2+}, and coordinating ligand show that redox chemistry is occurring at potentials less negative than the onset of hydrogen evolution. To determine if this redox chemistry was the result of Sb-ligand and Mn-ligand reduction to form MnSb or Mn_2Sb, thin films were electrodeposited directly on a conducting copper substrate at a single potential. Besides the differences in electrochemical behavior observed in the CVs caused by the choice of coordinating ligand, both solution pH and bath temperature were considered in thin film electrodeposition.

5.5.1 Experimental details

Films were electrodeposited from aqueous solution containing 200 mM ligand, 25 mM $Sb(CH_3COO)_3$ (99.99% metals basis, Aldrich), and 25 mM $Mn(CH_3COO)_2$ (98%, Aldrich), where the ligand is citric acid (sodium salt, 99.5+%, Aldrich), EDTA (disodium salt, ~99%, Aldrich), or gluconic acid (sodium salt, 99% minimum, Aldrich). The deposition solutions were prepared by adding the ligand to 18 MΩ·cm Millipore water and stirring until the ligand was completely dissolved. Then $Sb(CH_3COO)_3$ was added. Upon complete dissolution, the $Mn(CH_3COO)_2$ was added. The pH was subsequently adjusted to the range of 4-7 by the addition of ammonium hydroxide (NH_4OH, Aldrich, ACS reagent grade). The resulting solutions were clear and colorless.

Depositions were conducted in a three-electrode cell using a CHInstruments 660 workstation for thin films or a Gamry Ref3000 for wires. Platinum mesh was used as the counter electrode and a saturated sodium calomel electrode (SSCE) was used as the reference. Copper foil or evaporated copper substrates with an approximate surface area of 1 cm^2 were used as the working electrode. The evaporated copper substrates were prepared by evaporation on clean glass slides using a Denton Vacuum evaporator with a Maxtek MDC-260 deposition controller. Glass slides were cleaned with dilute sulfuric acid then rinsed with water and methanol. Then, 5 nm of chromium was deposited to act as an adhesion layer for the copper, which was then deposited to a thickness of 200-250 nm. In order to mask off the desired surface area, clear nail polish was used to insulate the back and sides of the substrates. The depositions were at a constant potential for 10 minutes and the bath temperature was either 25 °C or 60 °C. After the deposition was

complete, the films were rinsed with copious amounts of distilled water and allowed to air dry.

The films were characterized using SEM-EDS and XRD. The SEM-EDS data were obtained using a JEOL JSM-6500F equipped with energy EDS from Thermo Electron. An accelerating voltage of 15 kV was used in all cases. The XRD powder patterns were obtained using a Scintag X-2 advanced diffraction X-ray cabinet system using Cu Kα radiation and Peltier Detector.

5.5.2 Room temperature depositions, pH, and film composition

Based on CVs of citrate solutions containing 200 mM citric acid, 25 mM $Sb(CH_3COO)_3$, and 25 mM $Mn(CH_3COO)_2$, at pH 6 and 7 the reduction potential used for film deposition was –1.30 V. XRD was used to identify crystalline components of deposited films. A representative XRD pattern for films deposited from citrate solutions at room temperature and a single potential is shown in Figure 5.7. Peaks corresponding to copper from the substrate at 43, 50, and 74 °2θ are responsible for the highest peak intensity. Additional peaks in the XRD pattern correspond to rhombohedral antimony metal. The antimony peaks at 40 and 51.5 °2θ are more defined in the XRD pattern as the pH is increased from pH 6 to 7. No manganese was observed in the XRD pattern at pH 6 or pH 7. Upon examination of the films using SEM-EDS it was determined that <1% of the film deposited from solution at pH 6 was amorphous manganese.

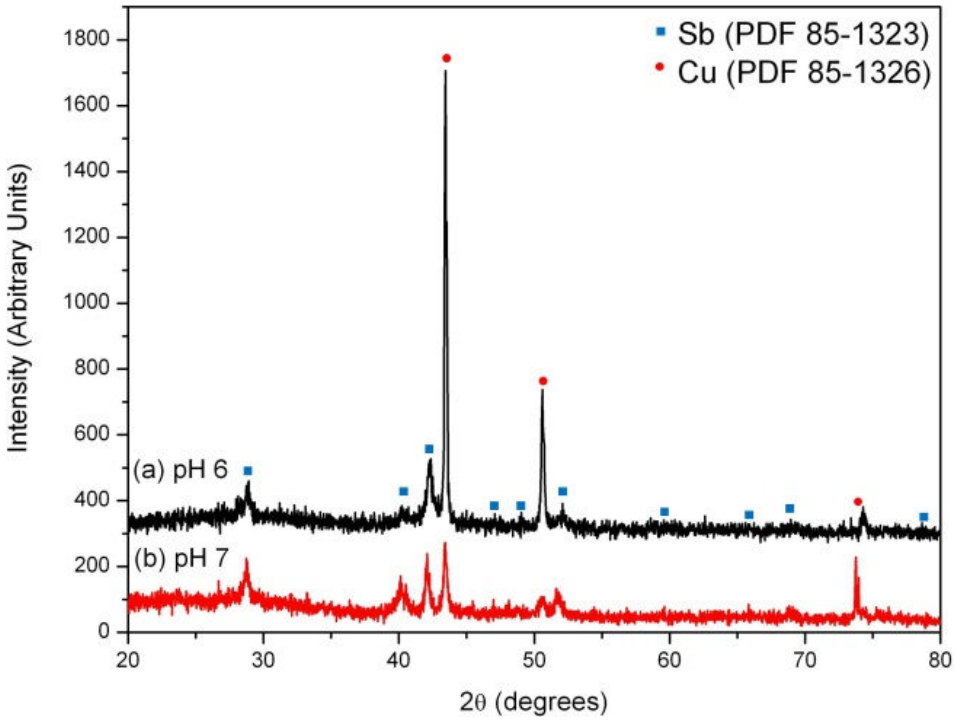

Figure 5.7. XRD patterns of Sb and Mn films deposited for 10 minutes from solution containing Sb^{3+}, Mn^{2+}, and citric acid using evaporated copper substrates at (a) pH 6 and (b) pH 7.

Since the position of the anodic peak in the CVs corresponded to the oxidation of antimony (Figure 5.2a, b) and Mn-citrate was not electrochemically active at this potential, the low abundance of manganese is not unexpected. In order to deposit manganese, a more negative potential must be applied to the deposition bath to reduce Mn-citrate complexes, a ligand that brings the reduction potentials of the two metals closer together, or the use of a ligand that binds manganese less strongly is necessary.

XRD patterns for films deposited from EDTA deposition baths display similar features to the XRD patterns for films deposited from citric acid. Figure 5.8 is a representative XRD pattern for films deposited from EDTA baths at pH 4-6 at a deposition potential of –1.40 V vs. SSCE. Peaks corresponding to copper from the substrate at 43, 50, and 74 °2θ are again responsible for the highest intensity. However,

unlike the films deposited from citrate solutions on evaporated copper, these substrates are copper foil. The large reflection at 50 °2θ indicates the copper foil is cut in the (200) direction. Additional peaks in the XRD patterns at all pH values correspond to rhombohedral antimony. No manganese was observed in the XRD pattern at any pH value. Examination of the films using SEM-EDS indicates that amorphous manganese is not present in the deposited film.

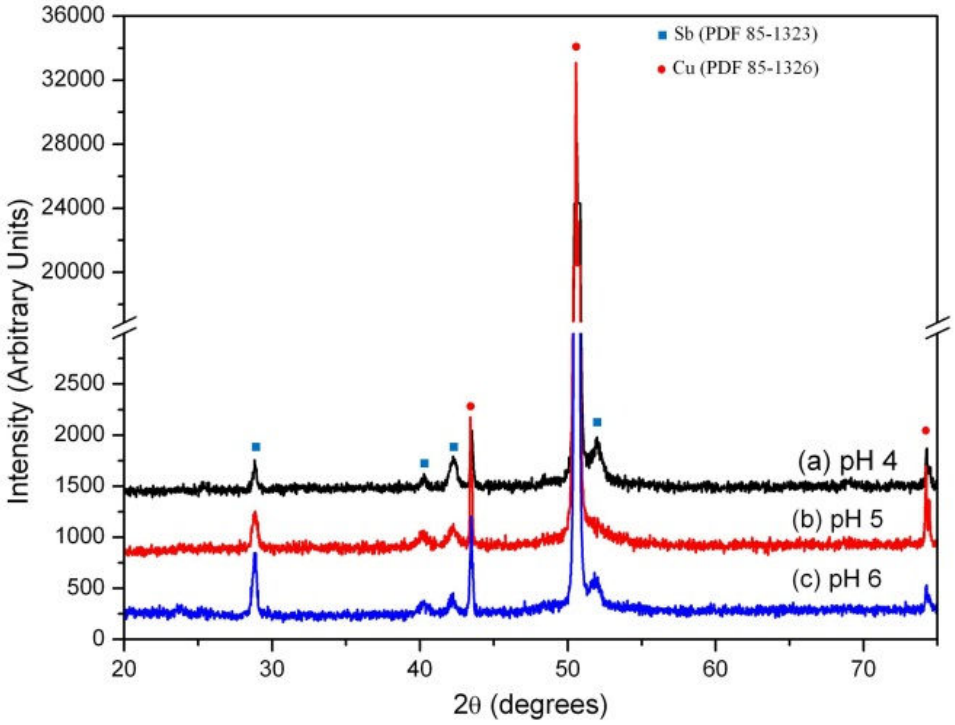

Figure 5.8. XRD patterns of Sb and Mn films deposited for 10 minutes from solution containing Sb^{3+}, Mn^{2+}, and EDTA using copper foil substrates at (a) pH 4, (b) pH 5, and (c) pH 6.

The lack of manganese indicates that Mn-EDTA complexes are not reduced at the deposition potential –1.40 V as a result of the strong Mn-EDTA binding indicated in the large equilibrium constants. However, since the binding constants for Sb-EDTA complexes are larger than for Mn-EDTA complexes, it was thought that the deposition of

antimony would be depressed. According to Eq. 4.1, the reduction potential of a metal-ligand complex is determined not only by the binding constant, but the reduction potential of the unbound metal and the number of electrons transferred. Therefore, it follows that a more negative deposition potential is required to reduce Mn-EDTA complexes than Sb-EDTA complexes due to the reduction potential of Sb^{3+} and Mn^{2+} in aqueous solution. The electrochemical window of the deposition solution is limited by the onset of hydrogen evolution (Figure 5.4) and does not allow access to more negative potentials, which are required for Mn-EDTA reduction. Therefore, to preclude hydrogen evolution, films were deposited from gluconate solutions at pH 6, due to the delayed onset of hydrogen evolution (Figure 5.6a).

The XRD pattern for a representative film deposited at –1.20 V and at room temperature from a gluconate bath at pH 5 (Figure 5.9) shares similar features with films deposited from citrate and EDTA baths. The evaporated copper substrate is responsible for reflections at 43 and 50 °2θ. Additionally, the other peaks are indexed to rhombohedral antimony. No significant reflections are unreferenced. New features are observed in XRD patterns for films deposited from gluconate solutions at pH 4 (Figure 5.6a). Besides peaks present from the copper substrate and antimony, reflections at 31.8, 35.0, 43.6, and 45.2 °2θ among others, are due to the presence of tetragonal Cu_2Sb.

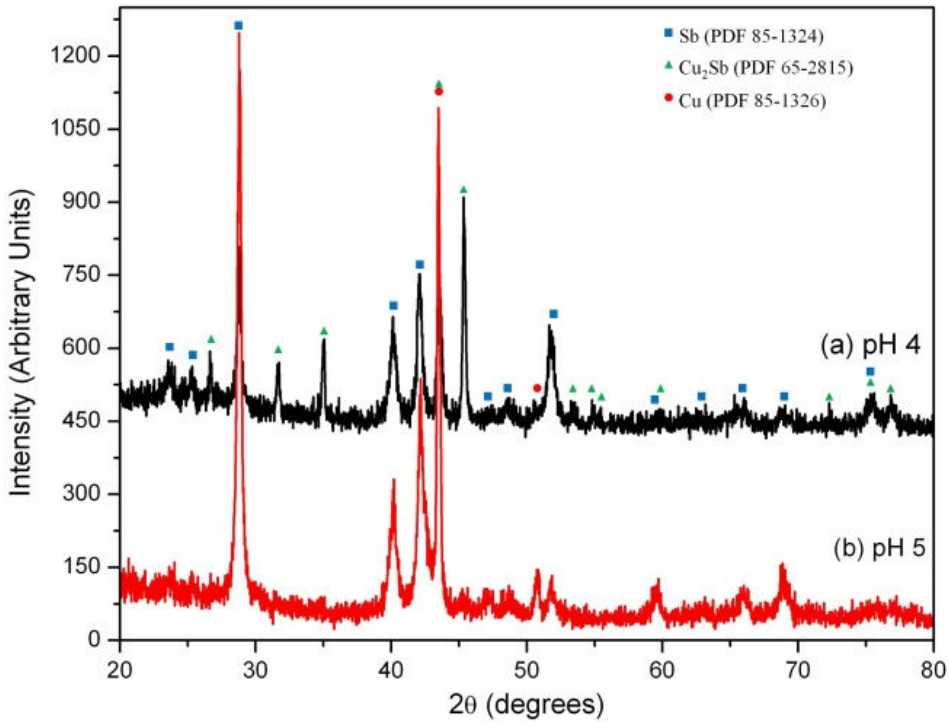

Figure 5.9. XRD patterns of Sb and Cu_2Sb films deposited for 10 minutes from solution containing Sb^{3+}, Mn^{2+}, and gluconic acid using evaporated copper substrates at (a) pH 4 and (b) pH 5.

During the deposition process, copper from the substrate migrated via diffusion into the antimony thin film forming Cu_2Sb. Unfortunately, the identifying reflections for Mn metal and tetragonal Cu_2Sb are very similar. It was originally thought that depositing films from gluconate solution at pH 4 yielded crystalline thin films of a Mn-Sb alloy. Therefore, much of the subsequent research was focused on gluconate deposition baths.

Summarizing the results of the room temperature depositions using citric acid, EDTA, and gluconic acid: films deposited from citrate solutions at pH 5 contain <1% manganese (determined by EDS) whereas films deposited from EDTA and gluconate solutions contained no manganese as determined by XRD. XRD characterization of all films deposited from citrate and EDTA solutions shows the presence of rhombohedral

antimony and cubic copper (from the substrate). Films deposited from gluconate baths also showed the presence of rhombohedral antimony and cubic copper, but the solution at pH 4 also showed the presence of Cu_2Sb according to XRD. Since Mn and Cu_2Sb XRD peaks overlap significantly, it was thought that an alloy of Mn-Sb was formed. Later SEM-EDS characterization revealed it was Cu_2Sb and not manganese. However, it was thought that Mn and Sb were deposited at room temperature from gluconate baths adjusted to pH 4 at a single potential. To promote solid state diffusion of Mn into Sb and form the desired MnSb or Mn_2Sb, the temperature of the bath was raised to 60°C.

5.5.3 High temperature depositions, pH, and film composition

Films deposited from solution containing 200 mM citrate, EDTA, or gluconic acid with 25 mM $Sb(CH_3COO)_3$, and 25 mM $Mn(CH_3COO)_2$ were examined for changes in composition and crystallinity due to increasing the bath temperature from 25 °C to 60 °C. Figure 5.10 is a representative XRD pattern for a film deposited from a citrate bath at 60 °C and an applied potential of –1.20 V for all pH values. Examining the XRD powder pattern shows the presence of three crystalline film components including rhombohedral antimony, cubic copper, and tetragonal Cu_2Sb. The copper peaks are a result from the substrate. As the pH is increased from 5 to 7 (Figure 5.10a-c) the intensity of the Sb reflections increases and the peaks become narrower. For example, the peak at approximately 28 °2θ sharpens and grows in intensity. The increased temperature may contribute to sintering of the film and increasing of the grain size, which would account for the narrower, more intense peaks as a function of pH. Inspecting the film using SEM-EDS reveals no manganese is present, only copper and antimony.

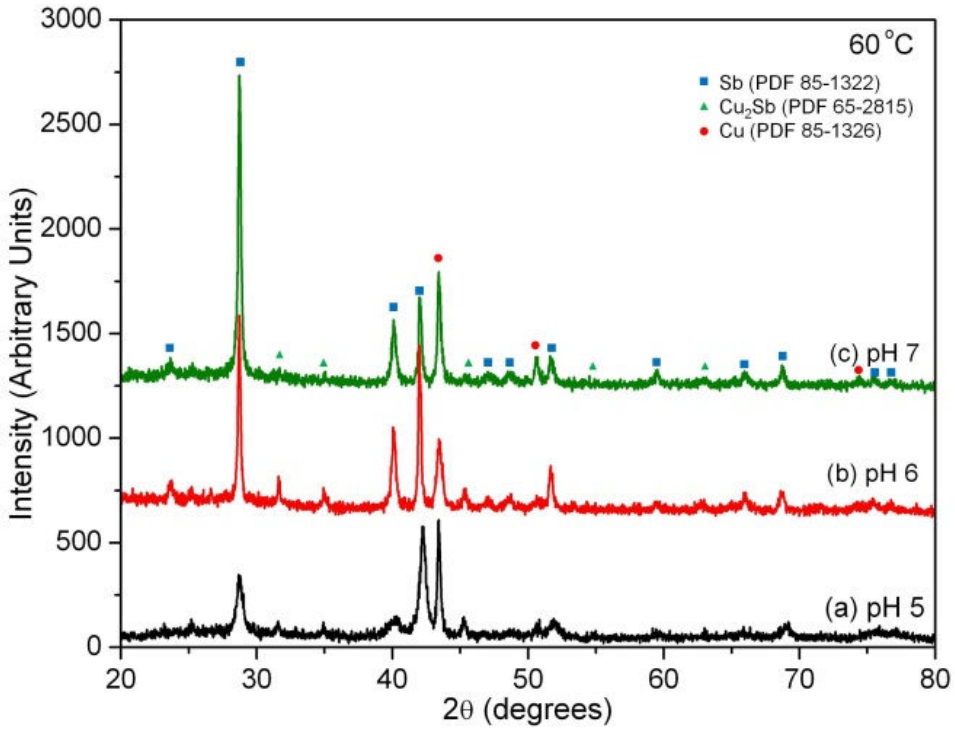

Figure 5.10. XRD patterns of Sb and Mn films deposited at 60 °C for 10 minutes from solution containing Sb^{3+}, Mn^{2+}, and citric acid using evaporated copper substrates at (a) pH 5, (b) pH 6, and (c) pH 7.

The increased temperature did not allow for the deposition of Mn and Sb. Instead, the increased temperature promoted the formation of Cu_2Sb via diffusion of copper from the substrate into the Sb film. Since citrate baths did not yield MnSb using a higher bath temperature, EDTA baths with elevated temperatures were used for film deposition to observe differences in film composition due to choice of coordinating ligands.

Films deposited from EDTA bath solutions at 60 °C between pH 4 and 6 at a deposition potential of –1.00 V showed similar results as shown in Figure 5.11.

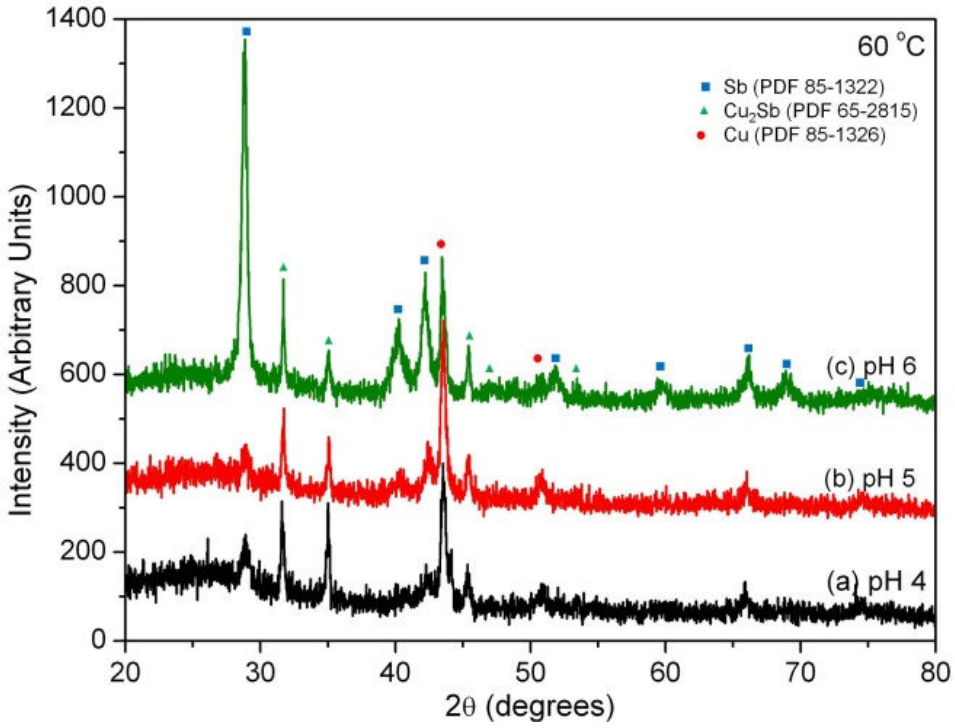

Figure 5.11. XRD patterns of Sb and Mn films deposited at 60 °C for 10 minutes from solution containing Sb^{3+}, Mn^{2+}, and EDTA using evaporated copper substrates at (a) pH 4, (b) pH 5, and (c) pH 6. The squares indicate Sb, triangles Cu_2Sb, and the circles Cu.

The XRD powder pattern reveals the presence of three crystalline film components including rhombohedral antimony, cubic copper, and tetragonal Cu_2Sb. As the pH is increased from 4 to 6, the intensity of the antimony reflections increases, probably due to sintering of the film during the deposition process, leading to larger grain sizes. This would also account for the narrowing of the peaks with increasing pH. Additionally, the large growth of the reflection at approximately 28 ° 2θ indicates Sb has a preferred orientation. The room temperature deposition was performed on a copper foil substrate and the high temperature deposition was performed on evaporated copper substrates. This accounts for the differences in the copper peaks in the room-temperature and high-temperature powder patterns shown in Figures 5.8 and 5.11, respectively. The intensity

and peak width for peaks corresponding to Cu_2Sb is similar from pH 4-7. Examining the film using SEM-EDS data indicate no manganese is present, verifying the presence of Cu_2Sb, not Mn. Raising the temperature of the deposition bath did not promote the deposition and diffusion of Mn into Sb, instead the diffusion of Cu into Sb was promoted and Cu_2Sb was formed.

Since neither citrate nor EDTA baths at elevated temperature yielded MnSb, high temperature gluconate baths were considered to observe differences in film composition as the number of coordination sites is decreased from 6 to 1 and the onset of hydrogen evolution is shifted to approximately –1.50 V at room temperature. Films deposited at 60 °C from baths containing gluconic acid were characterized using XRD and SEM-EDS. Representative XRD patterns of films deposited from gluconate solutions at pH 5-7 at an applied potential of –1.20 V are shown in Figure 5.12. Examining the XRD powder pattern shows the presence of three crystalline film components including rhombohedral antimony, cubic copper, and tetragonal Cu_2Sb. Films deposited at pH 6 and 7 have similar powder patterns that show the presence of crystalline antimony and copper. Films deposited at pH 5 also contain crystalline copper and antimony, but also contain crystalline Cu_2Sb. Unlike films deposited from high temperature citrate and EDTA baths, Cu_2Sb only appears in the powder pattern at pH 5, not at pH 6 or 7. The reason for this is unknown. If the deposition substrate at pH 5 was left in the deposition solution at 60 °C several minutes after the deposition was complete, the diffusion of copper into antimony and subsequent sintering of the film could have occurred. SEM-EDS analysis detected manganese in films deposited from baths at pH 5, but at <1% of the film composition. On average films deposited from solution at pH 6, where no manganese appeared in the

powder pattern, contained manganese with a Sb:Mn ratio of 0.93 ± 0.05 and the film-to-film composition varied by approximately 12%. Films deposited at pH 7 indicated an even greater manganese content with a Sb:Mn ratio of approximately 1:3. A large difference in film-to-film composition was also observed, similar to the variability exhibited at pH 6. These differences may be due to impurities in the manganese precursor. It has been shown that the deposition of Mn is sensitive to the presence of impurities, particularly Ni, Fe, Cu, and Co [3, 6]. The presence of these impurities suppresses the deposition of Mn.

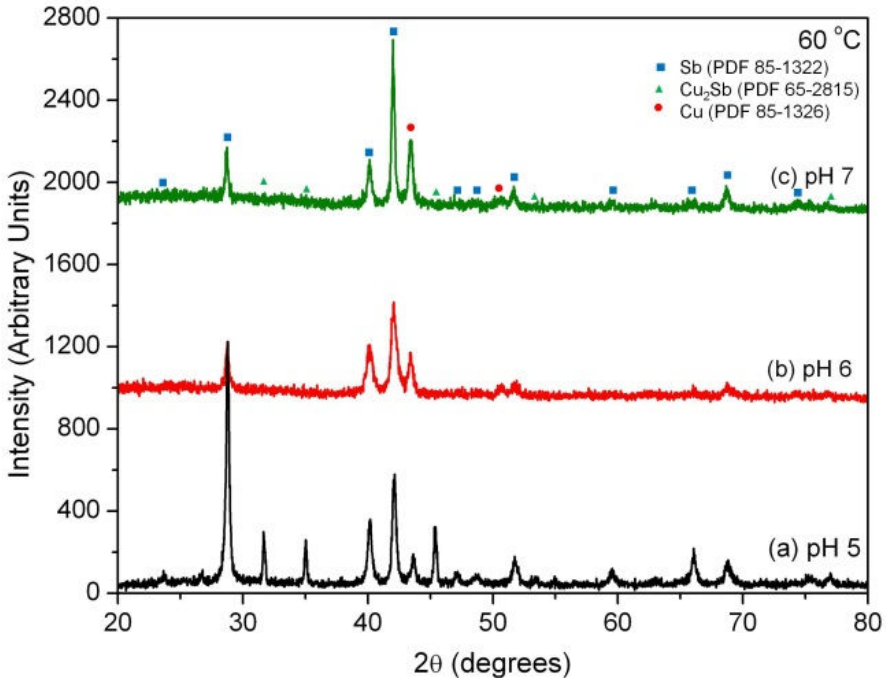

Figure 5.12. XRD patterns of Sb and Mn films deposited at 60 °C for 10 minutes from solution containing Sb^{3+}, Mn^{2+}, and gluconic acid using evaporated copper substrates at (a) pH 5, (b) pH 6, and (c) pH 7.

EDS was used to further determine the composition of the as-deposited films and the mapping was used to identify the distribution of each metal on the electrode. Figure

5.13 shows EDS elemental mapping that suggests a layer of antimony is deposited followed by the deposition of manganese. Figure 5.13a shows the morphology of the as-deposited film from aqueous solution containing 200 mM gluconic acid, 25 mM $Sb(CH_3COO)_3$, and 20 mM $Mn(CH_3COO)_2$ at 60 °C. The morphology is constant over the surface of the film. EDS elemental mapping of manganese (Figure 5.13c) shows the manganese deposits evenly over the film while elemental mapping shows antimony is mainly confined between the large island growths (Figure 5.13b).

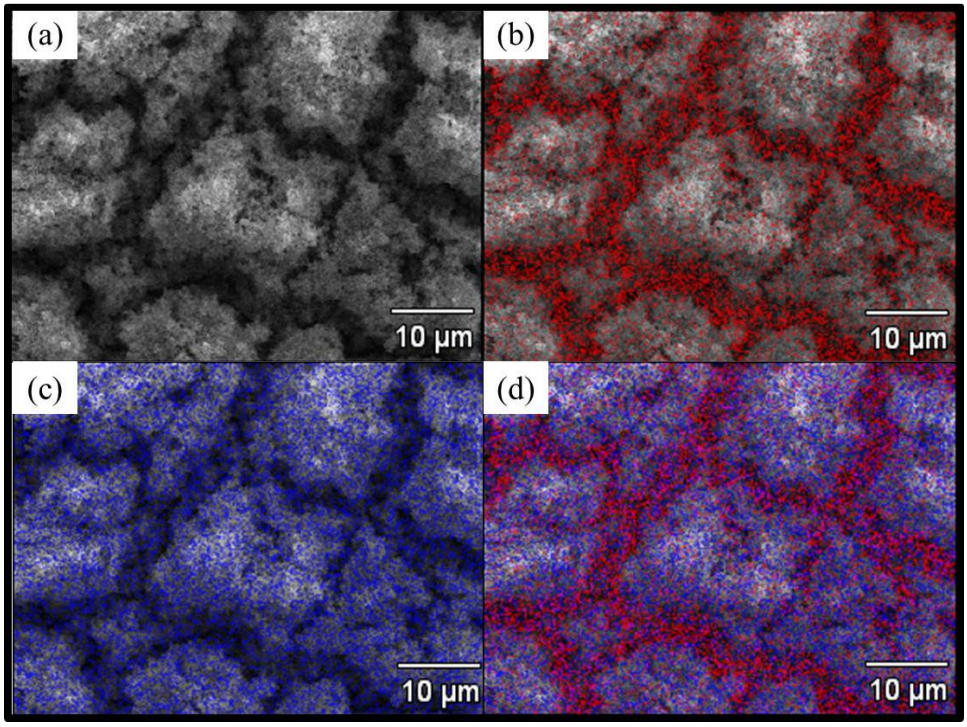

Figure 5.13. EDS elemental mapping of films deposited from solution containing Sb^{3+}, Mn^{2+}, and gluconic acid using evaporated copper substrates where (a) shows the morphology of the film, (b) antimony mapping overlay, (c) manganese mapping overlay, and (d) combination of both antimony and manganese mapping overlay.

Despite antimony mainly growing between the islands, no difference in morphology is observed when comparing the island growth to the growth between the islands,

suggesting the observed morphology is due to manganese. This idea is supported by the EDS mapping, which shows Mn evenly covering the film. Combining the elemental maps of antimony and manganese (Figure 5.13d) shows where antimony and manganese deposit relative to each other. The purple areas are where both metals deposit. The remaining gray portions of the film are identified as oxygen or carbon using EDS, probably in the form of antimony and manganese oxide and advantageous carbon.

Based on the EDS mapping, the deposition mechanism was thought to be the deposition of antimony metal, which allowed the induced underpotential deposition of manganese on top of the already-deposited antimony. Arguably, depletion of the antimony-gluconate complex at the electrode surface was required before the deposition of manganese could proceed. Thus, the mechanism of antimony-gluconate and manganese-gluconate deposition was further explored considering observations recorded during the depositions and a literature examination.

While depositing films from solution containing gluconic acid, the counter electrode, a Pt mesh flag, and the solution around it turned a bright red/pink color throughout the course of the deposition, indicating the presence of Mn(IV). A literature search revealed that in Mn(II)-gluconate systems, the manganese complex is easily oxidized according to Table 5.1. In gluconate solutions with manganese in the +2 oxidation state, Mn(II)-gluconate complexes are easily oxidized at potentials less negative than –1.20 V vs. SSCE, the potential where the depositions took place. According to Table 5.1, the deposition of Mn should not occur by reduction of Mn(II) to Mn^0 at an applied potential of –1.20 V where the depositions took place. This is evidence that the mechanism of Mn-Sb alloy deposition proceeds by the deposition and depletion

of antimony first, which then allows for the induced underpotential deposition of manganese.

Table 5.1 Characteristic redox of the Mn-gluconate complexes in aqueous solution. Adapted from Bodini *et al* . [18].

	Ox. State	ΔOx. State	vs. SSCE
Oxidation	Mn(II)	II→IV	–0.29 V
	Mn(II)	II→III	–0.54 V
	Mn(III)	III→IV	–0.27 V
Reduction	Mn(II)	II→0	–1.75 V
	Mn(III)	III→0	–1.73 V
	Mn(III)	III→II	–0.53 V
	Mn(III)	III→II	–1.04 V
	Mn(IV)	IV→III	–0.27 V
	Mn(IV)	IV→II	–1.10 V
	Mn(IV)	IV→0	–1.73 V

While Sb-gluconate and some Mn-gluconate complexes are being reduced at the working electrode surface, Mn(II)-gluconate complexes are simultaneously oxidized to Mn(III) and Mn(IV) at the Pt gauze counter electrode according to Table 5.1. As those complexes diffuse toward the working electrode, they are then reduced to Mn(II), Mn(III), or Mn^0 at the electrode surface. Not only does the deposition of manganese depend on the underpotential deposition allowed by the initial deposition of antimony, but it depends on the diffusion of manganese species to the surface of the working electrode. There is a direct competition for the reduction and oxidation of Mn-gluconate complexes, which decreases the amount of Mn(II)-gluconate at the electrode available for deposition. Increasing the Mn precursor concentration from 25 mM to 50 mM to promote Mn deposition does not improve the Mn incorporation into the film. Instead, increasing the

Mn precursor concentration results in a decrease in the amount of Mn in the deposited film to <0.5%.

To summarize high temperature film deposition, depositions from baths raised to 60°C containing citrate or EDTA did not promote the deposition of Mn. Instead, XRD and SEM-EDS revealed the presence of antimony, copper (from the substrate), and copper antimonide. Baths raised to 60°C containing gluconic acid allowed the deposition of Sb and Mn at pH 6 and 7, though Mn was not crystalline. Films containing Mn-Sb alloys were electrodeposited at a single potential from baths containing gluconic acid adjusted to pH 6 or 7. The ratio of Sb:Mn was 0.93 ± 0.05, at pH 6 and 0.294 ± 0.003 at pH 7 with approximately 12% difference in composition from film to film. Due to the oxidation of the Mn-gluconate complexes, the use of a different ligand may allow the deposition potential to be shifted to a point inside the electrochemical window so that Mn may be deposited at potentials less negative than the onset of hydrogen evolution. However, the deposition of Mn-Sb can proceed when deposited from gluconate baths. It is predicted that the deposition of antimony first allows the underpotential deposition of manganese. To test this hypothesis, wires were deposited from solution containing 200 mM gluconic acid, 25 mM $Sb(CH_3COO)_3$, and 20 mM $Mn(CH_3COO)_2$ at 60 °C into an anodic alumina template at a constant potential where the pores restrict the concentration of metal-ligand complexes available at the electrode surface. If the Sb is depleted inside the pores, the deposition of Mn may be promoted before the Sb-gluconate can be replenished. Examining the wires for growth of Sb only at the current collector followed by the presence of Mn may indicate this prediction is valid.

5.6 Electrodeposition of Mn-Sb wires in an anodic alumina template

Even though the ultimate goal for these anode materials is to electrodeposit nanowires for use in a 3D battery architecture to improve rate capabilities, decrease Li diffusion distances, and decrease initial capacity loss; the purpose of this experiment was to probe the mechanism of Mn-Sb deposition at a single potential with restricted metal-gluconate complexes available for deposition in the pores. In electrodeposition, alumina templates are commonly used to deposit nanowires because the templates can be easily and completely removed after the deposition is complete. Nanowires remain after the dissolution of the template. The diameter and length of the wires can be easily controlled by pore size of the template and deposition time. Though an electrodeposition procedure for MnSb, and Mn_2Sb has not been fully optimized, alloy films of Mn-Sb have been deposited. Mn-Sb alloy wires were deposited in an anodic alumina template from gluconate baths at 60 °C at an applied potential of –1.20 V vs. SSCE. Unlike thin films, these wires can be annealed to promote the formation of MnSb and Cu_2Sb contamination will be minimized, only occurring in the small area where the wire contacts the copper current collector.

5.6.1 Experimental details

Depositions were conducted in a three-electrode cell using a Gamry Ref3000. Platinum mesh was used as the counter electrode and a SSCE was used as the reference. For wire depositions, the template substrates were prepared by deposition of 5 nm chromium and 200 nm of copper on the back of an anodic alumina template using a Denton Vacuum evaporator with a Maxtek MDC-260 deposition controller. The

templates are Whatman® Anopore membranes with a pore size of 200 nm and a thickness of 60 μm. Electical contact was made by attaching a copper wire to the substrate template using colloidal graphite paste. To ensure deposition was only occurring in the pores, the back of the substrate, copper wire, and sides were insulated with clear nail polish. The wires were deposited for 1800 seconds after the open circuit potential for the template substrate was constant, indicating sufficient wetting, with an applied potential of –1.20 V vs. SSCE.

The films were characterized using SEM-EDS using a JEOL JSM-6500F equipped with energy EDS from Thermo Electron. An accelerating voltage of 15 kV was used in all cases. The copper wire and insulating layer of nail polish was removed from the back of the template substrate for SEM imaging. Additionally, to determine pore filling and observe cross-sectional images of wire growth in the template, the substrate was carefully broken in half. The standard deviation of the Sb: Mn ratio was calculated from data of multiple samples at a given set of deposition conditions. The 95% confidence interval was then calculated using the student t-test.

5.6.2 Deposition of Mn-Sb alloy wires in a template

The reason for depositing nanowire arrays of MnSb is twofold: (i) to probe the deposition mechanism of Mn-Sb films and (ii) the expectation that a higher surface area anode will exhibit better battery performance characteristics than that of the bulk material. The deposition mechanism of Mn-Sb can be probed by purposefully choosing the porous template as a substrate which restricts the metal-ligand concentration in the pores due to diffusion. Because the deposition was not pulsed, there was no dead time

where bulk metal-ligand complexes could diffuse into the pores. Instead, it was predicted that the antimony-gluconate complex would reduce first followed by depletion of the complex in the pore which allows the subsequent under-potential reduction of manganese-gluconate still available in the pore after the antimony-gluconate depletion.

The same conditions used to deposit Mn-Sb alloy thin film on copper was used for the nanowire array deposition. Before the deposition took place, the template was wetted until the open circuit potential was constant. Figure 5.14 is an SEM image showing the formation of wires in the template. Figure 5.14a is a top down view of the pores showing that some of the pores are filled.

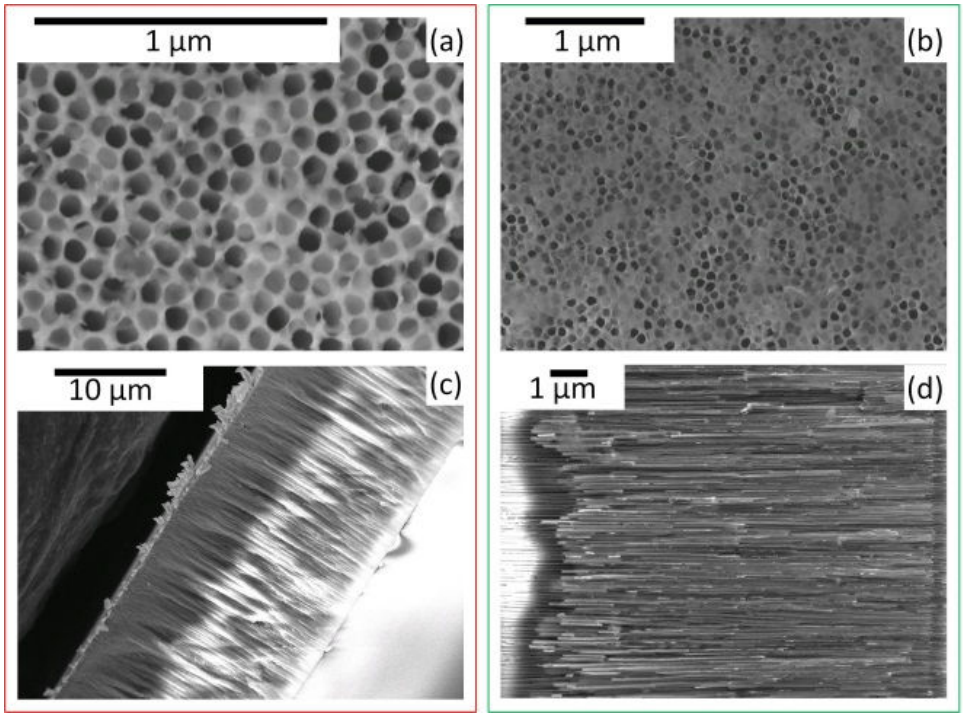

Figure 5.14. SEM image of Mn-Sb alloy wires electrodeposited in an alumina template where (a) shows some pores are filled, (b) shows fraction of pores that are filled, (c) side view shows the pores are approximately 40% filled, and (d) shows a side view of the wires. The deposition was 800 seconds long at a potential of –1.20 V vs. SSCE.

Another top down view from farther away shows that some pores are filled and a thin film has developed on top of parts of the template (Figure 5.14b). The length of the wires can be controlled by the deposition time. An 800 second deposition filled approximately 40% of the pore length (Figure 5.14c) while an 1800 second deposition filled about 60% of the pore length (not shown). Lastly, a side view of the wires shown in Figure 5.14d highlights the observation that the wires are not perfectly cylindrical.

SEM images showed that the pores were filled with some material during the deposition process. EDS was then used to determine the composition of the wires and elemental mapping was used to visually identify the material distribution in the electrodeposited wires. Figure 5.15 shows a SEM image of the selected wire electrode area, map overlay of antimony, map overlay of manganese, and a map overlay of both antimony and manganese. In Figure 5.15a, the copper current collector is the white strip on the far right side of the image. The wire growth began there. On the far left side of Figure 5.15a beyond the end of the electrodeposited wires is the alumina template. The composition of the wires included both antimony and manganese. According to EDS data, the Sb:Mn ratio was found to be 4 ± 1. Based on the EDS mapping of the Mn-Sb thin films, it was predicted that when confined in a pore, antimony would deposit first followed by the induced underpotential deposition of manganese. Restricting the concentration of metal-gluconate species in the pores allowed for the deposition of antimony until it was depleted in the pore, and then the deposition of manganese occurred until the antimony could be replenished. It is unclear in the EDS mapping if a layer of antimony deposits first, but it appears that antimony is present in greater concentration at the current collector (far right of Figure 5.15b) and at the end near the opening of the

pores (left side of Figure 5.15b). This indicates that antimony is deposited preferentially in the pore near the current collector and near the end of the pore where the diffusion length for the replenishment of antimony-gluconate from the bulk is small. Also, according to EDS mapping antimony is present the entire length of the wires.

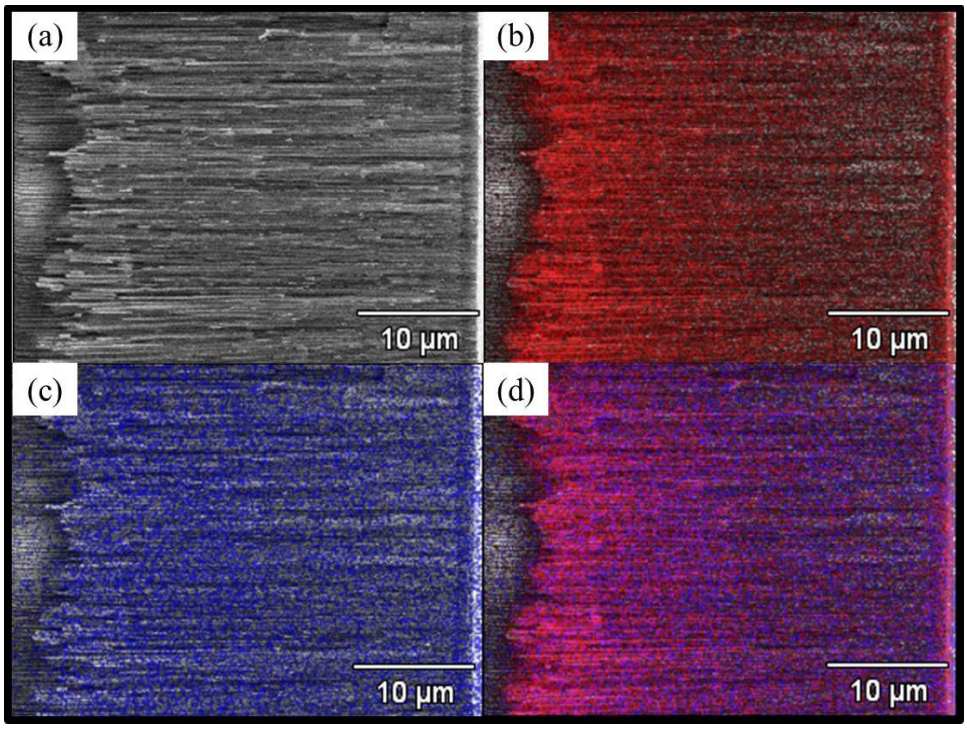

Figure 5.15. EDS elemental mapping of films deposited from solution containing Sb^{3+}, Mn^{2+}, and gluconic acid into anodic alumina templates with a copper contact where (a) displays a SEM image showing the morphology of the film, (b) antimony mapping overlay, (c) manganese mapping overlay, and (d) combination of both antimony and manganese mapping overlay.

Manganese is also present the entire length of the wires but the composition seems to be uniform along the entire length indicating a constant deposition rate (Figure 5.15c). Comparing the EDS maps of antimony and manganese at the current collector show more antimony than manganese. This shows that the idea that the deposition and depletion of the antimony-gluconate complex inside the pore is required before the deposition of

manganese can proceed may be valid. The depletion of antimony is required to *begin* the underpotential deposition of manganese. Even as antimony is replaced, the deposition of both metals can still proceed. Although the deposition of the more noble antimony is preferred over manganese it does not preclude manganese deposition. This is evidenced by the presence of both metals the entire length of the wire.

EDS analysis of Mn-Sb wires grown in alumina templates has shown that it is possible that the deposition of antimony allows for the underpotential deposition of manganese. Both manganese and antimony were present the entire length of the wire, with antimony more concentrated at the ends, and a more constant concentration of manganese over the length of the wire. With both wires and thin films, gentle heating to 60 °C during the deposition resulted in films containing a Mn-Sb alloy and did not result in the formation of MnSb or Mn_2Sb. Post deposition annealing of alloy materials has been shown to promote the formation of intermetallic compounds upon heating. Therefore, post deposition annealing of *thin films* containing Mn and Sb was attempted to determine if the formation of MnSb or Mn_2Sb was promoted upon heating.

5.7 Post deposition annealing of Mn-Sb thin films

Post deposition annealing of the as-deposited Mn-Sb alloy thin films at 300 °C was completed to promote the formation of MnSb or Mn_2Sb. The high vapor pressure of antimony required the system to be under a slight positive pressure (800 torr) during the annealing process. Additionally, a clean quartz tube was used to avoid any chemical vapor transport and deposition of impurities on the surface of the tube on the films. Figure 5.16 shows XRD patterns of as-deposited films versus annealed films deposited

from solution containing 200 mM gluconic acid, 25 mM $Sb(CH_3COO)_3$, and 25 mM $Mn(CH_3COO)_2$ at pH 5. These depositions were 10 minutes long with the bath temperature raised to 60 °C.

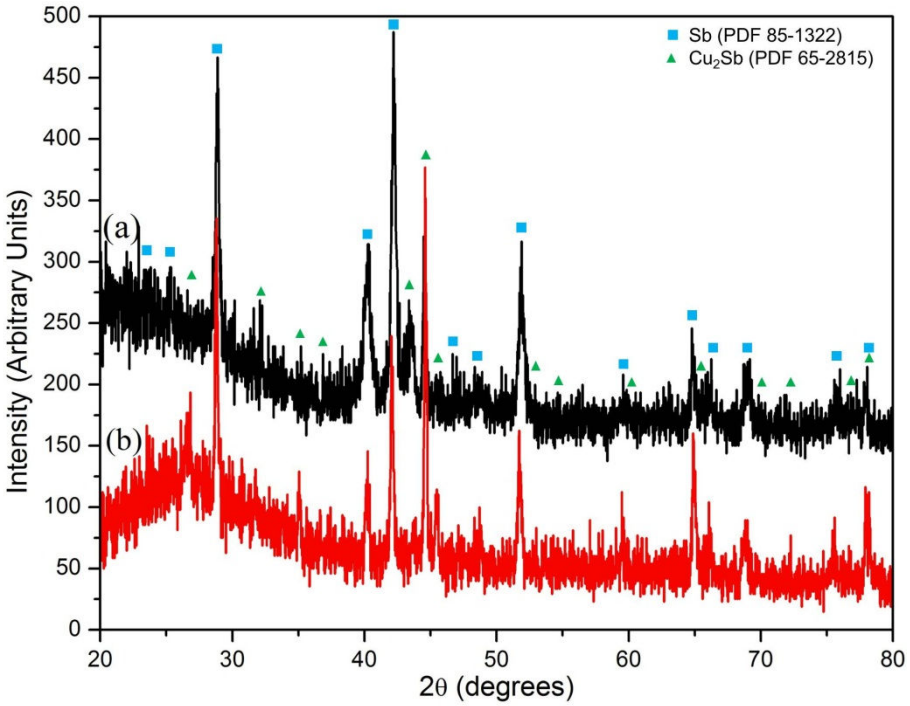

Figure 5.16. XRD patterns of films deposited at 60 °C for 10 minutes from solution containing Sb^{3+}, Mn^{2+}, and gluconic acid adjusted to pH 5 (a) as-deposited and (b) annealed at 300 °C for 12 hours at 800 torr.

The as-deposited film contained crystalline rhombohedral antimony and tetragonal Cu_2Sb as determined by XRD. No other crystalline entities were present and no peaks were unaccounted for. Surprisingly, annealing the film at 300 °C for 12 hours at 800 torr did not alter the crystalline composition. The annealed film also contained crystalline rhombohedral antimony and tetragonal Cu_2Sb. No new peaks were observed in the XRD pattern. The intensity of the peaks changed and the peaks became narrower with annealing. Although no new peaks were observed, the Cu_2Sb peaks at approximately 44 and 45 °2θ shift in intensity, with the peak at 44 °2θ decreasing in intensity and the peak

at 45 °2θ increasing in intensity after the annealing process. This indicates that Cu_2Sb crystallizes with preferred orientation. The peaks were also narrower after the annealing process probably due to increased grain size with sintering of the film. The absence of crystalline MnSb or Mn_2Sb indicates that Cu_2Sb is the thermodynamically favored phase. Therefore, post deposition annealing at these conditions is not a viable solution to promoting the formation of MnSb from films containing Mn and Sb metals.

5.8 Conclusions

Citrate, EDTA, and gluconic acid can be used to solubilize antimony and manganese precursors in aqueous solution. Additionally, reduction and oxidation behavior observed in CVs of solutions containing Sb^{3+} and Mn^{2+} can be changed by changing properties of the coordinating ligand like size, charge, and equilibrium constant. Moreover, Sb-ligand complexes were electrochemically active and Mn-ligand complexes were electrochemically inactive. The solution pH was also important in controlling the species in solution. The speciation diagrams for citrate, EDTA, and gluconic acid were calculated, demonstrating which ligand species were present in solution and available for binding at specific pH values.

Thin films were deposited at room temperature from solutions containing Sb^{3+} and Mn^{2+} with citrate, EDTA, or gluconate. Characterization using XRD and SEM-EDS showed that films deposited from citrate and gluconate solutions contained less than 1% Mn, and no manganese was detected in films deposited from EDTA baths. However, crystalline Cu_2Sb was in films deposited from gluconic acid baths at pH 5 which was

mistaken for crystalline Mn. In order to promote the diffusion of Mn into Sb, the deposition bath temperature was raised to 60 °C.

Thin films were deposited at 60 °C from solutions containing Sb^{3+} and Mn^{2+} with citrate, EDTA, or gluconate. Characterization using XRD and SEM-EDS showed that most deposited films contained crystalline Cu_2Sb. Instead of promoting the diffusion of Mn into Sb, the diffusion of Cu from the substrate into Sb was promoted. SEM-EDS data indicated that films deposited from gluconate solutions at pH 6 or pH 7 contained both Mn and Sb. It was believed the deposition occurred via underpotential deposition of Mn. Mn-Sb wires were deposited to determine if the deposition and depletion of Sb-gluconate complexes in the pore would allow for the deposition of Mn. It was found that Mn-Sb wires were formed, even with restricted metal-gluconate complexes in the pores.

In an effort to form MnSb or Mn_2Sb from thin films containing Mn and Sb, films were annealed at 300 °C at 800 torr pressure. Surprisingly, the as-deposited film and the annealed film had the same composition – Cu_2Sb. No new crystalline phases were formed during the annealing process. This result indicates the formation of Cu_2Sb is thermodynamically favored over the formation of MnSb or Mn_2Sb and annealing is not a good way to promote the formation of MnSb.

5.9 References

[1] J. Gong, I. Zana, G. Zangari, *J. Mater. Sci. Lett.* 20 (2001) 1921-1923.
[2] J. Gong, G. Zangari, *Mat. Sci. Eng. A-Struct.* 344 (2003) 268-278.
[3] J. Gong, G. Zangari, *J. Electrochem. Soc.* 149 (2002) C209-C217.
[4] J.E. Lewis, P.H. Scaife, D.A.J. Swinkels, *J. Appl. Electrochem.* 6 (1976) 453-462.
[5] R. Murti, N. Razdan, G.E. Ermolina, *Indian J. Technol.* 24 (1986) 270-274.
[6] P. Wei, O.E. Hileman, M.R. Bateni, X.H. Deng, A. Petric, *Surf. Coat. Technol.* 201 (2007) 7739-7745.
[7] A.E. Martell, R.M. Smith, *Critical stability constants*. Plenum Press, New York, 1974.
[8] S.J.S. Flora, G. Flora, G. Saxena, M. Mishra, *Cell. Mol. Biol.* 53 (2007) 26-47.
[9] D.W. Hartley, G. Smith, D.S. Sagatys, C.H.L. Kennard, *J. Chem. Soc. Dalton* (1991) 2735-2739.
[10] R. Das, S. Pani, *J. Indian Chem. Soc.* 32 (1955) 537-542.
[11] J.M. Mosby, A.L. Prieto, *J. Am. Chem. Soc.* 130 (2008) 10656-10661.
[12] P. Amico, P.G. Daniele, V. Cucinotta, E. Rizzarelli, S. Sammartano, *Inorg. Chim. Acta* 36 (1979) 1-7.
[13] D. Yu, N. Zhang, Y. Liu, W. Yu, *Heat Treat. Met.* 33 (2008) 20-22.
[14] M. Filella, P.M. May, *J. Environ. Monitor.* 7 (2005) 1226-1237.
[15] H.A. Mottola, H. Freiser, *Anal. Chem.* 40 (1968) 1266-1268.
[16] C. Macca, L. Solda, G. Favaro, P. Pastore, *Talanta* 72 (2007) 655-662.
[17] S.R. Trifunovic, Z.D. Matovic, V. Milovanovic, H. Kawaguchi, M. Yamasaki, *Transit. Metal Chem.* 25 (2000) 680-685.
[18] M.E. Bodini, L.A. Willis, T.L. Riechel, D.T. Sawyer, *Inorg. Chem.* 15 (1976) 1538-1543.

CHAPTER 6

CONCLUSIONS AND FUTURE WORK FOR THE ZNSB AND MNSB SYSTEMS

6.1 The ZnSb system

6.1.1 Single potential deposition of ZnSb thin films

The work presented in Chapter 4 covered the development of an electrochemical deposition procedure for the direct deposition of ZnSb thin films. The films were deposited from aqueous solution at a single potential and at room temperature. This material was studied for use as an anode material in a lithium-ion battery. An inexpensive synthesis method was desired to control fabrication costs for the components of a lithium-ion battery. To develop an electrochemical deposition method the relationship between speciation and the electrochemistry of solutions containing gluconate, Zn^{2+}, and Sb^{3+} was studied. The known equilibria for Zn-gluconate and Sb-gluconate were used to calculate speciation diagrams. Speciation data were used to describe cyclic voltammograms of the deposition solutions at different pH values. It was found that the reduction potential of Sb^{3+} shifted to less negative potentials as the pH was increased until the Sb was so tightly bound to the gluconate that reduction did not occur within the probed electrochemical window. The reduction potential of Zn^{2+} shifted to more negative potentials as the pH was increased due to the shift in dominance of Zn-gluconate species from $ZnGH_4^-$ to $ZnGH_4OH$. The reduction potentials of Sb and Zn were close to each other in solutions at pH 4-7. Using solutions in this pH range, the deposition parameters

were optimized so that a film containing both Sb and Zn could be reproducibly deposited on a copper substrate.

6.1.2 Optimizing the film composition

Films containing both Sb and Zn were electrochemically deposited at room temperature from aqueous solution at a single potential. This goal was reached by examining the effect of coordinating ligand, deposition potential, and deposition bath temperature on film composition. Gluconic acid was chosen as the coordinating ligand due to excellent solubility and electrochemical window. It was determined that Sb and Zn could be directly deposited at a potential of -1.54 V vs. SSCE from solution containing 200 mM gluconic acid, 25 mM $Sb(CH_3COO)_3$, and 25 mM $Zn(CH_3COO)_2$ at pH 6 or 7. Depositing films at more positive potentials resulted in Sb rich films. Also, lower pH resulted in Sb rich films. The as-deposited films were not crystalline. Instead, crystalline Sb was observed and the Sb:Zn ratio determined using EDS. Raising the temperature of the deposition bath from 25 °C to 60 °C increased the crystallinity of the Sb, but did not promote the formation of crystalline ZnSb. According to EDS, the prepared films are relatively free from impurities.

6.2 The MnSb system

The work presented in Chapter 5 covered the development of an electrochemical deposition procedure for the direct deposition of MnSb thin films. Films containing Mn and Sb were deposited from aqueous solution at a single potential and at room temperature onto a copper foil substrate. This material was studied for use as an anode

material in a lithium-ion battery. To develop an electrochemical deposition method the relationship between speciation and the electrochemistry of solutions containing gluconate, Mn^{2+}, and Sb^{3+} was studied. Coordinating ligands considered included citric acid, EDTA, and gluconic acid. The known equilibria for each ligand were used to calculate speciation diagrams. Speciation data were used to help describe cyclic voltammograms of the deposition solutions at different pH values. It was found that the electrochemistry of the deposition solution was similar to the Sb-ligand electrochemistry and Mn-ligand electrochemistry closely matched the behavior of the ligand only.

6.2.1 Single potential deposition of MnSb thin films

Depositions were performed at room temperature and at 60 °C to determine if Mn could codeposit with Sb. It was found that no Mn codeposited with Sb at room temperature. The choice of coordinating ligand did not change the film composition. XRD patterns of films deposited at room temperature and pH 4-7 from citric acid, EDTA, and gluconic acid showed the presence of crystalline antimony, but no crystalline manganese. At elevated temperatures the only films with relevant amounts of Mn and Sb were deposited from aqueous solution containing 200 mM gluconic acid, 25 mM $Sb(CH_3COO)_3$, and 25 mM $Mn(CH_3COO)_2$ at pH 6 or 7. No relevant amounts of Mn were detected via EDS in films deposited from citric acid or EDTA.

6.2.2 Optimizing the film composition

Films containing both Mn and Sb were deposited at a single potential and elevated bath temperature from solutions containing gluconic acid. This goal was reached

by examining the effect of coordinating ligand, deposition potential, and deposition bath temperature on film composition. Gluconic acid was chosen as the coordinating ligand due to the composition of as-deposited films. It was determined that Sb and Mn could be directly deposited at a potential of –1.20 V vs. SSCE from solution containing 200 mM gluconic acid, 25 mM $Sb(CH_3COO)_3$, and 25 mM $Zn(CH_3COO)_2$ at pH 6 or 7. Depositing films at more positive potentials resulted in Sb rich films. Also, lower pH resulted in Sb rich films. The as-deposited films were not crystalline. Instead, crystalline Sb was observed in the XRD patterns and the Sb:Mn ratio determined using EDS. Raising the temperature of the deposition bath from 25 °C to 60 °C increased the crystallinity of the Sb, but did not promote the formation of crystalline ZnSb. According to EDS, the prepared films are relatively free from impurities.

Wires containing Mn and Sb were also deposited at a single potential (–1.20 V vs. SSCE) from baths at elevated temperature. Both Mn and Sb were present the entire length of the wire, with antimony more concentrated at the ends, while manganese was more constant over the length of the wire. Gentle heating to 60 °C during the deposition resulted in films containing a Mn-Sb alloy and did not result in the formation of crystalline MnSb or Mn_2Sb.

6.3 Future work: ZnSb and MnSb systems

To determine the process that occurs during the growth of intermetallic and alloy films electron microscopy studies to elucidate the deposition mechanism would be useful. TEM grids can be used as the working electrode and the material directly electrodeposited then examined. This would provide compositional and morphological

evidence of the nucleation and growth process of intermetallic and alloy films. Additionally, this might provide insight on how to form crystalline ZnSb or MnSb films. Studies involving the diffusion of Zn or Mn and Sb into one another would also be useful. Low solubility of metals into Sb may be responsible for the formation of the amorphous alloy instead of the crystalline film because solid-state transformations allowing for the deposition of the crystalline film may not be able to occur without diffusion on a reasonable time scale. Knowledge gained from TEM and diffusion studies would help develop a more complete understanding of the codeposition of intermetallic materials. Better control of the deposition may be achieved in addition to aiding in the development of a procedure for the deposition of ZnSb nanostructures.

Studies investigating the details of lithiation and delithiation processes of electrodeposited intermetallic materials is necessary to improve cycle performance. The number of cycles before pulverization occurs depends on film thickness and the charge/discharge rate. Optimizing the thickness and rate will then allow for the anode performance to be evaluated. The performance of anode materials with and without a binder can also be assessed. Additionally, higher surface area can contribute to better battery performance due to decreased diffusion distances for lithium to travel and reduced structural degradation. Lastly, modifying the deposition procedure to include reproducible electrodeposition of nanoscale intermetallic ZnSb and MnSb is an important step in the development of 3D solid-state Li-ion batteries.

CHAPTER 7

SYNTHESIS OF SR-RU-O COMPOUNDS, OF WHICH SR2RUO4 IS SUPERCONDUCTING

7.1 Introduction

Fundamental superconductivity concepts were discussed in Chapter 1.3. This discussion will focus on copper and non-copper based superconductors, two popular theories of superconductivity, and current synthesis methods. Through the discussion, it will be shown that properties of superconducting materials are dependent on the synthetic route chosen, and that kinetically stable phases are not accessible through the popular high-temperature solid-state synthesis methods. Development of a low-temperature hydrothermal synthetic method for the synthesis of high-quality crystals, as is the goal of this work, will allow access to kinetically stable phases while reducing the time and energy demands required for current solid-state synthesis methods.

7.2 La_2CuO_4 and the evolution of copper based superconductors

In 1987, it was discovered that lightly doped $La_{2-x}Ba_xCuO_4$ was superconducting below 40 K [1]. The high-temperature crystal structure of La_2CuO_4 is body-centered tetragonal and is isostructural to the perovskite K_2NiF_4 [2, 3]. Each copper atom is surrounded by six oxygen atoms in a distorted octahedral. La_2CuO_4 contains alternating layers of perovskite $LaCuO_3$ and LaO [3]. The composition of the metal-oxide blocks that

separate the perovskite-type CuO_2 layers has a direct effect on the superconducting transition temperature, T_c. Specifically, there are electronic effects if metals with different charges are substituted or steric effects if metals of different sizes are substituted [4].

Since the discovery of superconductivity in copper oxide materials, an explosion of research in the area of high-temperature superconductivity resulted in the synthesis and characterization of new Cu-O compounds. Table 7.1 is a summary of just a few doped Cu-O compounds with their transition temperature and synthesis method.

Table 7.1. List of some copper oxide based superconducting materials with their synthesis method and transition temperature.

Compound	Synthesis	T_c (K)	Ref.
$\mathbf{La_2CuO_{4.032}}$	flux, O_2 treatment	37.5	[5]
$\mathbf{La_{1.85}Ba_{0.15}CuO_4}$	Solid state	38	[2]
$\mathbf{La_{1.86}Ba_{0.14}CuO_4}$	Solid state	36.9	[6]
$\mathbf{La_{1.85}Sr_{0.15}CuO_4}$	Solid state	36	[2]
$\mathbf{La_{0.925}Sr_{0.075}CuO_4}$	Unspecified	32.5	[7]
$\mathbf{YBa_2Cu_3O_x}$	PVD	92	[8]
$\mathbf{Hg_2Ba_2Ca_2Cu_3O_x}$	Solid state	130	[8]

Examination of the lightly doped lanthanum copper oxides with barium or strontium shows that the transition temperature is around 40 K. Optimal doping was found to be 5-10%. These compounds have the same basic structure of pairs of pyramids pointing in the ±c direction with an oxygen atom in each corner and a copper atom at the center of their base [9]. Comparing the lanthanum barium copper oxides and the lanthanum strontium copper oxides shows the relationship between ionic size and critical temperature.

Compounds containing barium (149 pm), which has a larger crystallographic radius than strontium (132 pm), have a higher critical transition temperature [10]. With equal amounts of doping, T_c decreases from 38 K to 36 K with a decrease in ionic radius. Not long after these layered La-Cu-O materials were discovered to be superconducting, materials with greater number of copper oxide layers were shown to have considerably higher T_c values, including yttrium-barium-copper oxide (YBCO) with T_c at 92 K [8]. More complicated layered copper oxide structures exist like $Hg_2Ba_2Ca_2Cu_3O_x$ with a T_c of 130 K [11].

Cuprate superconductors have proven to be difficult to understand theoretically and are very challenging to produce in sufficiently high quality [1, 9, 12-14]. It was thought that the copper oxide layers were the reason for the observed superconductivity. However, non-copper superconducting materials have since been discovered. Also, according to the popular Bardeen-Cooper-Schrieffer (BSC) theory, the theoretical maximum predicted value for T_c is about 40 K [15]. Contrary to this prediction, critical temperatures as high as 130 K have been reported for copper oxide superconductors, as shown above. Therefore, in order to better understand the mechanism of superconductivity in superconducting materials, researchers have turned to non-copper oxide superconducting materials.

7.3 Non-copper oxide based superconductors

The highest reported T_c for a non-copper oxide material is 39 K for MgB_2 [16]. These samples were prepared by pressing stoichiometric amounts of elemental or metal oxide powders together then annealing under pressure. The structure of MgB_2 consists of

layers of boron with layers of Mg incorporated between them [16]. The material was originally synthesized in 1953, but superconductivity in this compound was not discovered until 2001 [16, 17].

Layered rare-earth metals LnOFeAs (where Ln = La-Nd, Sm, and Gd) are now being studied following the discovery of superconductivity at 26 K in the iron based $LaO_{1-x}F_xFeAs$. The layered rare-earth material $SmO_{1-x}F_xFeAs$ has been the focus of recent attention. The material is tetragonal with a quaternary ZrCuSiAs-type structure. It has a layered structure with alternating planes of Sm and O or F and Fe with As [18]. This material is made using solid-state techniques with annealing at 1200 °C. The onset of the superconducting transition occurs at 41.3 K for $SmO_{1-x}F_xFeAs$. Replacing Sm (109.8 pm) with La (117.2 pm) forming $LaO_{1-x}F_xFeAs$ decreases the onset of superconductivity from 41.3 K to 26 K [10, 18]. The larger the lanthanide included in the compound the lower the superconductivity. This trend is opposite of the trend observed with crystallographic size of dopants in lanthanum copper oxides and shows how important it is that a theory describing the mechanism of superconductivity is established.

A particular non-copper oxide superconductor of note is Sr_2RuO_4. This material is isostructural to $La_{2-x}Ba_xCuO_4$ with the same layered perovskite structure. The strontium ruthenate crystals are typically grown using a float zone method. The crystal type is body-centered tetragonal of the K_2NiF_4 structure [19]. It has been shown using this material that the presence of copper oxide layers are not a prerequisite of superconductivity[19]. However, the low superconductivity transition temperature for Sr_2RuO_4 (0.93 K) indicates copper plays a special role. Sr_2RuO_4 is also superconducting without the incorporation of a dopant, whereas La_2CuO_4 requires a dopant like barium or

strontium before superconductivity is observed. There are important differences that account for the large discrepancy in transition temperatures between the strontium ruthenium and lanthanum copper oxides. The Cu^{2+} ($3d^9$) valence state has spin ½ while the Ru^{4+} ($4d^4$) is in the low spin state where spin is 1. Many existing theories of superconductivity rely on the spin ½ state including the resonating-valence-bond (RVB) theory of superconductivity [1]. Interestingly, in Sr_2RhO_4, which is also isostructural to Sr_2RuO_4 and $La_{2-x}Ba_xCuO_4$, the Rh^{4+} ($4d^5$) has spin ½ and the material was found to be metallic, with no evidence for superconductivity down to 50 mK [19]. Therefore, it seems that the mechanism for superconductivity is different for the Sr_2RuO_4, La_2CuO_4, and Sr_2RhO_4 cases. Unraveling the problem of how superconductivity works is an important task. Until the mechanism of superconductivity is determined, the prediction of which materials will exhibit high temperature superconductivity will be controlled by incomplete or incorrect theories of superconductivity.

7.4 Theories of superconductivity

One mechanism possibly responsible for the phenomenon of superconductivity is the RVB theory, which appears to account for most experimental observations [1]. The RVB state is a mixture of singlet pairings of the electrons on different sites in a specific way. It is only a singlet with no long range order, that can be described as a fluid in that it transports spin excitations [1, 20]. The RVB theory states that as the temperature approaches T_c, BCS type superconductivity takes over.

The BCS theory starts from the idea that electron attraction exists which overcomes the electrostatic repulsion. The origin of the attractive electron interaction is

the interaction between electrons and phonons [21, 22]. An electron moving through a crystal lattice will slightly attract nearby positive charges in the lattice. The small deformation of the lattice causes a second electron, with opposite spin, to be attracted to regions of higher positive charge density. These two electrons are said to be correlated as Cooper pairs. If the energy required to disable the electron-electron pairing is greater than the energy provided by oscillating atoms in the conductor, then the material becomes superconducting as the electron pairing is intact [21, 22]. The energy required to uncorrelate these electron pairs is highest at low temperatures, then disappears as the superconducting state is achieved. On the other hand, the superconducting state is destroyed if the energy required to break up the Cooper pairs is less than the energy of the oscillating atoms in the conductor.

Although the BCS theory does not completely describe observed characteristics of high temperature superconductivity, it does have its successes. The energy required to break the state of the Cooper pairs is adequately described as a gap, as opposed to a normal metal where any small change in energy can change the state of an electron. Also, the BCS theory correctly describes the temperature dependence of the Meissner effect and the threshold magnetic field tolerance of superconducting materials. [23, 24] The theory also describes the isotope effect, which is the observation that the critical temperature is proportional to the mass of the isotope used in the material [25, 26]. Despite these successes, there is much about superconductivity that is not understood.

The chemistry and physics that are necessary to untangle the problem of correctly describing superconductivity are still in development. In particular, quantum mechanical ideas that are used to describe how electrons correlate, each interacting with other

electrons in complex ways, are not understood. *Understanding the mechanism of superconductivity is crucial for the rational design of superconducting materials with high transition temperatures.* This might be achieved by a deeper understanding of band-structure theory which could provide a complete mathematical description of the electron-phonon coupling [27]. Besides understanding how superconductivity works to logically design new materials, a low-temperature synthesis method that produces pure, high quality crystals and does not require high vacuum conditions or high temperature is required for the development of commercial applications.

7.5 Current synthetic methods

Most superconductors are made at high temperature (> 1000 °C) and high pressure. Not only is the synthesis process highly energy intensive but it also excludes the formation of kinetically stable phases of a given material, some of which might also be superconducting. Superconducting crystals are commonly grown in three ways, from a melt, under high pressure, and in the solid state.

Crystals grown from a melt contain few defects and are ultrapure. The solid metal precursors are placed in a crucible and heated just above the melting point of the precursors. Then, a single crystal seed attached to a rod is placed at the surface of the melt and slowly withdrawn. The melt crystallizes on the seed particle as it is drawn out and cooled [28]. This method is commonly used for the production of silicon. The single crystalline seed particle needed to draw out the melt for this method is frequently made using solid state synthesis techniques. Melting of the precursors to achieve high quality crystals is not required in all synthetic methods.

Application of pressure to a solid can cause a phase transition where the density of the material increases, and frequently the coordination numbers of atoms in the solid are increased as well. These phases are exclusively thermodynamically stable. An example of this type of transformation is graphitic carbon to diamond. The required pressure for the transition is 13 GPa and the temperature 3000 °C [28]. Treating solids at high temperature without the application of pressure is referred to as solid-state reactions.

Solid-state reactions involve the transformation of two phases to another phase *via* nucleation and growth. Nucleation occurs at high temperature because the desired product and solid precursors generally have different structures, so a rearrangement of the precursors is required [28]. Once nuclei have formed, growth proceeds by diffusion of ions from the reactant to the new solid layer. Figure 7.1 uses the example of La_2CuO_4 synthesis to illustrate the formation of the desired phase *via* diffusion of reactants into the solid phase. Before the reaction begins, in this case two precursors are placed in intimate contact with one another shown in Figure 7.1a. This is often done by grinding the precursors together to increase contact and decrease diffusion length. As heat is applied, nucleation occurs and the precursors diffuse into one another. In this case, copper diffuses more rapidly into lanthanum so the reactant-product interface extends further into the La_2O_3 precursor. This reaction occurs at 1200 °C for several days and the end product is often contaminated with unreacted CuO or La_2O_3 [6]. In order to reduce these impurities, the product is often reground into a fine powder then reheated to 1200 °C. While solid-state reactions yield high-quality crystals, the reactions can take a several days and, depending on the materials, require very high temperatures.

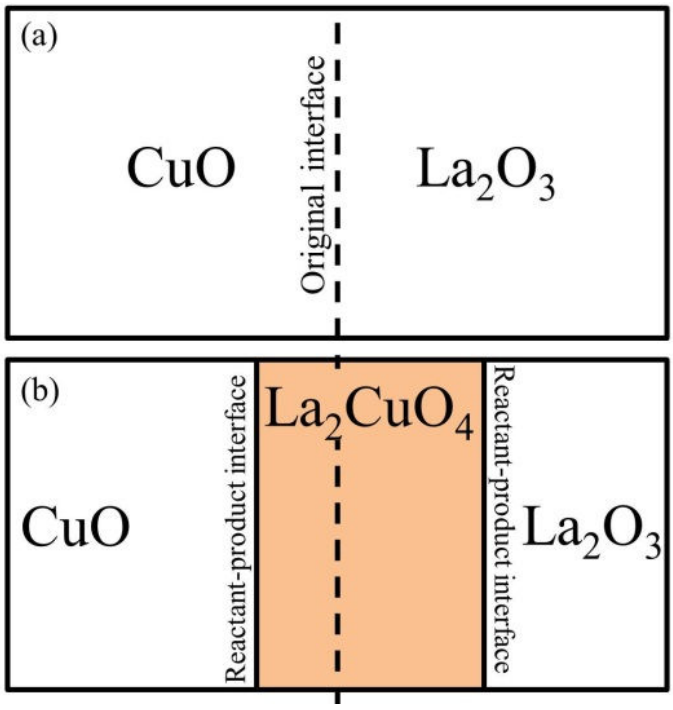

Figure 7.1. Illustration of (a) the original precursor-precursor interface before the reaction occurs and (b) after growth of the product layer upon heating. Adapted from S.R. Elliot, The Physics and Chemistry of Solids [28].

If superconductors are to be used for energy storage applications, a more efficient synthesis method is needed that is less energy intensive and easier to scale up while maintaining a reasonable manufacturing cost. Silicon is synthesized *via* the float zone method described earlier and has large industrial applications. However, the processing required to make silicon makes the material very expensive. Similarly, processing superconducting materials would make it prohibitively expensive for widespread energy storage applications. Therefore, a new synthesis method that utilizes lower temperature is necessary. As an added benefit, low-temperature synthesis would allow access to kinetically stable phases that might also be superconducting.

The goal of this research is *to develop a low temperature synthesis method* to form members of the Sr-Ru-O family as well as *determine if new phases of Sr-Ru-O* can

be formed. This family of materials is important because of their interesting properties including superconductivity and colossal magnetoresistance, among others [19, 29, 30]. In particular, Sr_2RuO_4 is superconducting without doping, unlike isostructural La_2CuO_4, and it is a prime candidate for first principles studies to investigate the mechanism of superconductivity [19]. Specifically, if nanorods of Sr_2RuO_4 can be formed the structure of the material can be carefully probed to investigate changes (i) just before, during, and after the onset of superconductivity and (ii) as the critical magnetic field is reached and the material goes from the superconducting to the normal state. Additionally, new superconducting materials can be valuable in developing a viable theory of superconductivity. Previously, strontium ruthenates have been synthesized using floating zone and solid-state methods, although there is one report of the synthesis of $Sr_2Ru_3O_{10}$ using high-pressure and high-temperature hydrothermal methods (480-630 °C) [31]. To synthesize pure, high-quality crystals of existing members of the Sr-Ru-O family and determine if new phases of this family of compounds can be formed, low temperature hydrothermal synthesis was employed. Hydrothermal methods are advantageous because of the combination of moderate temperatures and pressures that can be achieved. Mild temperatures also allow for the formation of kinetically stable phases. We have utilized hydrothermal methods at lower temperatures (140 to 210 °C) and pressures to synthesize this family of compounds.

7.6 References

[1] P.W. Anderson, G. Baskaran, Z. Zou, T. Hsu, *Phys. Rev. Lett.* 58 (1987) 2790-2793.

[2] T.K. Mandal, N.Y. Vasanthacharya, J. Gopalakrishnan, *J. Mater. Chem.* 12 (2002) 635-638.

[3] J.M. Longo, P.M. Raccah, *J. Solid State Chem.* 6 (1973) 526-531.

[4] S.L. Stoll, A.M. Stacy, C.C. Torardi, *Inorg. Chem.* 33 (1994) 2761-2765.

[5] C. Chaillout, S.W. Cheong, Z. Fisk, M.S. Lehmann, M. Marezio, B. Morosin, J.E. Schirber, *Physica C* 158 (1989) 183-191.

[6] M.K. Crawford, W.E. Farneth, E.M. McCarron, R.L. Harlow, A.H. Moudden, *Science* 250 (1990) 1390-1394.

[7] J.P. Attfield, A.L. Kharlanov, J.A. McAllister, *Nature* 394 (1998) 157-159.

[8] D. Larbalestier, A. Gurevich, D.M. Feldmann, A. Polyanskii, *Nature* 414 (2001) 368-377.

[9] C. Enz, in: Z. Petru, J. Przystawa, K. Rapcewicz, (Eds.), From Quantum Mechanics to Technology, Springer Berlin / Heidelberg, 1997, pp. 143-160.

[10] R. Shannon, *Acta Crystallogr. A* 32 (1976) 751-767.

[11] Y. Ma, L. Xiao, *Chinese Sci. Bull.* 49 (2004) 2435-2439.

[12] A. Survila, Z. Mockus, S. Kanapeckaite, J. Pileckiene, G. Stalnionis, *Russ. J. Electrochem.*+ 47 (2011) 129-135.

[13] J. Schmalian, *Mod. Phys. Lett. B* 24 (2010) 2679-2691.

[14] A.K. Saxena, High-Temperature Superconductors, Springer Berlin Heidelberg, 2010, pp. 199-214.

[15] J. Bardeen, L.N. Cooper, J.R. Schrieffer, *Phys. Rev.* 108 (1957) 1175-1204.

[16] J. Nagamatsu, N. Nakagawa, T. Muranaka, Y. Zenitani, J. Akimitsu, *Nature* 410 (2001) 63-64.

[17] M.E. Jones, R.E. Marsh, *J. Am. Chem. Soc.* 76 (1954) 1434-1436.

[18] X.H. Chen, T. Wu, G. Wu, R.H. Liu, H. Chen, D.F. Fang, *Nature* 453 (2008) 761-762.

[19] Y. Maeno, H. Hashimoto, K. Yoshida, S. Nishizaki, T. Fujita, J.G. Bednorz, F. Lichtenberg, *Nature* 372 (1994) 532-534.

[20] P.W. Anderson, Z. Zou, *Phys. Rev. Lett.* 60 (1988) 132-135.

[21] L.N. Cooper, *Phys. Rev.* 104 (1956) 1189-1190.

[22] J. Bardeen, L.N. Cooper, J.R. Schrieffer, *Phys. Rev.* 106 (1957) 162-164.

[23] J. Bardeen, *Phys. Rev.* 97 (1955) 1724-1725.

[24] C. Kittel, *Introduction to solid state physics*. Wiley, Hoboken, NJ, 2005.

[25] E. Maxwell, *Phys. Rev.* 78 (1950) 477-477.

[26] C.A. Reynolds, B. Serin, L.B. Nesbitt, *Phys. Rev.* 84 (1951) 691-694.

[27] D. Rainer, *Physica B+C* 109-110 (1982) 1671-1676.

[28] S.R. Elliott, *The physics and chemistry of solids*. J. Wiley, Chichester, West Sussex, England ;, 1998.

[29] G. Cao, C.S. Alexander, S. McCall, J.E. Crow, R.P. Guertin, *Materi. Sci. Eng. B-Adv.* 63 (1999) 76-82.

[30] I. Eremin, D. Manske, S.G. Ovchinnikov, J.F. Annett, *Ann. Phys.* 13 (2004) 149-174.
[31] C. Renard, S. Daviero-Minaud, F. Abraham, *J. Solid State Chem.* 143 (1999) 266-272.

CHAPTER 8

FACILE SYNTHESIS OF MEMBERS OF THE SR-RU-O FAMILY

8.1 Overview

A low temperature hydrothermal method for the synthesis of compounds in the strontium-ruthenate family has been developed. This family of materials is important because of their interesting properties including superconductivity and colossal magnetoresistance, among others.[1, 2] Previously, strontium-ruthenates have been synthesized using floating zone methods although there is one report of the synthesis of $Sr_2Ru_3O_{10}$ using high pressure and temperature hydrothermal methods (480-630 °C).[3, 4] Hydrothermal methods are advantageous because of the combination of moderate temperatures and pressures that can be achieved. We have utilized hydrothermal methods at lower temperatures (140 to 210°C) and pressures to synthesize this family of compounds. We have recently synthesized nanoscale cubes of $SrRuO_3$ and hexagonal platelets of $Sr_2Ru_3O_{10}$ and $SrRuO_4 \cdot H_2O$. Variables such as pH, temperature, and reaction time will be discussed.

8.2. Introduction

Perovskite oxides in the Ruddlesden-Popper (R-P) series exhibit many different properties including high temperature superconductivity in cuprates and magnetoresistance in manganites [5, 6]. The strontium ruthenates in the R-P series

$Sr_{n+1}Ru_nO_{3n+1}$ are an interesting family of compounds that have been investigated due to observed properties depending on n such as superconductivity in Sr_2RuO_4 where n=2 and ferromagnetism in $SrRuO_3$ where n=∞.

The ruthenium in members of the R-P series and $SrRuO_3$ contain varying oxidation states of ruthenium including Ru(IV) in $Sr_{n+1}Ru_nO_{3n+1}$ (n=1, 2 and 3) and $SrRuO_3$, Ru(V) in $Sr_4Ru_2O_9$, Ru (VI) in $SrRuO_4 \cdot H_20$, and mixed valent Ru(V) and (VI) in $Sr_2Ru_3O_{10}$. The compound $SrRuO_3$, where n=∞, is an itinerant ferromagnet with T_{Curie} = 160 K. At room temperature $SrRuO_3$ is orthorhombic with *Pbnm* symmetry and is isostructural to $GdFeO_3$ [7]. The first member of the R-P series, Sr_2RuO_4, is metallic but not ferromagnetic and also exhibits superconductivity at ~ 1 K [2]. Sr_2RuO_4 is tetragonal K_2NiF_4 structure type with *I4/mmm* symmetry and consists of a single RuO_2 plane per formula unit [8]. The third member of the R-P family, $Sr_3Ru_2O_7$, has been reported to be an antiferromagnetic [9], an itinerant ferromagnet [10], then as an enhanced paramagnetic metal [11, 12], and finally claimed to be a meta-magnet with quantum criticality [12-16]. The observed physical properties are highly dependent on the crystal growth technique. $Sr_3Ru_2O_7$ has one Ru-O bilayer per formula unit and the structure is orthorhombic with *Bbcb* symmetry with pseudotetragonal unit cell (where a~b) [17]. $Sr_4Ru_2O_9$ is hexagonal with $P\bar{6}2c$ symmetry [18, 19]. Literature dedicated to this compound is rare and includes the elaboration of the structure using powders and thin films [18, 19]. These members of the Ruddlesden-Popper series are all described by $Sr_{n+1}O_{3n+1}$ layers where ruthenium occupies the octahedral sites between layers. Other members of the Sr-Ru-O family include tetragonal $Sr_4Ru_3O_{10}$ with *I4/mmm* symmetry [20] and $SrRuO_4 \cdot H_2O$ for which no crystal structure has been reported [21].

Different synthetic routes have been used for the preparation of strontium ruthenium oxides, including the traditional solid state method, floating zones, flux growth, pulsed laser deposition, sol-gel methods, and hydrothermal methods (≥ 500 °C) [4, 22-25]. The latter approach has been used extensively by our research group to grow crystals of strontium ruthenium oxides at low temperature (≤ 210 °C) while controlling the oxidation state of the ruthenium. Low temperature hydrothermal methods offer control of the reaction products through a variety of reaction conditions including temperature, metal precursor concentration, mineralizer concentration, and reaction time. Also, hydrothermal conditions favor the solubility and mobility of species that allow access to crystalline products otherwise inaccessible under conventional conditions [24]. Lastly, the low temperatures and one-step synthesis makes this a convenient method not only for the synthesis of strontium ruthenium oxides, but also for the synthesis of other transition metal oxides.

The aim of this work is to control the oxidation state of ruthenium to direct the formation of specific members of the strontium ruthenate family. In this chapter we present the low temperature hydrothermal synthesis of $SrRuO_3$ and $SrRuO_4 \cdot H_2O$ as well as mixtures of $Sr_2Ru_3O_{10}$, $Sr_4Ru_2O_9$, and $SrRuO_4 \cdot H_2O$. In these compounds the ruthenium oxidation ranges between (IV) and (VI). Controlling the electrochemical potential of the reaction solution via temperature and amount of mineralizer in each reaction mixture allows for control of the ruthenium oxidation state in the product.

8.3. Experimental details

8.3.1 Preparation of Sr-Ru-O Compounds

The synthesis of $SrRuO_3$, $SrRuO_4 \cdot H_2O$, and $Sr_2Ru_3O_{10}$ were carried out using low temperature (≤ 210 °C) hydrothermal methods. The metal precursors included K_2RuO_4 (Pfaltz and Bauer, 95%) and $Sr(OH)_2$ (Sigma-Aldrich, 95%). All experimental procedures were completed in a glove bag under an argon atmosphere. The reactants were placed in a 23 mL capacity poly(tetrafluoroethylene) (PTFE)-lined pressure vessel, with 10 mL dilute KOH prepared from freshly distilled water (previously adjusted to pH 12-14) and sealed in an acid digestion bomb (Parr Instruments) under an inert atmosphere. The acid digestion bomb was then placed in the furnace for 24 hours and heated at a constant rate of 2 °C/min to 140 °C, 175 °C, or 210 °C (Table 8.1). After 24 hours, the digestion bomb was removed and allowed to quickly cool to room temperature. The precipitates were then collected by filtration and washed with copious amounts of distilled water and dried in air for 12 h. The reactions produced a highly crystalline black or red powder.

Table 8.1. Strontium ruthenate reaction temperatures and KOH concentration required to synthesize the desired product.

Product	Reaction Temp (°C)	[KOH]
$SrRuO_3$	210	saturated
$Sr_2Ru_3O_{10}$ **$Sr_4Ru_2O_9$**	210	pH 14
$SrRuO_4 \cdot H_2O$ **$Sr_2Ru_3O_{10}$** **$Sr_4Ru_2O_9$**	175	pH 13
$SrRuO_4 \cdot H_2O$	140	pH 13-14

8.3.2 Characterization

Powder X-ray diffraction analyses were carried out to determine the crystalline phases of the synthesized powder. Measurements were made by an X-ray diffractometer (Scintag X-2) with Cu Kα radiation at 40 kV and 20 mA. Diffraction patterns were collected in the 2θ range of 20 to 80 ° at a scanning speed of 2.5 °/min. Morphological aspects of the powders were examined using SEM (JEOL JSM-6500F). The samples were attached to an aluminum mount using carbon tape.

8.4. Results and Discussion

8.4.1 Synthesis of Sr-Ru-O Compounds

Samples of poly-crystalline strontium ruthenates were prepared from the direct hydrothermal reaction (140 °C) between RuO_4^{2-} and Sr^{2+} where 0.1-1 M KOH acted as the mineralizer. Figure 8.1 is a representative XRD pattern showing the formation of $SrRuO_4 \cdot H_2O$ and $SrCO_3$ when the solution pH varies between 13 and 14. The $SrCO_3$ contamination is a result of dissolved CO_2 and absorption by KOH or $Sr(OH)_2$. $SrCO_3$ crystals are long and needle-like and are easily distinguishable from the desired strontium ruthenium oxides. At these reaction conditions, the initial ruthenium (VI) was not reduced, but remained in the (VI) oxidation state. The synthesized $SrRuO_4 \cdot H_2O$ was indexed with a hexagonal unit cell. Figures 8.1f and 8.1g show representative SEM micrographs of the collected red powder.

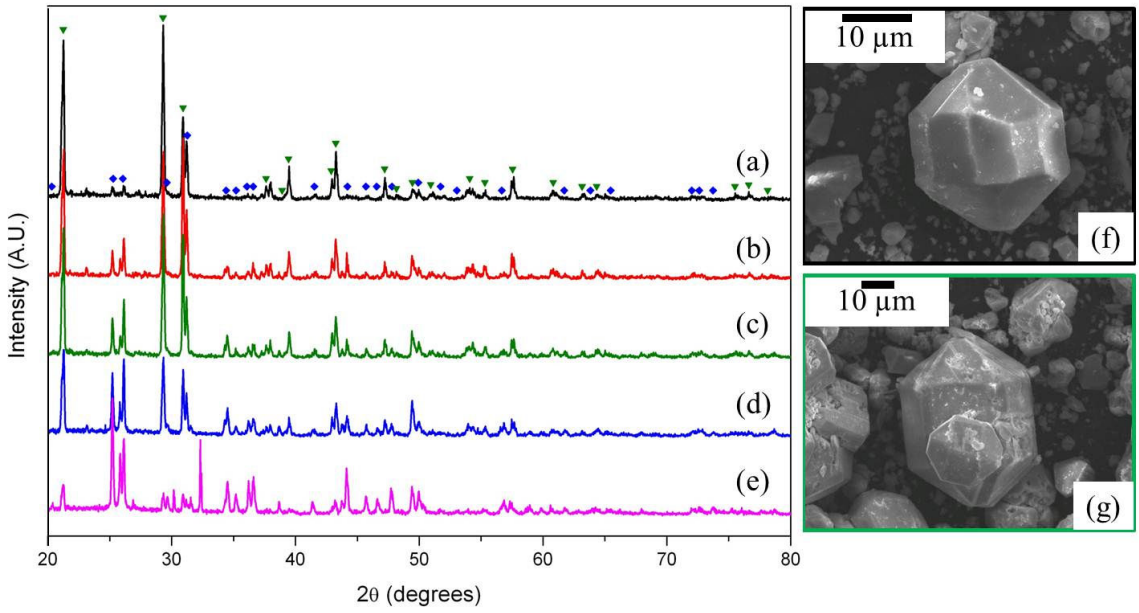

Figure 8.1. XRD powder pattern of hexagonal perovskite $SrRuO_4 \cdot H_2O$ (PDF 35-0949) and $SrCO_3$ (PDF 71-2393) at pH values (a) 13.00, (b) 13.25, (c) 13.50, (d) 13.75 and (e) 14.00. SEM images (f) and (g) show characteristic morphology of the as-synthesized $SrRuO_4 \cdot H_2O$. Green triangles mark the reflections that correspond to hexagonal $SrRuO_4 \cdot H_2O$ and the blue diamonds mark the reflections that correspond to orthorhombic $SrCO_3$.

It was observed that $SrRuO_4 \cdot H_2O$ formed large hexagonal crystals where the middle was a hexagonal prism with a pyramid on both ends. The width of the crystals ranged from hundreds of nanometers to microns and the length of the crystals ranged from approximately 1-15 μm. The crystals were well faceted but some particles exhibited pitting and surface degradation, as shown in Figure 8.1g. Etching of the crystal surface indicates the reaction time may be too long which allows for the partial dissolution of the particles by KOH. The concentration of KOH affects the chemical composition of the reaction product by altering which oxidation states of ruthenium are accessible. The ideal [KOH] values were found to be [KOH] = saturated and 0.1 to 1 M. Interestingly, the intensity of the $SrCO_3$ reflections increases with increasing pH. This

may be due to additional CO_2 absorption by KOH at higher pH values or could be a result of preparation order and exposure time to ambient air, thus allowing the absorption of CO_2. As a result, the preparation of the reaction was altered to include freshly distilled water for the KOH and sealing the vessel under an inert atmosphere. This practice greatly diminished, and in some cases completely eliminated the amount of $SrCO_3$ contaminant observed in the reaction product.

Raising the temperature from 140 to 175 °C results in the formation of a crystalline mixture of $SrRuO_4 \cdot H_2O$, $Sr_2Ru_3O_{10}$, $Sr_4Ru_2O_9$, and $SrCO_3$ as shown by the XRD pattern in Figure 8.2. Three main morphologies were observed in SEM images including hexagonal prisms with pyramids on the end, hexagonal platelets, and rectangular prisms. $SrRuO_4 \cdot H_2O$, $Sr_2Ru_3O_{10}$ and $SrCO_3$ were readily identified using the XRD pattern but due to peak overlap of these compounds, closer inspection of the rectangular structures observed in the SEM using TEM-SAED was required to confirm that the rectangular prisms were $Sr_4Ru_2O_9$. The morphology of the synthesized strontium ruthenium oxides are consistent with the morphology of the individually synthesized materials.

Closer inspection of the rectangular prism structures using TEM-SAED shows they are indeed $Sr_4Ru_2O_9$. A polycrystalline rod of the material was examined using TEM-SAED the resulting TEM image and SAED pattern are shown in Figure 8.3.

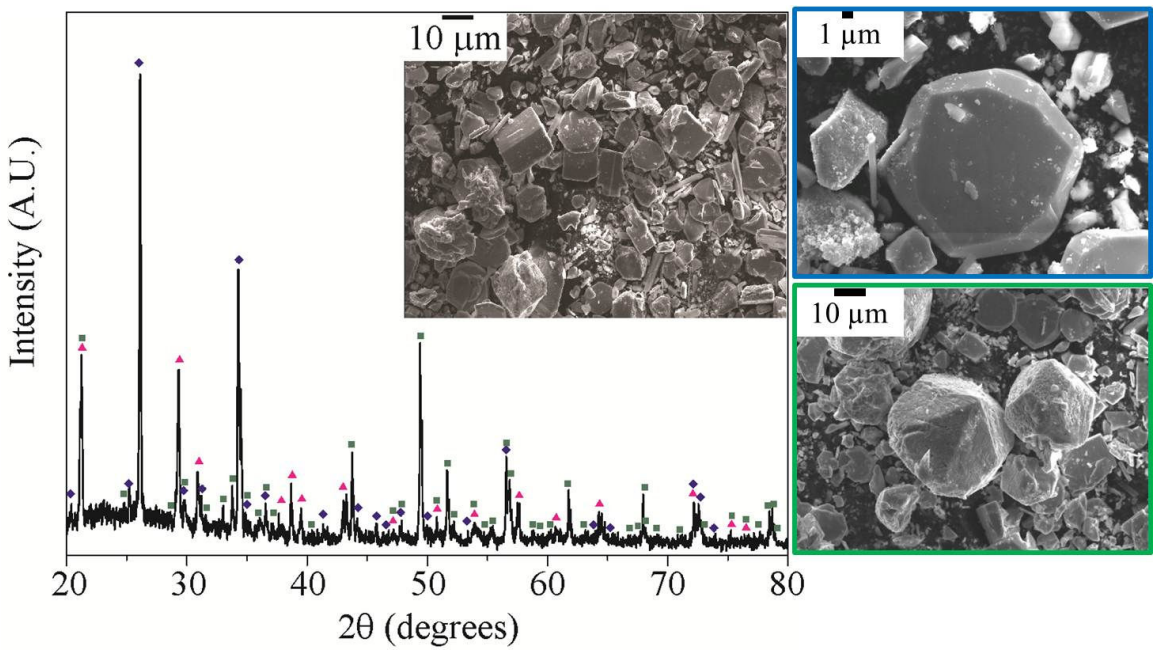

Figure 8.2. XRD powder pattern of hexagonal perovskite $SrRuO_4 \cdot H_2O$ (PDF 35-0949) and monoclinic $Sr_2Ru_3O_{10}$ (PDF 89-4456) with hexagonal $Sr_4Ru_2O_9$ (PDF 83-0223). The magenta triangles mark the reflections that correspond to hexagonal $SrRuO_4 \cdot H_2O$, green squares $Sr_2Ru_3O_{10}$, and the blue diamonds correspond to $SrCO_3$. Insets SEM micrographs of synthesized $SrRuO_4 \cdot H_2O$ and $Sr_2Ru_3O_{10}$.

The SAED shows the material is polycrystalline and the rings index to the (202), (110), (212), and (002) lattice planes of $Sr_4Ru_2O_9$. Despite the overlap of reflections in the XRD, the TEM-SAED confirms the presence of the $Sr_4Ru_2O_9$. Under these reaction conditions, the accessible ruthenium oxidation states are Ru(V), (V and VI) and (VI). The presence of these three strontium ruthenium oxides indicates that at this specific set of reaction conditions a phase boundary between Ru(IV) and Ru(V) exists. Small changes in pH or temperature may alter the accessible oxidation states of ruthenium, thereby allowing the synthesis of one compound instead of a mixture.

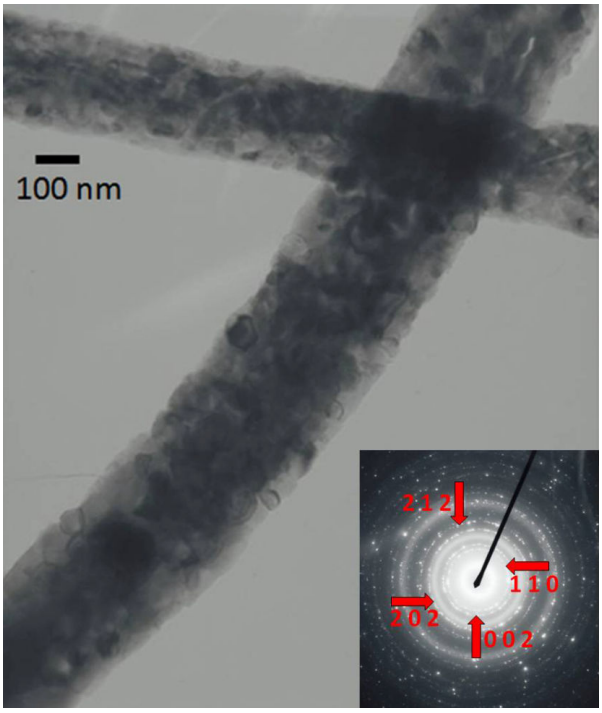

Figure 8.3. TEM images of rectangular rod structure. Pictured are smaller polycrystalline $Sr_4Ru_2O_9$ rods of the material. The SAEDs (inset) shows the material indexes to $Sr_4Ru_2O_9$. *TEM and SAED images were obtained by Mary B. Martucci.*

Further raising the temperature from 175 to 210 °C with 0.1 M KOH mineralizer allows for the formation of $Sr_2Ru_3O_{10}$ and $Sr_4Ru_2O_9$. The $Sr_2Ru_3O_{10}$ was indexed with a monoclinic unit cell (space group *C2/m*) and the $Sr_4Ru_2O_9$ was indexed with a hexagonal unit cell (space group $P\bar{6}2c$). SEM images in Figure 8.4 shows a survey view of the reaction product, the hexagonal platelet, and rod morphology for these compounds. The $Sr_4Ru_2O_9$ formed rectangular crystals where the length and width were on the order of 10-50 μm. The $Sr_2Ru_3O_{10}$ formed thin hexagonal platelets and a large size distribution was observed where the width of the crystals ranged from 10-100 μm.

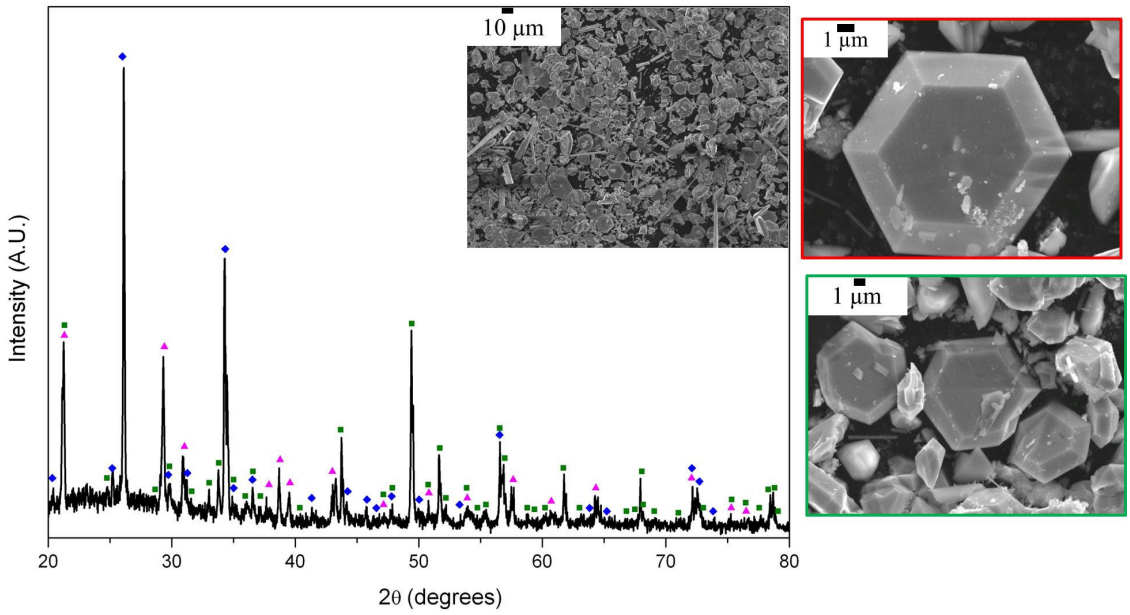

Figure 8.4. XRD pattern of $Sr_2Ru_3O_{10}$ (PDF 89-4456), $Sr_4Ru_2O_9$ (PDF 83-0223), and $SrCO_3$ (PDF 05-0418). The magenta triangles mark the reflections that correspond to hexagonal $SrRuO_4 \cdot H_2O$, the green squares indicate the reflections that correspond to $Sr_2Ru_3O_{10}$, and the blue circles indicate the reflections that correspond to $SrCO_3$. Inset: SEM image of reaction product mixture containing $Sr_2Ru_3O_{10}$ and $Sr_4Ru_2O_9$. Top and bottom SEM images: characteristic morphology of $Sr_2Ru_3O_{10}$.

The width of the platelets ranged from hundreds of nanometers to microns and the breadth of the platelets ranged from approximately 1-10 microns. The crystals are well faceted and etching of the surface is observed. Reducing the reaction time would decrease the etching, preserving the crystal surface. Under these experimental conditions, Ru(VI) was partially reduced to Ru(V) as $Sr_2Ru_3O_{10}$ contains both Ru (V) and (VI). $Sr_4Ru_2O_9$ was formed by the reduction of Ru(VI) to (V). The partial reduction of ruthenium to form two different Sr-Ru-O compounds each containing Ru(V) and one containing both (V and VI) indicates a boundary condition where the Ru may or may not be reduced from (VI) to (V). Both oxidation states are accessible and a shift in reaction temperature affords the synthesis of a single valent Ru Sr-Ru-O compound.

Using temperature the electrochemical potential of the reaction solution has been changed so that KOH reduces ruthenium. At 140 °C, the Ru(VI) was maintained and no reduction occurred. Increasing the temperature to 175 °C and 210 °C, changed the electrochemical potential of the solution so that the reaction products contained a mixture of Ru(VI) and Ru(V). The reaction temperature was limited to 210 °C by the PTFE liners, which would melt above temperatures of 220 °C. Therefore, instead of using temperature to control the reducing power of KOH, the concentration of KOH was raised from 0.1 M to a saturated solution.

A reaction temperature of 210 °C with saturated KOH allows the formation of pure $SrRuO_3$. Figure 8.5 shows the XRD pattern of pure $SrRuO_3$. These samples were indexed with an orthorhombic unit cell (space group *Pnma*). All peaks index to $SrRuO_3$, no crystalline impurities were present. The inset shows a representative SEM micrograph of the collected $SrRuO_3$. The particles were cubo-octaedral, well faceted, and had a wide size distribution with both length and width on the order of hundreds of nanometers to microns. In this case, Ru(VI) was reduced to Ru(IV) by KOH. Air and CO_2 free techniques have eliminated the presence of $SrCO_3$ so that $SrRuO_3$ is present with no contamination from secondary products.

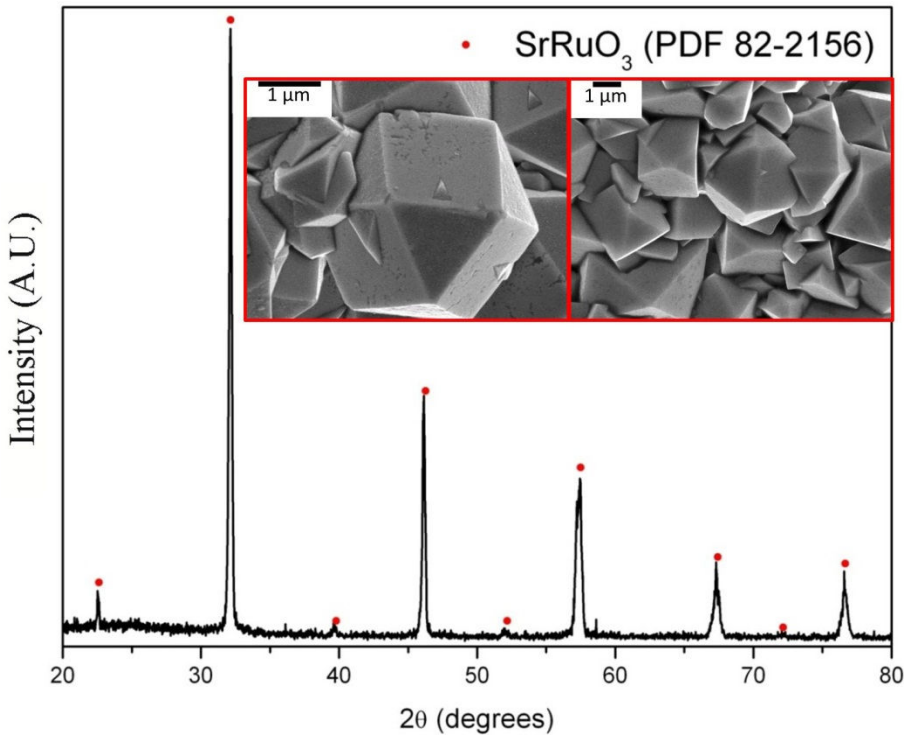

Figure 8.5. XRD pattern of the orthorhombic perovskite $SrRuO_3$ (PDF 43-0472) derived from K_2RuO_4 and $Sr(OH)_2$ precursors. All peaks index to $SrRuO_3$ as indicated by red circles. Inset: representative SEM images of the crystals.

8.4.2 Effect of reaction time

The reaction time was varied to observe changes in product composition and morphology. It was predicted the size of the product would be smaller but the composition would not change. The reaction at 140 °C and 0.1 M KOH earlier completed at 24 h, was also performed at 12 h and 4 h. A reduction in reaction time yielded $SrRuO_4 \cdot H_2O$, as determined by XRD, which was the same product obtained at 24 h. Figure 8.6 shows SEM micrographs of representative crystals for each reaction time.

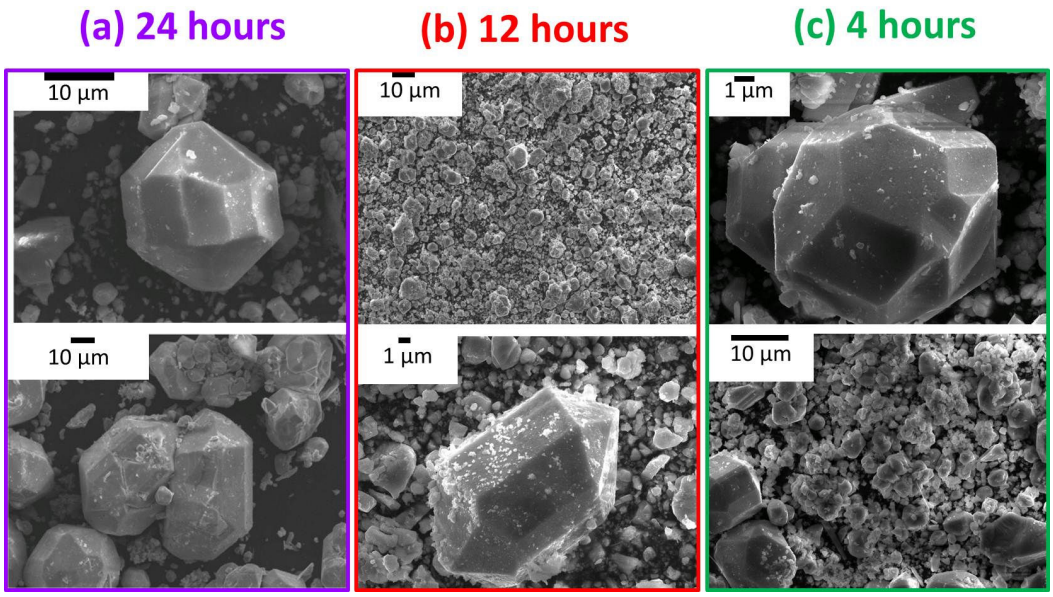

Figure 8.6. SEM images of $SrRuO_4 \cdot H_2O$ formed hydrothermally at 140 °C and a reaction time of (a) 24 hours, (b) 12 hours, and (c) 4 hours.

Decreasing the reaction time from 24 h to 12 h resulted in crystals of the same composition and similar morphology (Figures 8.6a and b). The hexagonal prism with a pyramid on the end is maintained with a shorter reaction time, but the hexagonal prism portion was larger when compared to the pyramid. Further decreasing the reaction time from 12 h to 4 h resulted in crystals with the same composition and different morphology (Figures 8.6b and c). These crystals were hexagonal, as seen in Figure 8.6c, and the pyramid on the end was not completely formed. A reaction time greater than 4 h is required for the pyramids on the end to fully form. At less than 4 h, hexagonal crystals are the dominant product morphology. No etching of the crystals was observed at shorter reaction times, increasing the quality of the crystals. The morphology of the crystals can be controlled to a small degree using reaction time.

Another 4 h reaction was performed with the KOH concentration at 0.01 M (pH 12). The result indicates the presence of a phase boundary at these reaction conditions. The XRD of the reaction product is shown in Figure 8.7.

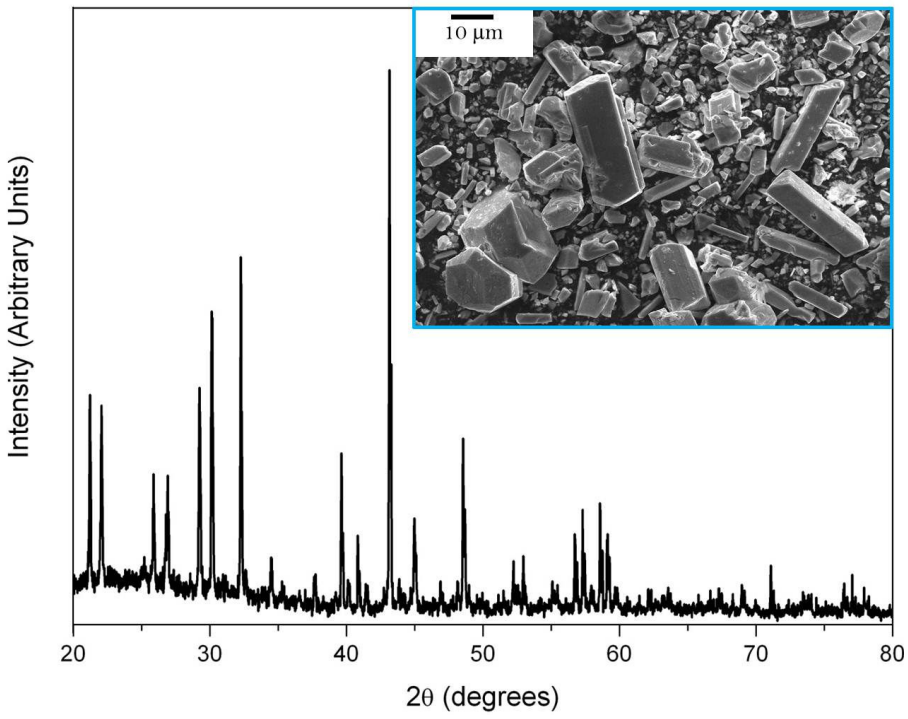

Figure 8.7. XRD pattern of the reaction product derived from K_2RuO_4 and $Sr(OH)_2$ precursors at pH 12 and a reaction time of 4 hours.

Doublets present in the XRD pattern indicate that at least two products are present with similar structures. Additionally, the doublet peak spacing is not even over the entire pattern making it difficult to distinguish which peaks belong to a single product. Lastly, due to the XRD peak overlap for many Sr-Ru-O compounds, the composition of the reaction products was not determined by XRD. Based on the characteristic morphology of previously synthesized Sr-Ru-O materials it was determined that the hexagonal prism and pyramid morphology was due to the presence of $SrRuO_4 \cdot H_2O$. Also, using TEM-SAED it was determined that $Sr_4Ru_2O_9$ was present. The other main product consisted of

large rectangular prisms. Unfortunately, these crystals are too large to identify using TEM-SAED and too small to mount on the single crystal X-ray diffractometer. At this time, ways to characterize this material are still being considered.

Comparing the results of the reactions performed at 0.01 M and 0.1 M (pH 12 and 13) indicate that a phase boundary is accessible at these reaction conditions. Reactions at pH 13 and 4 h result in the presence of $SrRuO_4 \cdot H_2O$ while at pH 12 the product is a mixture including both $SrRuO_4 \cdot H_2O$ and $Sr_4Ru_2O_9$, along with an unidentified phase. At pH 12, the Ru is only in the (IV) oxidation state, while increasing the pH to 13 results in Ru in the (V) and (VI) oxidation states. A small change in pH can change the reaction product from a mixture Ru(V) and (VI) to Ru(V) only. Additionally, it is possible that the unidentified compound is a new phase of Sr-Ru-O accessible at low temperature.

8.4.3 Effect of pH

The reaction product from a solution containing RuO_4^{2-} and Sr^{2+} is sensitive to pH, temperature, and time, all of which influence the reducing power of the KOH solution. In particular, the pH of the reaction solution has a significant effect on the accessible oxidation states of ruthenium in that particular reaction solution, which scales with the KOH mineralizer. For example, at 210 °C using a concentrated KOH solution yields the formation of $SrRuO_3$ (Ru IV). Uusing a mineralizer solution adjusted to pH 14 yields a mixture of $Sr_2Ru_3O_{10}$ (Ru V and VI) and $Sr_4Ru_2O_9$ (Ru V). In addition, at 210 °C the mixture $Sr_2Ru_3O_{10}$ and $Sr_4Ru_2O_9$ is only formed at pH >14, below pH 14 only $SrCO_3$ is formed. This relationship between mineralizer concentration and reducing power of the reaction solution is clearly seen with the reduction of the ruthenium precursor. At 140 °C,

$SrRuO_4 \cdot H_2O$ is easily synthesized between pH 13 and 14, but not at pH values less than 13 or greater than 14. This indicates there may be a reaction temperature/pH threshold that must be attained for a reaction to occur. Controlling the concentration of KOH in the reaction solution provides a facile synthesis of various strontium ruthenates by controlling the available oxidation states.

8.4.4 Effect of temperature

Similarly, the reaction temperature may be used to control the available oxidation states of ruthenium and solubility of the metal precursors. Elevated temperatures and the addition of the KOH mineralizer generated soluble and reactive RuO_4^{2-} and Sr^{2+} species. At pH 14 $Sr_2Ru_3O_{10}$ with $Sr_4Ru_2O_9$ and $SrRuO_4 \cdot H_2O$ are formed at 210 °C and 140 °C, respectively. Decreasing the temperature from 210 °C to 140 °C changes the accessible oxidation states of ruthenium so that none of the ruthenium can be reduced from (VI) to (V). Therefore, a product where ruthenium exists only in the (V) oxidation state is formed. The reduction potential of the reaction solution controls the reaction product and is easily observed when considering the reaction at pH 13 and 175 °C where a mixture of $Sr_2Ru_3O_{10}$, $Sr_4Ru_2O_9$ and $SrRuO_4 \cdot H_2O$ was synthesized. The oxidation state of ruthenium in these reaction products was mixed valent (Ru (VI) and (V)), Ru(V), and Ru(VI), respectively. The formation of $SrRuO_4 \cdot H_2O$ did not require a change in the Ru oxidation state. On the other hand, the formation of mixed valent $Sr_2Ru_3O_{10}$ requires the partial reduction of Ru(VI) to Ru(V). Additionally, $Sr_4Ru_2O_9$ is formed by the complete reduction of Ru(VI) to Ru(V). A small change in reaction temperature or mineralizer concentration may allow for the formation a single reaction product containing Ru in a

single oxidation state. A reaction temperature and solution pH above a reaction threshold is required for the formation of strontium ruthenates. Control of the temperature and KOH mineralizer concentration allows the oxidation state of the ruthenium to be predicted, though the product cannot be predicted since there are multiple strontium ruthenates with the same ruthenium oxidation state.

8.4.5 Controlling the CO_2 concentration

In addition to accurately knowing the [KOH], the amount of CO_2 absorbed must be controlled. Pure water absorbs 1.45 g CO_2/L and the ionic strength contribution of CO_2 is approximately 87 mM at pH 10 [26, 27]. The role of water and head space air in the absorption of CO_2 was elucidated by performing experiments in the absence of air. Carbon dioxide was eliminated from the water used to prepare the KOH by distillation and the pressure vessel was sealed under an argon atmosphere. Minimizing the absorption of CO_2 using air-free preparation techniques dramatically reduced, but did not always completely eliminate the $SrCO_3$ impurity. At higher reaction temperatures $SrCO_3$ contamination appears to diminish with no reflections occurring in the XRD powder pattern, but at lower temperatures and higher pH $SrCO_3$ continues to be formed. Whether or not CO_2 is present in the pressure vessel, $SrRuO_3$, $Sr_2Ru_3O_{10}$, and $SrRuO_4 \cdot H_2O$ were prepared hydrothermally at low temperatures (≤210 °C) using a KOH mineralizer.

8.5. Conclusions and Future Work

This study demonstrates that micron-sized crystallites of $SrRuO_3$, $Sr_2Ru_3O_{10}$, $Sr_4Ru_2O_9$ and $SrRuO_4 \cdot H_2O$ can be prepared by the hydrothermal reaction between

$Sr(OH)_2$ and K_2RuO_4. While alkaline conditions were necessary for the stability of the RuO_4^{2-} anion, a solution pH >12 and temperatures between 140-210 °C yielded several members of the strontium ruthenate family. The effects of reaction time, temperature, and mineralizer concentration were investigated to determine changes in product composition and morphology. Decreasing the reaction time from 24 h to 4 h resulted in products of the same composition but different morphologies. Changes in reaction temperature or mineralizer concentration were required to change the product composition, as summarized in Table 8.2.

Table 8.2. Summary of reaction products and the corresponding Ru oxidation state at various reaction temperatures and mineralizer concentrations.

Product	Ru ox. state	Reaction Temp (°C)	[KOH]
$SrRuO_3$	IV	210	saturated
$Sr_2Ru_3O_{10}$ **$Sr_4Ru_2O_9$**	VI and V V	210	pH 14
$SrRuO_4 \cdot H_2O$ **$Sr_2Ru_3O_{10}$** **$Sr_4Ru_2O_9$**	VI VI and V V	175	pH 13
$SrRuO_4 \cdot H_2O$	VI	140	pH 13-14

In general, higher reaction temperatures and higher mineralizer concentrations resulted in compounds containing Ru(IV). Lower reaction temperatures and lower mineralizer concentrations resulted in compounds containing Ru(VI), where the ruthenium precursor was not reduced and maintained the original oxidation state. Changing either the temperature or the KOH concentration allows access to Sr-Ru-O compounds where Ru(V) or a mixture of Ru(VI) and (V) are present.

The formation of secondary $SrCO_3$ was decreased by using air/CO_2 free techniques, but did not always completely eliminate the presence of the carbonate. These air/ CO_2 free techniques included the use of freshly distilled water and sealing the reaction devices under an inert atmosphere. The reduction of $SrCO_3$ in the reaction product made for easier characterization and allowed for the formation of more Sr-Ru-O product.

In order to synthesize members of the Sr-Ru-O family and construct a phase diagram for this material using $Sr(OH)_2$ and K_2RuO_4 precursors, pure K_2RuO_4 must first be synthesized. The main supplier of this material, Pfaltz and Bauer, has since stopped manufacturing and distributing this material. Secondly, the phase boundary discovered during the time study must be more thoroughly studied. Experiments with small incremental changes in pH or temperature will help narrow down the reaction parameters where the boundary occurs. Monitoring the composition and morphology of the reaction product using XRD and SEM is an important step.

New experiments that use temperatures lower than 140 °C can be performed to look for undiscovered low temperature phases where Ru(VI) exists. Also, probing mineralizer concentration at 280 °C may yield new reaction products. In this work, only saturated KOH was considered at 280 °C. Additionally, new Sr-Ru-O compounds may be formed by altering the ratio of Sr:Ru precursors. Specifically, since the CO_2 contamination was removed, the formation of the superconducting Sr_2RuO_4 phase may be promoted where the reaction conditions allow Ru(VI) to be reduced to Ru(IV). All experiments described previously used a 1:1 ratio of Sr:Ru. A concentration study of metal precursors is required at various reaction parameters including: time, temperature,

and KOH concentration. It is also possible that other precursors are suitable for the hydrothermal synthesis of these materials. However, Ru metal using $KMnO_4$ as an oxidizing agent was considered but the presence of Mn in the reaction product was problematic. Using a different ruthenium precursor could remove the requirement for a highly alkaline solution to maintain the stability of the RuO_4^{2-} and new Sr-Ru-O materials may be formed. In terms of the Sr precursor, $Sr(NO_3)_2$, SrO, and $Sr(OH)_2$ were studied, and it was determined that $Sr(OH)_2$ was the best choice to use with K_2RuO_4 due to solubility and stability at high pH. The low temperature hydrothermal synthesis of Sr-Ru-O materials is a reproducible synthetic method that may be applied to other classes of transition metal oxide materials.

8.6 References

[1] R. Perry, A. Mackenzie, Y. Maeno, *Physica B* 329 (2003) 904-905.

[2] Y. Maeno, H. Hashimoto, K. Yoshida, S. Nishizaki, T. Fujita, J.G. Bednorz, F. Lichtenberg, *Nature* 372 (1994) 532-534.

[3] C. Renard, S. Daviero-Minaud, F. Abraham, *J. Solid State Chem.* 143 (1999) 266-272.

[4] S.I. Ikeda, U. Azuma, N. Shirakawa, Y. Nishihara, Y. Maeno, *J. Cryst. Growth* 237 (2002) 787-791.

[5] G. Cao, C.S. Alexander, S. McCall, J.E. Crow, R.P. Guertin, *Materi. Sci. Eng. B-Adv.* 63 (1999) 76-82.

[6] R. Ciancio, J. Borjesson, H. Pettersson, R. Fittipaldi, D. Zola, A. Vecchione, M. Polichetti, S. Kittaka, Y. Maeno, S. Pace, E. Olsson, *Phys. Rev. B* 80 (2009).

[7] C.W. Jones, P.D. Battle, P. Lightfoot, W.T.A. Harrison, *Acta Crystallogr. Sect. C-Cryst. Struct. Commun.* 45 (1989) 365-367.

[8] L. Walz, F. Lichtenberg, *Acta Crystallogr. Sect. C-Cryst. Struct. Commun.* 49 (1993) 1268-1270.

[9] R.J. Cava, H.W. Zandbergen, J.J. Krajewski, W.F. Peck, B. Batlogg, S. Carter, R.M. Fleming, O. Zhou, L.W. Rupp, *J. Solid State Chem.* 116 (1995) 141-145.

[10] G. Cao, S. McCall, J.E. Crow, *Phys. Rev. B* 55 (1997) R672-R675.

[11] S. Ikeda, Y. Maeno, S. Nakatsuji, M. Kosaka, Y. Uwatoko, *Phys. Rev. B* 62 (2000) R6089-R6092.

[12] R.S. Perry, L.M. Galvin, S.A. Grigera, L. Capogna, A.J. Schofield, A.P. Mackenzie, M. Chiao, S.R. Julian, S.I. Ikeda, S. Nakatsuji, Y. Maeno, C. Pfleiderer, *Phys. Rev. Lett.* 86 (2001) 2661-2664.

[13] P. Gegenwart, F. Weickert, M. Garst, R.S. Perry, Y. Maeno, *Phys. Rev. Lett.* 96 (2006).

[14] K. Kitagawa, K. Ishida, R.S. Perry, T. Tayama, T. Sakakibara, Y. Maeno, *Phys. Rev. Lett.* 95 (2005).

[15] R.S. Perry, K. Kitagawa, S.A. Grigera, R.A. Borzi, A.P. Mackenzie, K. Ishida, Y. Maeno, *Phys. Rev. Lett.* 92 (2004).

[16] A. Tamai, M.P. Allan, J.F. Mercure, W. Meevasana, R. Dunkel, D.H. Lu, R.S. Perry, A.P. Mackenzie, D.J. Singh, Z.X. Shen, F. Baumberger, *Phys. Rev. Lett.* 101 (2008).

[17] H. Shaked, J.D. Jorgensen, O. Chmaissem, S. Ikeda, Y. Maeno, *J. Solid State Chem.* 154 (2000) 361-367.

[18] R. Chmielowski, V. Madigou, M. Blicharski, C. Leroux, *J. Cryst. Growth* 310 (2008) 3854-3860.

[19] C. Dussarrat, J. Fompeyrine, J. Darriet, *Eu.r J. So.l State Inor.* 32 (1995) 3-14.

[20] M.K. Crawford, R.L. Harlow, W. Marshall, Z. Li, G. Cao, R.L. Lindstrom, Q. Huang, J.W. Lynn, *Phys. Rev. B* 65 (2002).

[21] T.L. Popova, N.G. Kisel, V.P. Karlov, V.I. Kirvobok, *Russ. J. Inorg. Chem+* (1981) 1613.

[22] K. Byrappa, T. Adschiri, *Prog. Cryst. Growth Ch.* 53 (2007) 117-166.

[23] A. Querejeta, A. Varela, M. Parras, F. del Monet, M. Garcia-Hernandez, J.M. Gonzalez-Calbet, *Chem. Mater.* (2009) 1898-1902.

[24] A. Rabenau, *Angew Chem Int Edit* 24 (1985) 1026-1040.
[25] M.S. Whittingham, *Curr. Opin. Solid St. M.* 1 (1996) 227-232.
[26] A. Persat, R.D. Chambers, J.G. Santiago, *Lab Chip* 9 (2009) 2437-2453.
[27] A. Yasunishi, F. Yoshida, *J. Chem. Eng. Data* 24 (1979) 11-14.